

IONIZATION DYNAMICS IN INTENSE LASER  
FIELDS: APPLICATIONS OF TWO-COLOR FIELDS  
AND OF THE NUMERICAL TIME-OF-FLIGHT  
ANALYSIS

DISSERTATION

ZUR ERLANGUNG DES AKADEMISCHEN GRADES  
DOCTOR RERUM NATURALIUM (DR. RER. NAT.)  
DER MATHEMATISCH-NATURWISSENSCHAFTLICHEN FAKULTÄT  
DER UNIVERSITÄT ROSTOCK

VORGELEGT VON:	VASILII ANDREEVICH TULSKII
GEBOREN AM:	12.03.1992 IN MOSKAU, RUSSLAND
BETREUER:	PROF. DR. DIETER BAUER, UNIVERSITÄT ROSTOCK, INSTITUT FÜR PHYSIK
GUTACHTER:	PROF. DR. DIETER BAUER, UNIVERSITÄT ROSTOCK, INSTITUT FÜR PHYSIK
GUTACHTER:	PROF. DR. CARLA FARIA, UNIVERSITY COLLEGE LONDON, DEPARTMENT OF PHYSICS AND ASTRONOMY
GUTACHTER:	PROF. DR. MIKHAIL IVANOV, MBI FÜR NICHTLINEARE OPTIK UND KURZZEITSPEKTROSKOPIE IM FORSCHUNGSVERBUND BERLIN
EINGEREICHT AM:	20. SEPTEMBER 2021
VERTEIDIGT AM:	21. JANUAR 2022

[https://doi.org/10.18453/rosdok\\_id00003531](https://doi.org/10.18453/rosdok_id00003531)

# CONTENTS

<b>Contents</b>	<b>I</b>
<b>Abstract</b>	<b>III</b>
<b>Zusammenfassung (German)</b>	<b>III</b>
<b>Publications</b>	<b>1</b>
<b>Abbreviations</b>	<b>4</b>
<b>Introduction</b>	<b>5</b>
<b>1 Basic theory and approximations</b>	<b>8</b>
1.1 Single-active-electron treatment . . . . .	8
1.2 Strong-field approximation . . . . .	9
1.2.1 Classical trajectories and quantum interference . . . . .	10
1.2.2 Saddle-point method . . . . .	14
1.2.3 Saddle points in a monochromatic laser field . . . . .	15
1.2.4 Photoelectron spectra in two-color counter-rotating circularly polar- ized ( $\odot\odot$ ) fields . . . . .	16
1.2.5 Photoelectron spectra in two-color co-rotating circularly polarized ( $\ominus\ominus$ ) fields . . . . .	17
1.2.6 Photoelectron spectra in two-color colinearly polarized ( $\Updownarrow\Updownarrow$ ) fields . .	18
1.3 Numerical solution to the TDSE with QPROP . . . . .	19
1.3.1 Potentials in QPROP . . . . .	19
1.3.2 Representation of a wavefunction in QPROP . . . . .	20
1.3.3 Evaluating photoelectron spectrum (PES) with tSURFF in QPROP 2.0 and newer . . . . .	21
1.3.4 Evaluating the PES with iSURFV in QPROP 3.0 and newer . . . . .	22
1.3.5 Applications of QPROP 3.0 and newer . . . . .	25
<b>2 Phase-of-the-Phase spectroscopy and its applications</b>	<b>26</b>
2.1 Phase-of-the-Phase spectroscopy . . . . .	26
2.2 Calibrating the intensity of the laser with phase-of-the-phase (PoP) . . . . .	28
2.3 Retrieving laser-coherent features from a complex-target-produced PES with PoP technique . . . . .	34
2.4 Conclusions of Chapter 2 . . . . .	39
<b>3 Optimizing plasma-induced THz radiation using intense two-color ioniz-     ing laser fields</b>	<b>40</b>

3.1	Terahertz radiation resulting from the interaction of a strong laser pulse with atomic gases . . . . .	40
3.2	Optimizing the intensity ratio in a two-color laser field with colinearly polarized ( $\uparrow\uparrow$ ) components . . . . .	43
3.2.1	Corrections to the ionization probability within the strong-field approximation (SFA) for co-linear ( $\uparrow\uparrow$ ) two-color fields . . . . .	46
3.3	Optimizing polarizations of an intense two-color field components . . . . .	53
3.4	Optimal wavelengths in an intense two-color laser field . . . . .	56
3.5	Conclusions of Chapter 3 . . . . .	66
<b>4</b>	<b>Time-energy analysis of photoelectron quantum dynamics</b>	<b>67</b>
4.1	Time-of-flight analysis of PES . . . . .	68
4.1.1	Time-of-flight description of the attoclock . . . . .	70
4.1.2	Formation of the quantum interference structure . . . . .	71
4.1.3	Removing the quantum interference pattern from the PES obtained with numerical solutions to the TDSE . . . . .	73
4.2	Conclusions of Chapter 4 . . . . .	77
	<b>Conclusions and Outlook</b>	<b>78</b>
	<b>References</b>	<b>80</b>
	<b>List of figures</b>	<b>97</b>
	<b>Acknowledgements</b>	<b>99</b>

## ABSTRACT

The present work focuses on multiple processes occurring due to the interaction of strong laser fields with matter. Main attention is devoted to applications of two-color fields. Starting with the recently developed tool to describe the distributions of photoelectrons in such tailored fields, phase-of-the-phase spectroscopy, an extension to that is introduced with two particular applications demonstrated.

Next, the conversion mechanism of laser radiation to lower, terahertz, frequencies in presence of two-color fields is addressed, aiming at optimizing the conversion efficiency. The superiority of using two-color circularly polarized corotating fields of mid-infrared wavelengths is theoretically predicted.

Finally, a method of analysing the numerically obtained photoelectron spectra with respect to the registration time of electrons is proposed. The resulting time-resolved spectra allow for a direct comparison with the physically transparent but less predictive semiclassical theories.

## ZUSAMMENFASSUNG (GERMAN)

Die vorliegende Arbeit konzentriert sich auf mehrere Prozesse, die durch die Wechselwirkung von starken Laserfeldern mit Materie hervorgerufen werden. Das Hauptaugenmerk liegt auf Anwendungen von Zweifarbenfeldern. Ausgehend von dem kürzlich entwickelten Werkzeug zur Beschreibung der Verteilungen von Photoelektronen in solchen maßgeschneiderten Feldern, der Phase-der-Phase-Spektroskopie, wird eine Erweiterung dazu mit zwei bestimmten Anwendungen demonstriert.

Als nächstes wird der Umwandlungsmechanismus von Laserstrahlung in niedrigere Terahertz-Frequenzen in Gegenwart von Zweifarbenlaserfeldern behandelt, um die Umwandlungseffizienz zu optimieren. Die Überlegenheit der Verwendung von zweifarbigem, zirkular polarisierten, korotierenden Feldern mittlerer Infrarotwellenlängen wird theoretisch vorhergesagt.

Schließlich wird ein Verfahren zur Analyse der numerisch erhaltenen Photoelektronenspektren in Bezug auf die Registrierungszeit dieser Elektronen vorgeschlagen. Die resultierenden zeitaufgelösten Spektren ermöglichen einen direkten Vergleich mit den physikalisch transparenten, aber weniger vorhersagekräftigen semiklassischen Theorien.

## LIST OF PUBLICATIONS

Parts of the present thesis have been published in the following peer-reviewed journal papers:

1. **V. A. Tulskey** and D. Bauer, *Numerical time-of-flight analysis of the strong-field photoeffect*. Physical Review Research **2**(4):043083, October 2020. [arXiv:2008.06275]
2. **V. Tulskey** and D. Bauer. *Qprop with faster calculation of photoelectron spectra*. Computer Physics Communications, **251**:107098, June 2020 [arXiv:1907.08595]
3. **V. A. Tulskey**, B. Krebs, J. Tiggesbäumker, and D. Bauer. *Revealing laser-coherent electron features using phase-of-the-phase spectroscopy*. Journal of Physics B: Atomic, Molecular and Optical Physics, **53**(7):074001, February 2020 [arXiv:1911.00477]
4. **V. A. Tulskey**, M. A. Almajid, and D. Bauer. *Two-color phase-of-the-phase spectroscopy with circularly polarized laser pulses*. Physical Review A, **98**:053433, November 2018. [arXiv:1808.05167]
5. **V. A. Tulskey**, M. Bagheri, U. Saalman, and S. V. Popruzhenko. *Boosting terahertz-radiation power with two-color circularly polarized midinfrared laser pulses*. Physical Review A, **98**:053415, November 2018 [arXiv:1810.08834]
6. S. V. Popruzhenko and **V. A. Tulskey**. *Control of terahertz photoelectron currents generated by intense two-color laser radiation interacting with atoms*. Physical Review A, **92**(3):033414, September 2015

## CONFERENCE TALKS AND SEMINARS

Parts of the present thesis have been reported in the following conference and seminar talks:

1. Oct 19 – Oct 22 2021. 8th International Symposium on Optics & its applications (OPTICS-2021), Rostock, Germany.  
Oral talk: *Numerical time-of-flight analysis of the strong-field photoeffect.*
2. Oct 12 - Oct 14 2020. ELI Beamlines user conference 2020, Prague, Czech Republic.  
Oral talk: *Phase-of-the-phase spectroscopy as a tool for analyzing photoelectron spectra.*
3. Jan 26 - Jan 31 2020. EAS - Extreme Atomic Systems, Riezlern, Austria.  
Oral talk: *Applications of the phase-of-the-phase spectroscopy to two-color bi-circular fields.*
4. Nov 19 – Nov 22 2019. International Workshop on Atomic Physics, Dresden, Germany.  
Poster title: *QPROP 3.0: faster t-SURFF for slow electrons.*
5. Sep 22 - Sep 26 2019. 55th Symposium on Theoretical Chemistry, Rostock, Germany.  
Poster title: *Phase-of-the-Phase technique as a tool to exclude the laser-incoherent part from a spectrum.*
6. Sep 01 - 05 2019. Wilhelm und Else Heraeus Seminar #702: Otto Stern's Molecular Beam Research and its Impact on Science, Frankfurt am Main, Germany.  
Poster title: *Phase-of-the-Phase technique as a tool to exclude the laser-incoherent part from a photoelectron spectrum.*
7. Mar 10 - Mar 15 2019. 83. Jahrestagung der DPG und DPG-Frühjahrstagung (83rd Annual Conference of the DPG and DPG Spring Meeting), Rostock, Germany.  
Oral talk: *Extracting laser-coherent information from a photoelectron spectrum of a complex target using the phase-of-the-phase.*  
Poster title: *QPROP 3.0: an improved t-SURFF 2.0 algorithm for a trusted Schrödinger solver.*
8. Nov 27 – Nov 30 2018. International Workshop on Atomic Physics, Dresden, Germany.  
Poster title: *Extraction of laser-coherent information from a photoelectron spectrum of a complex target using the phase-of-the-phase.*
9. Jul 16 - Jul 20 2018. 27th annual International Laser Physics Workshop (LAS-PHYS2018), Nottingham, UK.  
Oral talk: *Revealing Coherent Information from a Photoelectron Spectrum of a Complex Target*

10. Feb 19 - Feb 22 2018. EAS - Extreme Atomic Systems, Riezlern, Austria.  
Oral talk: *Optimization of THz currents induced in strong laser circularly polarized fields.*
11. Nov 27 – Dec 2, 2016. International Workshop on Atomic Physics (atom2016), Dresden, Germany.  
Poster title: *Complex-time soft recollisions in strong field ionization of atoms.*
12. Apr 18 – Apr 23, 2016. V International youth scientific school-conference “Modern problems of physics and technology”, Moscow, Russia.  
Poster title: *Invariant method for evaluating the Coulomb-corrected action of the electron in the intense laser field.*
13. Apr 5 – Apr 7, 2016. V International conference “Problems of mathematical and theoretical physics and mathematical modelling”, Moscow, Russia.  
Oral talk: *Invariant method for evaluating the Coulomb-corrected action of the electron in the intense laser field.*
14. Aug 21 – Aug 25, 2015. 24th Annual International Laser Physics Workshop (LAS-PHYS’15), Shanghai, China.  
Oral talk: *Optimization of terahertz currents induced in atomic gases by intense bichromatic laser fields.*

## ABBREVIATIONS

ATI	above-threshold ionization
CEP	carrier-envelope phase
$\circ\circ$	counter-rotating circular
$\circ\circ$	corotating circular
$\circ\updownarrow$	circular and linear
HHG	high-harmonic generation
IR	infrared
iSURFV	infinite-time surface-flux method with Volkov functions
$\updownarrow\updownarrow$	co-linear
MC	Monte Carlo
MIR	mid-infrared
NIR	near-infrared
PES	photoelectron spectrum
PIC	particle-in-cell
PoP	phase-of-the-phase
QTMC	quantum-trajectory Monte Carlo
RPC	relative phase contrast
SAE	single active electron
SFA	strong-field approximation
SMM	simple-man's model
TDSE	time-dependent Schrödinger equation
THz	terahertz
TOF	time-of-flight
tSURFF	time-dependent surface-flux method
UV	ultraviolet
WOM	window-operator method
XUV	extreme ultraviolet

## INTRODUCTION

Since their prediction in the 1950s and invention in the 1960s, lasers have covered an ultra-wide list of various applications in all spheres of life ranging from low-power diode lasers daily used in barcode readers in grocery stores and in optical disk drives to ultrahigh-power multi-beam facilities aimed to study the matter at extreme conditions and in perspective to gain control over the inertial confinement fusion. Occupying the middle of this hierarchy, the table-top or room-size laser-based setups operating at peak intensities of about  $10^{12} - 10^{15} \text{ W/cm}^2$  are in charge of modern investigations in the area of strong-laser-induced matter ionization and subsequent processes. Here, the term ‘strong’ reflects that the non-linear interaction of an electromagnetic field with particles of the medium cannot be described perturbatively with respect to the field strength.

One of the key utilities in such experiments is the mechanism of temporal and spectral transformation of the initial radiation. Two opposite branches with different physics behind them should be named here. First is the mechanism of high-harmonic generation (HHG) which by its name indicates that the initial laser pulse energy is partially converted to higher frequency coherent radiation. By controlling and optimizing the initial laser beam properties and subsequent filtering of the produced radiation, fine tuning of the latter is performed providing a high-quality source with desired spectral properties covering the extreme ultraviolet (XUV) or even soft X-ray domains. An incident of the HHG process mainly proceeds on a sub-laser-cycle timescale and results in a burst of radiation that is narrow in time. The HHG mechanism is intrinsic both to gas and solid phases of matter, the correspondent branches of research mainly develop correlatively and are often discussed jointly in the literature.

On the other hand, the interaction of a strong laser field with gaseous matter may lead to creation of the radiation at incomparably lower frequencies. The responsible mechanism is essentially macroscopic. Here the keystone is the collective movement of the electrons in the plasma remaining after the interaction with the laser. The characteristic frequency of oscillations is then determined by the density of the plasma, which is related to the ionization probability. This frequency does not depend on the spectral properties of the initial laser pulse directly and, thus, does not inherit those. Starting with a laser pulse of a near-infrared (NIR) and mid-infrared (MIR) frequency, one may create by such mechanism a source of radiation operating at hundreds or even thousands times slower frequencies lying in the terahertz (THz) domain.

In both XUV and THz generation cases, the laser-induced electron-ion interaction plays a role of an indispensable facilitator. Therefore, a comprehensive study of the photoelectron movement is key to understanding both processes and advancing the control over them. The responsible branch of theoretical and experimental investigations is called photoelectron spectroscopy. Besides fulfilling the goal of analysis and optimization of the above-mentioned mechanisms of radiation conversion, studies of photoelectron spectrum (PES) answer additional questions about the matter properties hidden in the set of inter-

playing features in those spectra. Since the de Broglie wavelength for a 10–100 eV electron is of the order of one Ångström ( $10^{-10}$  m) while for a 10–100 eV photon the wavelength is over a hundred times higher value, measurement with the help of electron beams technically can provide better spatial resolution than with beams of photons of the same energy. Eventually, this allows to probe the matter at natural scales of atomic systems. To wind up, extensive examination of the properties of PES does not only provide knowledge that is further useful in the optimization of coherent radiation frequency conversion schemes: PES are valuable by themselves as a repository of structural information about atomic and molecular targets encrypted in them. Thus, theoretical research of the properties of PES related to the parameters of the laser pulse and of the irradiated target occupies a central place of the present thesis.

Despite that the range of topics being the core of the different parts of the thesis is relatively wide, they overlap on the ground of laser fields under consideration: in most examples the focus is on two-color fields, consisting of a main component with frequency  $\omega_1$  and a second component with frequency  $\omega_2$ , forming a periodic joint field. Typically, but not only, the intensity of the second component is taken relatively weak. From the theoretical point of view it allows to treat its effect on the PES perturbatively and often provides closed-form expressions that allow to optimize for desired properties. From the experimental point of view, a setup with such a two-color laser where one component is weak is rather simple to establish. Experimental adjustment of the relative time delay between the components with different frequency at an attosecond timescale is easily achieved. Therefore, application of a two-color configuration allows for precise control over the ionization dynamics and over the subsequent motion of photoelectrons at almost no additional cost. To this end, the thesis mainly bases on investigations of strong-field physics with two-color laser-fields.

The structure of the thesis is as follows. In Chapter 1, further used approximations are stated, and the general theoretical background is introduced. Starting with the basics concepts of the so-called strong-field approximation (SFA), a variety of specific ionization scenarios are briefly introduced, which are subsequently applied in the follow-up chapters. The next part of the introductory Chapter addresses the purely numerical approach to calculate PES. The concepts of the surface-flux methods are mentioned and some examples based on the self-developed software that was used are provided.

Chapter 2 is devoted to a modern technique of characterization of PES called phase-of-the-phase (PoP) spectroscopy. In particular, an extension of this technique to a wider variety of laser field configurations is introduced, and examples of two specific applications of this technique are given. Firstly, a way to calibrate the parameters of a laser field in focus with the help of the PoP technique is proposed. Secondly, it is demonstrated that using the PoP one may subtract the laser-coherent part from a spectrum that has a dominant incoherent contribution.

Chapter 3 is devoted to the application of two-color laser fields in a plasma-based source of coherent THz radiation. In particular, configurations for which the power of the output THz radiation is optimized are proposed. Firstly, for the most commonly

used case of two-color co-linearly polarized pulses, the optimal intensity ratio is defined. Secondly, for otherwise polarized pulses the optimization with respect to polarizations is performed. Thirdly, for laser pulses with optimal polarization, the benefit of applying long-wavelength laser pulses is demonstrated. The results are in good agreement with experimental observations.

Chapter 4 is devoted to a new theoretical approach to the characterization of numerically obtained PES. In the era of continuous progress in designing new powerful laser sources, the generation of shorter and shorter pulses holds a special place. Correspondingly, a demand on the theoretical background providing a detailed description of the rich dynamics happening within a narrow span of time is also growing. The theory is here faced with a dilemma — the results it may provide are either based on simplified models which might not be predictive enough or on modelling that requires an immense computational power, thus, rendering a thorough parametric study prohibitive. And even when it is affordable, the outcomes of such calculations are hardly interpreted in a simple way. In Chapter 4, a step towards understanding this ‘black-box nature’ of time-dependent Schrödinger equation (TDSE) solvers is made, demonstrating the fingerprints of the classical photoelectron motion in the build-up of PES in the time-resolved quantum simulation of strong-field ionization rather than discussing signatures in the final, time-integrated result.

The last Chapter summarises the results and includes a short outlook.

# CHAPTER 1

## BASIC THEORY AND APPROXIMATIONS

### 1.1 SINGLE-ACTIVE-ELECTRON TREATMENT

*Helium is a multi-electron system  
with at least one electron too much.*  
(D. Bauer)

The general process of non-relativistic strong-laser-induced ionization is formally described by a solution to a many-particle Schrödinger equation. Unfavorably high complexity of this problem even in the two-electron system compared to a single-electron case often leaves a comprehensive study impossible apart from using the approximation of single active electron (SAE) which is assumed throughout this work. The effect of all electrons besides the SAE is approximately accounted for via the time-independent negative charge density partially screening the potential of the nucleus (this approach is often referred to as “frozen core” approximation, and any other correlations between the active and frozen electrons are disregarded).

If the length scale of the problem is considerably smaller than the wavelength of the laser, one may omit the dependence of the laser on the coordinates and treat the interaction in the dipole approximation. The laser field strength can be expressed via its vector potential  $\mathbf{A}(t)$  as  $\mathbf{E}(t) = -\partial_t \mathbf{A}(t)$ . The interaction between the electron and the laser is described as<sup>1</sup>

$$\hat{V}_{\text{int}} = \frac{2\hat{\mathbf{p}}\mathbf{A}(\mathbf{t}) + \mathbf{A}^2(\mathbf{t})}{2} \quad (1)$$

within the so-called velocity gauge, and the interaction with the residual ion is dictated by potential energy term  $U(\mathbf{r})$ . The central equation of interest, the time-dependent Schrödinger equation (TDSE), reads

$$i\partial_t |\psi(t)\rangle = \left[ \frac{\hat{\mathbf{p}}^2}{2} + \hat{V}_{\text{int}}(\mathbf{r}, t) + U(\mathbf{r}) \right] |\psi(t)\rangle. \quad (2)$$

Let us start with an electron in a bound state  $|\psi_{\text{bound}}(0)\rangle$ . Due to the process of the laser-atom interaction, this electron can occupy continuum states with some probability and the wavefunction is then

$$|\psi(t)\rangle = |\psi_{\text{bound}}(t)\rangle + |\psi_{\text{free}}(t)\rangle. \quad (3)$$

---

<sup>1</sup> Here and later on atomic units  $e = m_e = \hbar = 4\pi\epsilon_0 = 1$  are assumed unless other units are explicitly given.

The latter term can be presented in a form of an integral over momentum space:

$$|\psi_{\text{free}}(t)\rangle = \int d\mathbf{k} |\mathbf{k}\rangle \langle \mathbf{k} | \psi(t) \rangle \quad (4)$$

with  $|\mathbf{k}\rangle$  being the exact continuum eigenstates in a given potential. The main quantity of interest here is the ionization amplitude defined as a projection

$$a_{\mathbf{k}}(t) = \langle \mathbf{k} | \psi(t) \rangle. \quad (5)$$

The photoelectron momentum distribution (or photoelectron spectrum (PES)) is defined as

$$Y(\mathbf{k}, t) = |a_{\mathbf{k}}(t)|^2, \quad (6)$$

and the total ionization probability is given by integration of (6) over momentum space.

## 1.2 STRONG-FIELD APPROXIMATION

*Simple is better than complex.*

*Complex is better than complicated.*

(T. Peters, The Zen of Python)

The general analytic solution to the TDSE where both the binding potential and the laser field are present does not exist in closed form. Let us start from the analytic treatment and introduce the basics of the strong-field approximation (SFA) [1–3], a theoretical approach that has well recommended itself through decades as capable of producing qualitatively (and in some cases quantitatively) correct results in a closed-form. The core assumption of the SFA is that after the instant of ionization an electron is treated as propagating only in the external laser field while the influence of the binding potential of the parent ion is neglected. Photoelectrons that do not rescatter at the parent ion are called “direct”. The probability amplitude for such a process reads [4–6]

$$a_{\mathbf{k}}(T) = -i \int_0^T dt \langle \Psi_{\mathbf{k}}^V(t) | \mathbf{r} \cdot \mathbf{E}(t) | \Psi_0(t) \rangle. \quad (7)$$

Here,  $T$  is the laser pulse duration,  $|\Psi_0(t)\rangle = |\psi_0\rangle \exp(iI_p t)$  is the initial state with the ionization energy  $I_p$  and

$$|\Psi_{\mathbf{k}}^V(t)\rangle = \exp(-iS_{\mathbf{k}}^V(t)) |\mathbf{k} + \mathbf{A}(t)\rangle \quad (8)$$

is the Volkov function [7] describing the the state of a free electron in an external laser field <sup>2</sup>. The function in the exponent,

$$S_{\mathbf{k}}^V(t) = \frac{1}{2} \int_0^t dt' [\mathbf{k} + \mathbf{A}(t')]^2, \quad (9)$$

---

<sup>2</sup> Here and after the notation  $|\mathbf{k}\rangle$  in the SFA formulas refers to a plane wave and not an exact continuum eigenstate as the influence of the binding potential is neglected.

has a form of the classical action for such an electron. The resulting expression for the ionization amplitude (7) takes the form of a time integral

$$a_{\mathbf{k}}(T) = \int_0^T dt P(\mathbf{k}, t) \exp(-iS(\mathbf{k}, t)), \quad (10)$$

where

$$S(\mathbf{k}, t) = \int_t^\infty dt' \left( \frac{[\mathbf{k} + \mathbf{A}(t')]^2}{2} + I_p \right). \quad (11)$$

Throughout the thesis the following form of a vector potential will be used:

$$\begin{aligned} \mathbf{A}(t) = A_0 f(t) & \left[ \left( \cos(a\omega t) + \xi \cos(b\omega t + \phi) \right) \mathbf{e}_x \right. \\ & \left. + \left( \epsilon_a \sin(a\omega t) + \epsilon_b \xi \sin(b\omega t + \phi) \right) \mathbf{e}_y \right]. \end{aligned} \quad (12)$$

The temporal duration and form of the pulse is dictated by the envelope  $f(t)$ , which is assumed to be vanishing at  $t \rightarrow \pm\infty$ . The ellipticity of each component is defined via  $\epsilon_{a,b}$ . If the fields are elliptic and rotate in the same direction,  $\epsilon_{a,b}$  are of the same sign. Linearly polarized fields have  $\epsilon = 0$ . For them, the ratio of vector potential amplitudes between the  $\omega$  and  $b\omega$  components reads  $1 : \xi$  but the field strengths relate as  $a : b\xi$ , and the intensities – as  $a^2 : (b\xi)^2$ . Intensity of each elliptical field is  $(1 + \epsilon^2)$  times higher than of a linearly polarized one with the same  $A_0$ . The remaining parameter  $\phi$  defines the relative phase.

Depending on how the characteristic atomic and laser energies relate, the ionization dynamics can be explained differently. As an indicator of the ionization scenario the so-called Keldysh parameter [1]

$$\gamma = \frac{\sqrt{2I_p}}{A_0} \quad (13)$$

is used distinguishing between the multiphoton ( $\gamma \gg 1$ ) and tunneling ( $\gamma \ll 1$ ) regimes. In the multiphoton regime the ionization is determined by the quantum nature of the laser-matter interaction resulting in the absorption of a discrete number of photons. In the opposite limit of small  $\gamma$  the electron starts its motion by tunneling through the barrier formed by the potential of the residual atom together with the strong laser field and continues with the laser-driven motion almost free from the core's influence. This description is often called simple-man's scenario for the above-threshold ionization (ATI) process. In fact, such an intuitively transparent semiclassical approach with quantum initial conditions and classical post-tunneling electron motion is capable of giving a fruitful insight into the predictions of quantum theories. Let us briefly describe its main aspects below.

### 1.2.1 CLASSICAL TRAJECTORIES AND QUANTUM INTERFERENCE

The photoionization amplitude (10) defined above within the SFA in a form of an integral over time gains its value in the vicinity of certain instants specific for each value of the final momentum  $\mathbf{k}$ . No restriction is made on possible  $\mathbf{k}$ , however, going far away from certain values leads to exponentially small probabilities. As such exponential damping of

the probability is a common quantum behaviour in parameter regimes that are forbidden classically, it is natural to derive the semiclassical limit for the photoionization process as follows. In the zero-range potential (which is the one assumed by the SFA), one replaces the initial quantum electron wavefunction by a classical point-like particle located at  $\mathbf{r} = 0$  with velocity  $\mathbf{v}(t) = \mathbf{k} + \mathbf{A}(t)$  being also zero initially at time  $t_s$ . Thus, the canonical momentum  $\mathbf{k}$  is equal to  $-\mathbf{A}(t_s)$ . The classical equations of motion

$$\mathbf{r}(t) = \int_{t_s}^t dt' \mathbf{v}(t'), \quad (14)$$

$$\mathbf{v}(t) = - \int_{t_s}^t dt' \mathbf{E}(t'). \quad (15)$$

determine the subsequent dynamics of an electron. Such a treatment restricts the possible momenta to

$$\min |\mathbf{A}(t)| \leq k \leq \max |\mathbf{A}(t)|, \quad (16)$$

exaggerating the exponential decay predicted by the SFA. However, this still gives no information about the relative probabilities for ionization with momenta within this range. Those still have to be defined according to some quantum prediction. In particular, it is common to estimate it within the long-wavelength limit of the PPT formula (named after Perelomov, Popov and Terent'ev who introduced it in [8])<sup>3</sup>:

$$\partial_t Y(t_s) \sim \exp(-\text{const}/|\mathbf{E}(t_s)|). \quad (17)$$

Such a combination of classical electron movement and instantaneous ionization is called simple-man's model (SMM). While in the tunneling regime the constant in Eq. (17) reads  $\frac{2}{3}(\sqrt{2I_p})^3$ , it can be derived for moderate Keldysh parameter values  $\gamma \sim 1$  (see Eq. (33) below and [10]). The main takeout here is that in the classically allowed domain of momenta (16) the PES is expected to reach the highest values around momenta such that  $\mathbf{k} = -\mathbf{A}(t_0)$  where  $t_0$  stands for times close to those where the peaks of  $|\mathbf{E}(t)|$  are. The SFA-predicted PES for two particular examples of linear and circular fields are displayed in Fig. 1.1. They are complemented by classical-theory predictions for most probable momenta. Not surprisingly, a good qualitative agreement between the two approaches is observed.

It is worth mentioning, that such a seemingly very simplistic treatment can give more than just a rough estimate for the shape of the PES. In fact, SMM serves as a good starting point for advanced Monte Carlo (MC) simulations that “upgrade” the classical picture by introducing the quantum nature of the initial spatial distribution of electrons or even by including the quantum interference between different trajectories on a qualitative level. The latter could be, for example, achieved by summing up the weights of trajectories,

---

<sup>3</sup> Which is the tunneling or quasistatic limit and requires  $\gamma \ll 1$ . The correspondent formula is also often called in the literature ‘ADK-rate’ formula named after Ammosov, Delone and Krainov who re-derived it in [9].

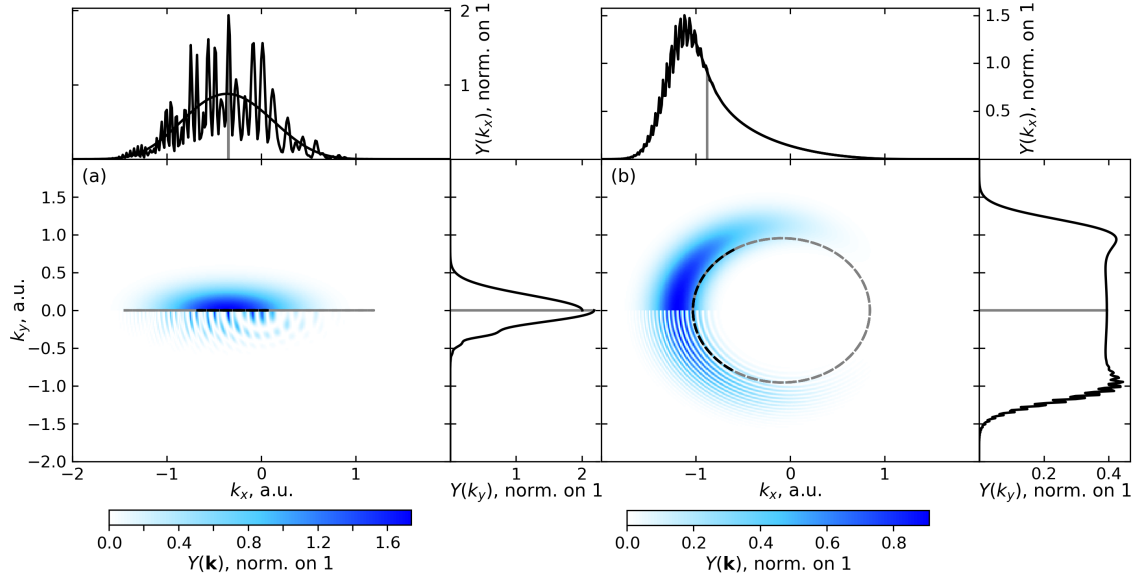


**Figure 1.1:** Spectra of 'direct' photoelectrons from argon in a laser field of intensity  $I = 2 \cdot 10^{14} \text{W/cm}^2$  and wavelength  $\lambda = 800 \text{ nm}$  with a weak ( $\xi = 0.1$ ) 400 nm component added. The polarization of the laser components is either (a) co-linear ( $\uparrow\uparrow$ ) or (b) corotating circular ( $\odot\odot$ ). Dashed gray lines represent the vector potential with inverse sign,  $-\mathbf{A}(t)$ . Dashed black lines correspond to values of  $-\mathbf{A}(t)$  at times  $t$  such that  $|\mathbf{E}(t)|$  is greater than 80% of its maximum. Upper parts of the density maps show the SFA-based calculations with the interference between the saddle points removed, lower parts include interference emerging within two optical cycles of the laser pulse. The average momentum (gray lines in the 1D distributions) experiences no notable change when this interference is neglected.

modified with phase factors defined by classical actions:

$$Y(\mathbf{k}, t) = \left| \sum_n \delta(\mathbf{v}_n(t) - (\mathbf{k} + \mathbf{A}(t))) e^{-iS(\mathbf{v}_n(t), t_{s,n}, t)} \right|. \quad (18)$$

In practise, even smallest differences in velocities  $v$  of electrons cause the fading of interference at long times due to the continuously raising difference of phases  $S$ . To preserve the interference, a modification of Eq. (18) could be adapted. There, each electron is launched at an ionization time  $t_s$  being distributed equally. Its contribution to the final PES is weighted by the tunneling probability  $w(t_{s,n})$ . A histogram  $Y(\mathbf{k}, t = \infty) = \sum_{\mathbf{k}_n \approx \mathbf{k}} w(t_s)$  representing the final distribution is then replaced by

$$Y(\mathbf{k}, t = \infty) = \left| \sum_{\mathbf{k}_n \approx \mathbf{k}} \sqrt{w(t_{s,n})} e^{-iS(\mathbf{v}_n(t), t_{s,n}, t=\infty)} \right|^2. \quad (19)$$

Such methods are called quantum-trajectory Monte Carlo (QTMC) in the literature [11]. In case of chaotic phases  $S$  both formulas (18) and (19) coincide. Depending on the task set, such an approach may be advantageous in areas where the spectrum cannot be predicted by using the regular SFA.

Besides components parallel to the laser polarization, initial momenta are complemented by perpendicular components  $\mathbf{k}_\perp$  defined according to the respective tunneling limit of the PPT formula, resulting eventually in the following expression for the instantaneous tunneling ionization rate:

$$Y(\mathbf{k}, t) \sim \exp\left(-\frac{2(\sqrt{2I_p})^3}{3|\mathbf{E}(t)|}\right) \exp\left(-\frac{2\sqrt{2I_p}\mathbf{k}_\perp^2}{|\mathbf{E}(t)|}\right) \delta(\mathbf{k}_\parallel + \mathbf{A}(t)). \quad (20)$$

If the motion of the electrons takes place under the influence of a force that is described by a short (or zero) range potential, the scattering can be modelled by probabilistic instantaneous velocity rotation if the trajectory passes close to the origin (the impulse approximation). An example calculation is demonstrated in Fig. 1.2 where the quantum interference is accounted for.

Thorough examinations of various structures weaved in the interference carpet of PES have been carried out [12–19]. As key physics-controlling observables in the experimental research are often macroscopic in nature, tiny structures risen at the microscopic level eventually smear away or get distorted once averaging over the focal volume is performed (see, e.g., [20–23]). This averaging is hardly avoidable as experiments with high-intensity laser beams require tight focusing. If integral quantities are of main interest, the interference patterns all the more are secondary as is demonstrated by the examples shown in Fig. 1.1. In this regard, the present thesis does not aim on the precise description of quantum interferences restricted to specific laser configurations. The focus is on global properties instead.

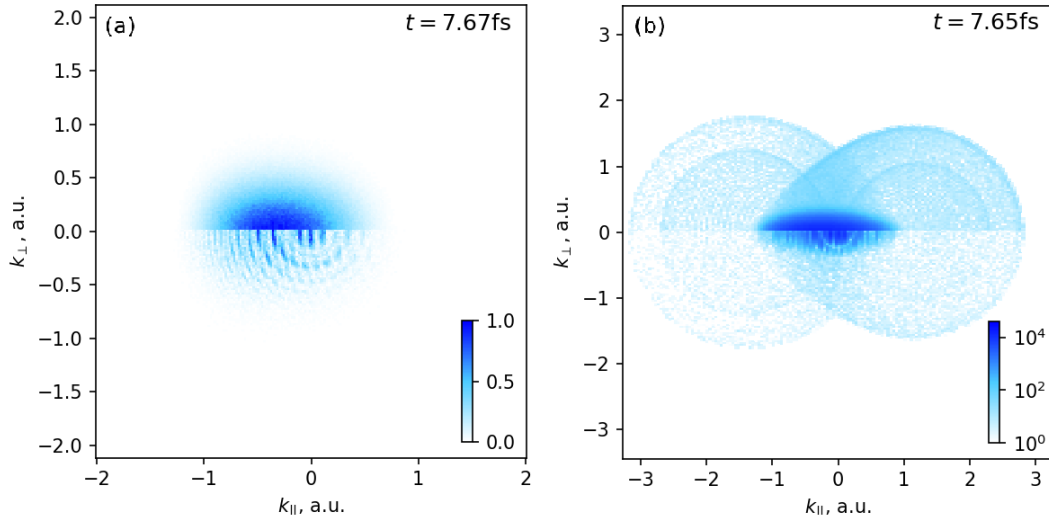


**Figure 1.2: PES in a two-color field as from Fig. 1.1(a) but calculated with CTMC including (a) 'direct' electrons only; (b) 'direct' and scattered electrons. Bottom parts of each subplot accounts for quantum interference according to Eq. (18) with  $S(\mathbf{v}_n(t), t_{s,n}, t) = \int_{t_{s,n}}^t \left[ \frac{(\mathbf{v}_n(t'))}{2} + I_p \right] dt'$ . Laser parameters are the same as in Fig. 1.1(a). The scale in (b) is logarithmic due to low ratio between scattered and non-scattered electrons.**

### 1.2.2 SADDLE-POINT METHOD

The derivation of closed-form analytic expressions for the yield is often based on the limit of (infinitely) long laser pulses. In that case, the ionization rate is considered, which is defined as

$$\partial_t Y(\mathbf{k}) \simeq \lim_{T \rightarrow \infty} \frac{|a_{\mathbf{k}}(T)|^2}{T} \sim \left| \int_0^{2\pi/\omega} dt P(\mathbf{k}, t) \exp(-iS(\mathbf{k}, t)) \right|^2 \quad (21)$$

where  $2\pi/\omega$  is one optical period of a laser. The contribution of multiple neighboring optical periods eventually leaves this expression non-vanishing only at energies in the vicinity of those fulfilling energy conservation:

$$\frac{k_n^2}{2} = n\omega - (I_p + U_p), \quad n = N_{\min}, N_{\min} + 1, \dots \quad (22)$$

The correspondent pattern in the spectrum is called ATI-peak pattern and is most pronounced for multiphoton laser conditions when a small number of ATI peaks forms the whole spectrum. The minimum number of photons  $N_{\min}$  is defined by the target through the ionization energy  $I_p$  and by the laser intensity through the ponderomotive energy

$$U_p = \frac{1}{T} \int_T dt \frac{A(t)^2}{2} \quad (23)$$

being the average kinetic energy of an electron oscillation in the given electric field.

The time integral in (21) can be often performed with the saddle-point method [4, 6,

24, 25], which bases on assumption that the exponential factor  $\exp(-iS(\mathbf{k}, t))$  oscillates much faster than the pre-exponential factor  $P(\mathbf{k}, t)$ . The integral than boils down to contributions from a finite number (or in the case of infinitely long pulses – to a countable set) of instants in time, the saddle-points:

$$\partial_t Y(\mathbf{k}) \sim \left| \sum_s M_{\mathbf{k}}(t_s) \right|^2 = \left| \sum_s P(\mathbf{k}, t_s) \exp(-iS(\mathbf{k}, t_s)) \right|^2. \quad (24)$$

These times  $t_s$  are complex solutions to the saddle-point equation

$$[\mathbf{k} + \mathbf{A}(t_s)]^2 + 2I_p = 0. \quad (25)$$

If the ionization potential is neglected here, this equation coincides with the classical distribution of canonical momenta.

It is convenient to introduce the following dimensionless units for time, momentum, and energy:

$$a\tau = a\omega t_s - \alpha, \quad \mathbf{q} = \frac{\mathbf{k}_\perp}{A_0}, \quad q_z = \frac{k_z}{A_0}, \quad \gamma^2 = \frac{2I_p}{A_0^2}. \quad (26)$$

Here,  $\alpha$  is the angle between momentum vector  $\mathbf{k}_\perp$  in the  $x$ - $y$  plane and the  $x$  axis,  $\gamma$  is the Keldysh parameter (13). In dimensionless units (26) the saddle-point equation reads

$$[\mathbf{q} + \mathbf{A}(t_s)/A_0]^2 + \gamma^2 = 0. \quad (27)$$

Apart from few specific cases, the results within the SFA, even with the saddle-point method involved, cannot be obtained in a closed form, and solutions to the saddle-point equation (25) need to be found numerically. Nevertheless, as no universal solution to the problem of searching for complex roots of an arbitrary function exists, it is worth doing few analytic steps for the simplest cases and to derive useful starting points for more complicated ones.

### 1.2.3 SADDLE POINTS IN A MONOCHROMATIC LASER FIELD

Taking, in particular, the solutions for the single-color infinitely long laser pulse provides goods seeds for a numerical search of the saddle points in a configuration with an addition of a weak second component. It is worth mentioning that the set of solutions defined for a single-color field would not exhaust the set of those for a two-color case. However, the dominant contribution to the ionization amplitude would be successfully captured.

We start with two simplest examples. Firstly, let us take the laser pulse (12) with a constant envelope  $f(t) = 1$ . If no second color is present ( $\xi = 0$ ) and the polarization of the remaining field is circular ( $\epsilon_a = 1$ ), the saddle-point equation (27) reads

$$2q \cos(a\tau) + 1 + \gamma^2 + q_z^2 + q^2 = 0 \quad (28)$$

and has a single physical solution (i.e., such that has non-negative imaginary part and gives

not a large but an exponentially small yield), which is periodically repeated each optical cycle [8, 26]:

$$a\tau^{(0)} = \pi + ia\tau_i^{(0)} = \pi + i \cosh^{-1} \left( \frac{1 + \gamma^2 + q_z^2 + q^2}{2q} \right). \quad (29)$$

Inserting this expression in (11) gives the imaginary part of the action equal to

$$\text{Im}S(q, \tau) = -\frac{A_0^2}{2a\omega} \left\{ \left( 1 + \gamma^2 + q_z^2 + q^2 \right) a\tau_i^{(0)} - 2q \sinh(a\tau_i^{(0)}) \right\}. \quad (30)$$

The resulting ionization rate (24) displays a fast decay of the photoionization probability with increase of  $|q_z|$ , i.e., outside of the laser  $x$ - $y$  polarization plane [3, 8]. Thus, it is sufficient to restrict the further analysis of PES to the  $x$ - $y$  plane only. Additionally, the influence of non-zero momentum  $q_z$  can be taken into account by introducing the effective  $\tilde{\gamma} = \sqrt{\gamma^2 + q_z^2}$ .

If a monochromatic field ( $\xi = 0$ ) has a polarization different from circular ( $\epsilon^2 < 1$ ), each optical cycle contains two saddle points [24]. For a pulse polarized linearly along the  $x$  axis ( $\epsilon_a = 0$ ), the saddle-point equation (25) reads (hereafter  $a = 1$  without loss of generality)

$$(q_x + \cos(\tau))^2 = \tilde{\gamma}^2 \quad (31)$$

where  $\tau = a\omega t_s$  and  $\tilde{\gamma} = \sqrt{\gamma^2 + q_z^2}$ . The two solutions per optical cycle are

$$\tau^{(0)} = \pm \frac{\pi}{2} \pm \sin^{-1}(q_x \pm i\tilde{\gamma}) = \pm \frac{\pi}{2} + i \sinh^{-1}(\tilde{\gamma} \mp iq_x). \quad (32)$$

The signs are chosen such that  $\text{Im}\tau > 0$ . For each of them the imaginary part of the action (11) is then

$$\text{Im}S(\mathbf{q}, \tau) = -\text{Im} \frac{A_0^2}{2\omega} \left\{ \left( \frac{1}{2} + \tilde{\gamma}^2 + q_x^2 \right) \tau^{(0)} - 2q_x \sin(\tau^{(0)}) - \frac{1}{4} \sin(2\tau^{(0)}) \right\}. \quad (33)$$

The highest probability corresponds to zero  $q_{\parallel}$  momentum, and there the imaginary part of the action reads [10]

$$\text{Im}S(q_{\parallel} = 0, \mathbf{q}_{\perp}, \tau) = -\frac{A_0^2}{2\omega} \left\{ \left( \frac{1}{2} + \tilde{\gamma}^2 \right) \sinh^{-1}(\tilde{\gamma}) - \frac{1}{2} \tilde{\gamma} \sqrt{1 + \tilde{\gamma}^2} \right\}. \quad (34)$$

Assuming the tunneling limit and small  $q_{\perp}$  momenta one gets the correspondent formula (20) where the perpendicular momentum distribution can be approximately treated as Gaussian.

#### 1.2.4 PHOTOELECTRON SPECTRA IN TWO-COLOR COUNTER-ROTATING CIRCULARLY POLARIZED ( $\odot\odot$ ) FIELDS

Armed with analytic predictions for the single-color laser case, one may proceed towards the derivation of PES in two-color fields that will be useful in the next chapters. We start with a field consisting of a strong  $a\omega$  component and a weak  $b\omega$  component. It is worth noticing that if the influence of the second color is significant such that none of the two

field components can be fruitfully treated as a perturbation to the other, our derivations can still provide the results of interest after recursive substitution of intermediate values as initial conditions for a numerical search. Crucially, the solving procedure for a saddle-point equation should in such a case be initialized with the lower frequency component being turned off, because otherwise part of the important saddle points might be lost. Last but not least, in some cases the saddle points may approach each other, violating the applicability of the general saddle-point method. In this case, the uniform approximation should be applied instead [24].

Keeping in mind these remarks, let both laser field components be circularly polarized and rotate in opposite directions ( $\epsilon_a = 1$ ,  $\epsilon_b = -1$ ). As discussed above, the classical theory predicts that the PES inherits the symmetry properties of the driver laser. Following this symmetry of the  $a\omega$ - $b\omega$  field, it is convenient to introduce an angle combining the emission angle  $\alpha$  and the phase shift  $\phi$ :

$$a\theta = a\phi + (b+a)\alpha. \quad (35)$$

Now, the saddle-point equation (25) reads

$$\begin{aligned} 2q \cos(a\tau) + 1 + \gamma^2 + q^2 \\ + \xi^2 + 2\xi[q \cos(b\tau + \theta) + \cos((a+b)\tau + \theta)] = 0, \end{aligned} \quad (36)$$

and the action (11) in the exponent for the SFA photoionization amplitude is equal to

$$\begin{aligned} S(q, \tau) = \frac{A_0^2}{2a\omega} \left[ (1 + \gamma^2 + q^2)a\tau + 2q \sin(a\tau) \right. \\ \left. + \xi^2 a\tau + 2\xi \left( q \frac{a}{b} \sin(b\tau + \theta) + \frac{a}{a+b} \sin((a+b)\tau + \theta) \right) \right] \Bigg|_{\tau=0}^{\tau=\tau_s}. \end{aligned} \quad (37)$$

The resulting spectrum inherits the  $(b+a)$ -fold symmetry from the driver laser and experiences a global rotation in the polarization plane according to  $\phi$ . In the present thesis, such a type of laser fields is further considered in the context of the analytical study of PES using the so-called phase-of-the-phase (PoP) spectroscopy, which Chapter 2 is devoted to.

### 1.2.5 PHOTOELECTRON SPECTRA IN TWO-COLOR CO-ROTATING CIRCULARLY POLARIZED ( $\odot\odot$ ) FIELDS

Another configuration considered further in the thesis is a two-color field with co-rotating circular polarizations of its components ( $\epsilon_a = 1$ ,  $\epsilon_b = 1$ ). While the PES are substantially different compared to the counter-rotating case, the analytical formulas are similar. Namely, it is enough to replace  $(b, \phi, \theta)$  by  $(-b, -\phi, -\theta)$  in Eqs. (35)–(37). Analogously to Eq. (35) one introduces a variable

$$a\theta = a\phi + (b-a)\alpha, \quad (38)$$

which turns the saddle-point equation (36) to

$$\begin{aligned} & 2q \cos(a\tau) + 1 + \gamma^2 + q^2 \\ & + \xi^2 + 2\xi[q \cos(b\tau + \theta) + \cos((b-a)\tau + \theta)] = 0, \end{aligned} \quad (39)$$

and the action (37) – to

$$\begin{aligned} S(q, \tau) = & \frac{A_0^2}{2a\omega} \left[ (1 + \gamma^2 + q^2)a\tau + 2q \sin(a\tau) \right. \\ & \left. + \xi^2 a\tau + 2\xi \left( q \frac{a}{b} \sin(b\tau + \theta) + \frac{a}{b-a} \sin((b-a)\tau + \theta) \right) \right] \Big|_{\tau=0}^{\tau=\tau_s}. \end{aligned} \quad (40)$$

Again, the PES obeys the  $(b-a)$ -fold symmetry as does the laser field and turns globally with  $\phi$ . Such laser field configurations will be further discussed in Chapter 3 where their benefits in the generation of terahertz (THz) radiation in plasmas will be addressed.

### 1.2.6 PHOTOELECTRON SPECTRA IN TWO-COLOR COLINEARLY POLARIZED ( $\Updownarrow\Updownarrow$ ) FIELDS

For co-linearly polarized two-color laser fields ( $\epsilon_{a,b} = 0$ ) evaluating the integral in (21) within the saddle-point approximation gives a saddle-point equation (27) of the form

$$[q_x + \cos(a\tau_s) + \xi \cos(b\tau_s + \phi)]^2 = -(\gamma^2 + q_\perp^2) \equiv -\hat{\gamma}^2. \quad (41)$$

If restricted to the simplest  $\omega$ - $2\omega$  case ( $a = 1, b = 2$ ), this equation has four solutions with a positive imaginary part in each optical period  $\text{Re}\tau_s \in [0, 2\pi[$  of a laser field (just as a  $2\omega$ -field would solely give two solutions per twice shorter cycle). Making use of the fact that in the limit  $\hat{\gamma} \gg 1$  the imaginary part of the saddle points behave approximately as

$$2 \cosh(\text{Im}\tau_s) \approx 2 \sinh(\text{Im}\tau_s) \approx \exp(\text{Im}\tau_s) \approx \hat{\gamma}, \quad (42)$$

one may find simple asymptotic expressions for those solutions [27]:

$$\tau_{s1,2} \approx \pi - \phi - i \ln(2\xi) + i \ln(1 - \sqrt{1 - 8\xi e^{-i\phi}(q_x \mp i\hat{\gamma})}), \quad (43)$$

$$\tau_{s3,4} \approx \pi - \phi - i \ln(2\xi) + i \ln(1 - \sqrt{1 + 8\xi e^{-i\phi}(q_x \mp i\hat{\gamma})}). \quad (44)$$

Approaching the limit  $\xi \rightarrow 0$ , the first two saddle points turn to the solutions  $\tau_{s1,2}$  for the monochromatic field while the other two solutions,  $\tau_{s3,4}$ , tend to infinity logarithmically as  $-i \ln \xi$ , eventually making vanishing contributions to the ionization probability.

The formulas derived above will be further used in Chapter 3 where the question of optimization of the two-color laser pulse will be addressed.

### 1.3 NUMERICAL SOLUTION TO THE TDSE WITH QPROP

Besides providing a benchmark for simplified models, a full numerical solution to the TDSE may give insight to ionization processes at parameters beyond the domain of applicability of approximate theories. Solving the TDSE numerically is often declared an ‘ab initio’ approach and is contrasted to ‘analytical’ methods, although these terms are often too pretentious [28]. Purely numerical calculations are in general demanding in terms of computational power and require sacrificing a part of their physical rigour in order for predictions to be affordable in reasonable time. Within the present thesis, the benchmarking TDSE-based calculations were performed using the free open-source software QPROP. The most important approximations made in QPROP are briefly discussed below.

#### 1.3.1 POTENTIALS IN QPROP

The commonly considered targets in the physics of laser-induced ionization are atomic and molecular gases. As mentioned above, for those it is often enough to treat the laser-atom interaction in the SAE approximation. In the versions of QPROP utilized within the present thesis, an additional restriction is made on the pseudo potential assuming it to be spherically symmetric. The simplest pseudo potential for a rare-gas atom has the form

$$U(r) = -\frac{1}{r} - \frac{Z_{\text{eff}} - 1}{r} e^{-cr} \quad (45)$$

with  $Z_{\text{eff}}$  being the effective charge (often close to the charge of the nucleus) and  $c$  being the screening parameter (typically of the order of 1). In all examples showing QPROP-based calculations for argon in the next chapters, (45) with  $Z_{\text{eff}} = 18$  and  $c = 2.2074$  will be assumed. This provides the ionization energy  $I_p = 15.8$  eV for the  $3p$  initial state on a radial grid with a resolution of  $dr = 0.1$ . In case of a hydrogen atom, the potential is, obviously,  $U(r) = -1/r$ . In computations aimed at a closer comparison of the results with the SFA prediction, a short-range potential will be adapted by removing the first, hydrogenic term from (45) and setting  $Z_{\text{eff}} = 5.2074$  and  $c = 5.0$  in the remaining screening term. Such potential supports a  $1s$  state with  $I_p = 13.6$  eV on the same radial grid. In principle, the choice of a pseudo potential is not unique and a specific formula can be designed to reproduce better the quantities of interest depending on the parameters of the numerical grid. A good compilation of alternative types of rare-gas atomic pseudo potentials aimed at different physical aspects can be found, for example, in [29]. One has to keep in mind that parameters for some of those were determined using numerical grids with rather tiny grid steps  $dr$ <sup>4</sup>. For targets other than rare-gas atoms formulas for pseudo potentials also exist. For example, the SAE potentials for alkali atoms and for one-valence-electron alkaline earth metals can be found in [31–33]. However, in the present thesis only noble gas atoms or atomic hydrogen will be considered.

---

<sup>4</sup> Special remark should be made on widely employed potentials from [30]: while for various strong-field-ionization scenarios a radial grid step  $dr \sim 10^{-1}$  provides acceptable accuracy for numerical simulations, for the heaviest rare gases the formulas from [30] should be used with caution as they work well only for  $dr \sim 10^{-3}$  or smaller.

Besides (45), a function  $U_{\text{im}}(r)$  is added to the potential in QPROP. This term is negative imaginary and is only non-zero at far distances  $r > R_{\text{im}}$  from the center. The inclusion of such a term into the Hamiltonian ensures the suppression of unphysical reflection from the numerical boundary  $r = r_{\text{max}}$  by causing a fast decay of a wavefunction propagating through it. Therefore, it is called a complex absorbing potential. By default, QPROP uses

$$U_{\text{im}}(r) = -iV_{\text{im,max}} \cdot \left( \frac{r - R_{\text{im}}}{W_{\text{im}}} \right)^{16} \Theta(r - R_{\text{im}}) . \quad (46)$$

Here,  $V_{\text{im,max}} > 0$  is the amplitude and  $W_{\text{im}} = r_{\text{max}} - R_{\text{im}}$  is the width;  $\Theta$  is the Heaviside function. An imaginary potential is not the only possibility to introduce absorbing boundary conditions but is simpler to implement than other methods like complex scaling [34, 35], a product of energy-specific absorbing operators [36] or representing open boundary conditions in integral form [37, 38].

### 1.3.2 REPRESENTATION OF A WAVEFUNCTION IN QPROP

Centrally symmetric binding potentials and the expansion of the wavefunction in spherical functions reduce the 3D TDSE down to a set of 1D radial equations that are coupled in presence of a laser field. The set of functions needed to describe the expansion

$$\langle \mathbf{r} | \psi(t) \rangle = \sum_{\ell m} R_{\ell m}(r, t) Y_{\ell m}(\Omega) \quad (47)$$

of the wavefunction is dictated by the polarization of the external laser field (e.g., if it is linear and along the  $z$  axis, different  $m$ -channels do not mix and their initial setting is conserved), its temporal characteristics and its intensity. A good estimate for the limit of  $\ell$  to be considered is the number of photons required to create photoelectrons with kinetic energies of interest:

$$\ell_{\text{max}} \gtrsim \frac{I_p}{\omega} + \frac{k^2}{2\omega} . \quad (48)$$

The maximum kinetic energy can be estimated by the classical cutoff for the photoelectron energy, which reads

$$\frac{k_{\text{max}}^2}{2} \lesssim 10U_p = 10 \frac{E_1^2}{4\omega^2} \quad (49)$$

in the case of a linearly polarized laser field [39]. Increasing the intensity or the wavelength of the driver laser pulse raises the computational complexity drastically. Numerical computations for mid-infrared (MIR) fields with  $\lambda \gtrsim 2 \mu\text{m}$  are quite challenging already at intensities  $I \sim 10^{14} \text{W/cm}^2$  and are hardly accessible for elliptically polarized pulses even at lower wavelengths. Fortunately, for some problems the SFA-based or even more simplified semiclassical theories can take up the baton in this parameter domain as they become more trustworthy in the quasistatic limit of ionization.

Besides the improvement of hardware in performance, the development of new methods for purely numerical calculations is also of big demand in the scientific society. The benefit of faster calculations is especially pronounced in the branches of strong-field-ionization research where big sets of simulated data are required as, for example, in studies based on

machine learning that gained increased attention in recent years (see, e.g., [40–44]). To this end, implementation of the state-of-the-art ‘tricks’ for boosting the calculation of PES in numerical TDSE solvers is an important objective.

### 1.3.3 EVALUATING PES WITH tSURFF IN QPROP 2.0 AND NEWER

Before passing to the discussion of the features of QPROP 3.0 and newer developments, which was an essential part of the work presented in this thesis, it is worth starting with a brief description of the capabilities of the previous version of the program package. The package QPROP was initially introduced in [45]. Back then, the calculation of the PES was implemented by the so-called window-operator method (WOM) [46]. Although WOM is capable of giving the correct total electron spectrum, the treatment of momentum- or angle-resolved PES is only approximate [47, 48]. Besides that, the biggest disadvantage of this method is the requirement to store the whole wavefunction by the end of the laser pulse, which becomes especially tough for long laser pulses. Ten years later, the release of a newer version 2.0 containing an important upgrade was introduced [49]. There, the time-dependent surface-flux method (tSURFF) for calculating the PES was implemented. This method, originally proposed in [50], bases on the representation of the photoionization amplitude in the form of a flux through a surface located sufficiently far away from the atom. This is achieved by taking the photoionization amplitude (5) at time  $T$  (sufficiently longer than the duration  $T_p$  of the ionizing laser pulse) and subtracting the contribution from the volume confined by a sphere of radius  $R$ :

$$a_{\mathbf{k}}(T) \approx \langle \mathbf{k}(T) | \Theta(r - R) | \psi(T) \rangle. \quad (50)$$

Here,  $\Theta(r)$  is the Heaviside function. The value of  $R$  must be chosen large enough for the bound states of the binding potential to be negligible beyond it. Next, the expression (50) is rewritten in the form of a time integral

$$a_{\mathbf{k}}(T) = \int_0^T dt \partial_t \langle \mathbf{k}(t) | \Theta(r - R) | \psi(t) \rangle + \langle \mathbf{k}(0) | \Theta(r - R) | \psi(0) \rangle. \quad (51)$$

As the initial wavefunction contains bound states contributions exclusively, the second term in (51) is eliminated by a proper choice of  $R$ . The time derivative can be expressed as the application of the Hamiltonian according to the TDSE (2) for  $|\psi(t)\rangle$  and the conjugated TDSE  $-i\partial_t \langle \mathbf{k}(t) | = \hat{H}_V \langle \mathbf{k}(t) |$  for  $\langle \mathbf{k}(t) |$ . Importantly, in QPROP with tSURFF, the binding potentials need to vanish beyond  $r = R$ , which allows the continuum to be represented in terms of Volkov states (8). The Hamiltonian for those reads  $\hat{H}_V = -\Delta/2 - i\mathbf{A}(t) \cdot \nabla$  (the purely time-dependent  $A^2(t)/2$  term is removed in QPROP by a gauge transformation), and in the region  $r > R$  the two Hamiltonians coincide, eventually giving

$$a_{\mathbf{k}}(T) = i \int_0^T dt \langle \mathbf{k}(t) | \left[ \hat{H}, \Theta(r - R) \right] | \psi(t) \rangle. \quad (52)$$

As the commutator in (52) vanishes everywhere except at the surface  $r = R$ , the spatial integration boils down to the integral over the surface,

$$a_{\mathbf{k}}(T) = \int_0^T dt \left( \int_{S_R} d\mathbf{S}_{\mathbf{r}} \mathbf{j}_{\mathbf{k}}(\mathbf{r}, t) \right), \quad (53)$$

with the normal vector on the surface  $d\mathbf{S}_{\mathbf{r}} = dS \mathbf{n}_{\mathbf{r}}$  and with the flux density in the integrand being

$$\mathbf{j}_{\mathbf{k}}(\mathbf{r}, t) = \frac{i}{2} \langle \mathbf{k}(t) | \nabla + i\mathbf{A}(t) | \mathbf{r} \rangle \langle \mathbf{r} | \psi(t) \rangle - \frac{i}{2} \langle \mathbf{k}(t) | \mathbf{r} \rangle \langle \mathbf{r} | \nabla + i\mathbf{A}(t) | \psi(t) \rangle. \quad (54)$$

Accumulating the flux in (53) during a finite time interval  $T$  longer than the pulse duration  $T_p$  allows to record the contribution of photoelectrons with momenta  $k$  that are big enough to reach the capturing surface, i.e.,

$$T \geq T_p + \frac{R}{k_{\min}}. \quad (55)$$

#### 1.3.4 EVALUATING THE PES WITH iSURFV IN QPROP 3.0 AND NEWER

Part of the results demonstrated below are presented in publication [51] or are based on those.

Although tSURFF no longer requires to store the whole wavefunction by the end of the laser pulse  $t = T_p$ , which would occupy a volume that scales non-linearly with  $T_p$ , the drawback of this approach is the necessity of a relatively long propagation of the wavefunction even after the laser pulse is over if the slow photoelectrons are of interest (up to times defined by Eq. (55)). A method to overcome this disadvantage was introduced independently in [52] and [53] and was called infinite-time surface-flux method with Volkov functions (iSURFV) in [53]. Here, the key feature is that the laser-free propagation is dictated by a time-independent Hamiltonian. This allows to calculate the contribution from the infinite time interval after the laser pulse in one step. To do so, let us split the integral over time into parts before and after the end of the laser pulse:

$$a_{\mathbf{k}}(T) = a_{\mathbf{k}}(T_p) + \delta a_{\mathbf{k}}^{(T)}(T_p), \quad (56)$$

$$\delta a_{\mathbf{k}}^{(T)}(T_p) = i \int_{T_p}^T dt \langle \mathbf{k}(t) | \left[ -\frac{\Delta}{2}, \Theta(r - R) \right] | \psi(t) \rangle. \quad (57)$$

The first term,  $a_{\mathbf{k}}(T_p)$ , is treated in QPROP numerically as it was described in [49] while the second, field-free term  $\delta a_{\mathbf{k}}^{(T)}(T_p)$  can be calculated without an expensive post-propagation of the wavefunction after the laser pulse is turned off. In a nutshell, the simplification of the expression for  $\delta a_{\mathbf{k}}^{(\infty)}(T_p)$  is performed as follows. As the laser-free conjugated Volkov function  $\langle \mathbf{k}(t) |$  is now just a plane wave, its time-dependent part reads  $e^{ik^2(t-T_p)/2}$ . One may move this factor through the commutator and then formally evaluate the time integral. This is done by expressing  $|\psi(t)\rangle$  at time  $t$  through the action of the evolution operator on

its value at  $T_p$ :

$$|\psi(t > T_p)\rangle = e^{-i\hat{H}_0(t-T_p)}|\psi(T_p)\rangle. \quad (58)$$

Here,  $\hat{H}_0$  is the Hamiltonian without the laser field. The contribution from the upper time boundary to the integral (56) is eliminated in the limit  $T \rightarrow \infty$  by assuming an infinitesimally small imaginary part added to the Hamiltonian. This is fulfilled within the implementation of iSURFV in QPROP thanks to the presence of the complex absorbing potential (46) near the boundary of the numerical grid. As a result, the iSURFV-related contribution to the photoionization amplitude can then be compactly written as [51–53]

$$\delta a_{\mathbf{k}}^{(\infty)}(T_p) = \int_{S_R} d\mathbf{S}_{\mathbf{r}} \mathbf{J}_{\mathbf{k}}^{(\infty)}(\mathbf{r}, T_p) \quad (59)$$

where the time-integrated flux density reads

$$\mathbf{J}_{\mathbf{k}}^{(\infty)}(\mathbf{r}, T_p) = \frac{i}{2} \langle \mathbf{k}(T_p) | \nabla | \mathbf{r} \rangle \langle \mathbf{r} | \frac{1}{E_k - \hat{H}_0} | \psi(T_p) \rangle - \frac{i}{2} \langle \mathbf{k}(T_p) | \mathbf{r} \rangle \langle \mathbf{r} | \nabla \frac{1}{E_k - \hat{H}_0} | \psi(T_p) \rangle. \quad (60)$$

The implementation of the iSURFV method is the core advantage of QPROP 3.0 over previous versions. The related work, along with other improvements that came out with the 3.x releases, was an essential part of the work in the present thesis. Details of the implementation of iSURFV in QPROP 3.0 are described in [51]. The applicability of iSURFV as well as its efficiency is addressed by two particular examples shown below that are also included in the QPROP 3.0 distribution accompanied by several other example configurations.

### Example 1

The first demonstration addresses the case of a short pulse, because for those iSURFV gives the biggest boost in terms of computational time compared to tSURFF. Let this pulse be described by the vector potential

$$\mathbf{A}(t) = \frac{E_1}{\omega} \sin^2\left(\frac{\omega t}{2n_c}\right) \cdot \left[ \sin(\omega t) \mathbf{e}_x + \epsilon \cos(\omega t) \mathbf{e}_y \right]. \quad (61)$$

Consider its polarization circular,  $\epsilon = 1$ , intensity equal to  $I = 2 \cdot 10^{14}$  W/cm<sup>2</sup> and wavelength  $\lambda = 400$  nm. Figure 1.3 illustrates the difference between the results obtained with tSURFF and iSURFV. For iSURFV, the real-time propagation is equal to the pulse duration  $T = 2.67$  fs. tSURFF requires a substantially longer propagation: to capture photoelectrons with momenta higher than  $k_{\min} = 0.1$  one needs  $t_{\max} = 26.85$  fs. In Figure 1.3(c), a cut along 250° (and a cut along 70° displayed by negative  $k$  values) additionally reveals a discrepancy on the logarithmic scale in the high-energy region being close to the numerical noise level. This, however, could be improved by increasing the values of the flux-capturing radius  $R$  and width  $W_{\text{im}}$  of the complex absorbing potential area. In the low-energy part of the iSURFV spectrum, a sharp ring-shaped peak is observed, which, in fact, is not related specifically to iSURFV and would appear in tSURFF provided a longer laser-free post-propagation is conducted. The origin of this peak is the truncation of the binding potential  $U(r \geq R) = 0$ , which is a requirement for using Volkov functions to

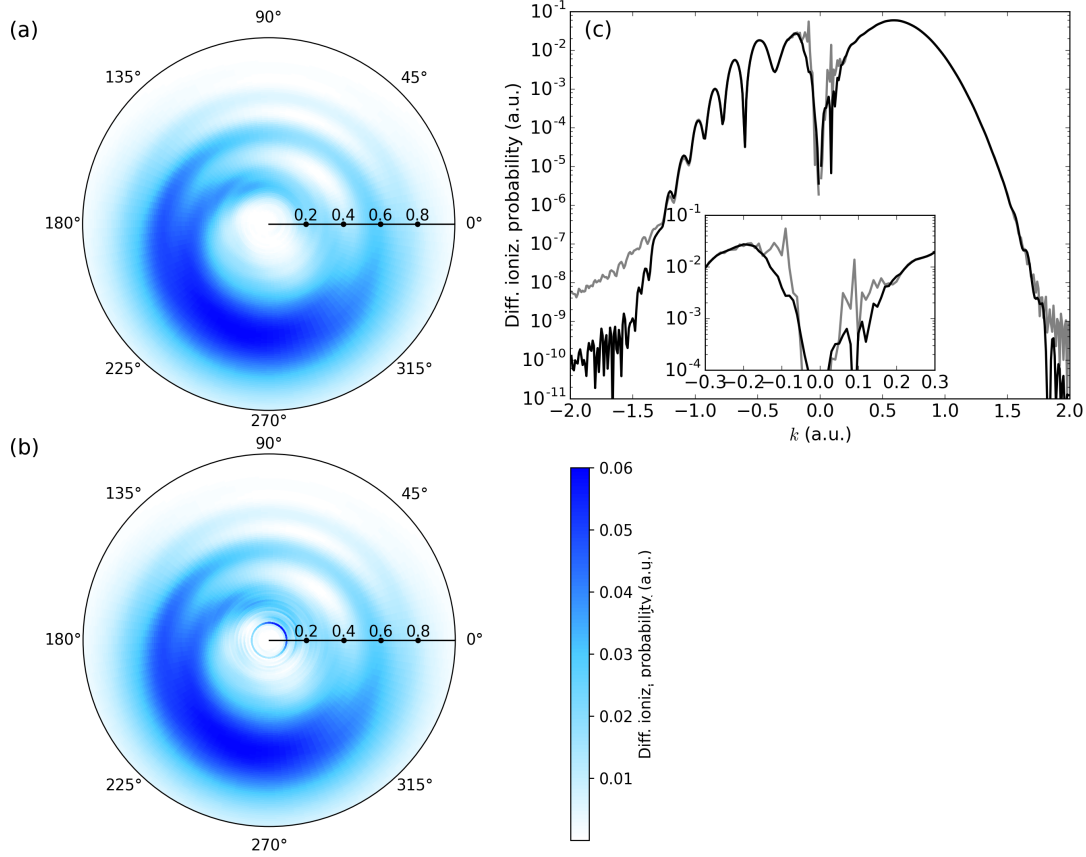


**Figure 1.3: PES for hydrogen in a circularly polarized laser pulse calculated using QPROP 3.2** (a) with tSURFF and (b) with iSURFV. Laser parameters:  $\lambda = 400$  nm,  $I = 2 \cdot 10^{14}$  W/cm<sup>2</sup>,  $n_c = 2$  cycles with  $\sin^2$  envelope. Horizontal axis indicates radial momenta in a.u. The black and gray spectra in (c) are sections through 250° (positive  $k$ ) and 70° (negative  $k$ ) lines from (a) and (b), respectively.

describe the continuum. This structure can be shifted to even lower momenta by choosing a smoother potential in the intermediate domain (in QPROP, the potential is by default matched to a linear roll-off at  $R_{co} = 50$  that reaches zero at  $2R_{co}$ ) or extending this domain (i.e., increasing  $R_{co}$ ).

### Example 2

Analysing Fig. 1.3(b) further, additionally to the brightest artificial sharp peak, a nonphysical oscillatory behavior can be seen in the radial direction at low energies. This effect was also observed in [53] and, in fact, is not caused by the iSURFV trick itself but by the complex absorbing potential. Increasing its width  $W_{im}$  for the evaluation of Eq. (59) reduces the magnitudes of those rings and shifts them to lower momenta. This is illustrated in Fig. 1.4 by another example. There, the same laser pulse but with linear polarization ( $\epsilon = 0$  in (61)) is used and the PES are calculated with iSURFV and with tSURFF with a much smaller  $k_{min} = 0.001$  taken in (55). Interestingly, the only surviving peak is the one located around  $k \approx 0.1$ , which, as mentioned above, is caused by the truncation of the potential. The oscillations related to the complex absorbing potential are successfully pushed to 10 times smaller momenta. Thus, implementation of iSURFV

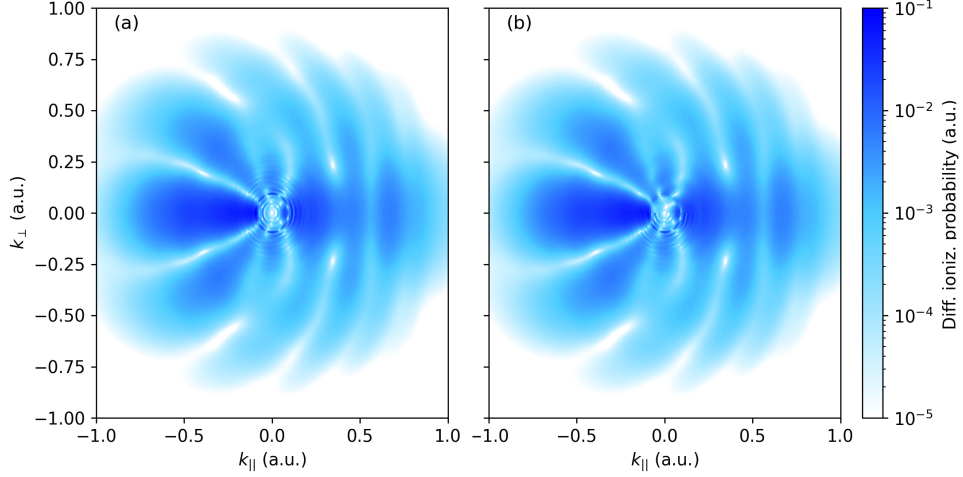


**Figure 1.4: PES for hydrogen in a linearly polarized laser pulse calculated using QPROP 3.2** (a) using tSURFF with  $k_{\min} = 0.001$  (upper halfplane) and i-SURFV (lower halfplane) at  $W_{\text{im}} = 150$  fixed for both. In (b), i-SURFV is used with  $W_{\text{im}} = 1500$  (upper halfplane) and  $W_{\text{im}} = 150$  (lower halfplane). Laser parameters:  $\lambda = 400$  nm,  $I = 10^{14}$  W/cm<sup>2</sup>,  $n_c = 2$  cycles with  $\sin^2$  envelope.

in QPROP not only speeds up the calculations, but also avoids unphysical patterns in PES for slow electrons using tSURFF.

In principle, one could change the shape of the imaginary potential rather than changing its width in order to suppress reflections and transitions (see, e.g., [54]) causing artifacts. However, no universal absorbing potential to cover the infinite energy range exists. Alternatively, instead of an explicit complex-valued term in the Hamiltonian one might adapt the so-called complex scaling in the region where absorption is required [34, 35]. This method is not yet included in QPROP, though.

### 1.3.5 APPLICATIONS OF QPROP 3.0 AND NEWER

Since the implementation of iSURFV in QPROP in [51], the 3.x versions of the program package aided multiple theoretical studies in providing the benchmark for alternative approaches to calculation of PES based on the SFA or the R-matrix with time dependence [55–57]. Moreover, it has been used to reproduce various experimental observations [58–60] with good agreement found in each case. The new capabilities of QPROP 3.x were also utilized in the theoretical investigations presented in Chapter 4 of this thesis.

## CHAPTER 2

# PHASE-OF-THE-PHASE SPECTROSCOPY AND ITS APPLICATIONS

### 2.1 PHASE-OF-THE-PHASE SPECTROSCOPY

Momentum-resolved PES carry information about the properties of the potential of the ionized parent target imprinted in these PES in form of holographic patterns [12–14, 16–19, 61]. Also, with properties of the ionizing laser properly adjusted, electrons can serve as a probe, imprinting in the PES ultrafast processes occurring in the parent atomic or molecular ion at femtosecond timescale [62–64]. Registration of individual incidents in strong-field experiments is, however, not possible to resolve in time. Instead, modern techniques aim on engineering the ionizing laser pulse properties to enhance the ionization in the vicinity of certain times, creating a so-called ‘temporal gate’ for the ionization process. In particular, two-color fields consisting of components with frequencies  $a\omega$  and  $b\omega$  (with  $a, b$  being co-prime) shifted by a phase delay  $\phi$  are promising in that respect. Typically, one component (say,  $b\omega$ ) has a relatively smaller intensity. Such type of streaking enhances the ionization probability in the vicinity of certain  $\phi$ -dependent times while leaving the dynamics of the produced photoelectrons nearly untouched. The simplest setup to realize experimentally and also the simplest to be analyzed theoretically is  $\omega$ - $2\omega$ . If the components are polarized co-linearly, the streaking  $2\omega$  component enhances the main  $\omega$  field around its peak once per laser cycle<sup>5</sup>. The PES  $Y(\mathbf{k}, \phi)$  inherits the periodicity of the ionizing laser field as a function of  $\phi$ . This allows to express the former in the Fourier series:

$$\begin{aligned} Y(\mathbf{k}, \phi) &= Y_0(\mathbf{k}) + \sum_{n \geq 1} |Y_n(\mathbf{k})| \exp[in\phi + i\Phi_n(\mathbf{k})] + \text{c.c.} \\ &= Y_0(\mathbf{k}) + 2 \sum_{n \geq 1} |Y_n(\mathbf{k})| \cos[n\phi + \Phi_n(\mathbf{k})] \end{aligned} \quad (62)$$

Restricting the ratio between the streaking and ionizing fields  $2\xi = E_2/E_1$  to small values ensures that this series converges fast.

The PoP technique has been originally introduced in [67] where the laser field was co-linear two-color  $\omega$ - $2\omega$ , and PoP was used to identify the regions in PES where different ionization pathways dominate. The physical mechanism behind it is easily understood from the classical-trajectory theory as follows. A weak  $2\omega$  field enhances the ionization probability in the vicinity of a certain time instant in an optical cycle of the main  $\omega$  field. This instant is controlled through the relative phase delay  $\phi$  between the components of

---

<sup>5</sup> In comparison, a  $n\omega$  streaking field could enhance the  $\omega$  field around its peak up to  $n - 1$  times per laser cycle. Another different technique bases on the application of a short extreme ultraviolet (XUV) pulse as a streaking field (for review see, e.g., [65] and references therein) which moderates the yield around a single instant in time, thus, not being equal to the  $\omega$ - $n\omega$  case with  $n \rightarrow \infty$ .

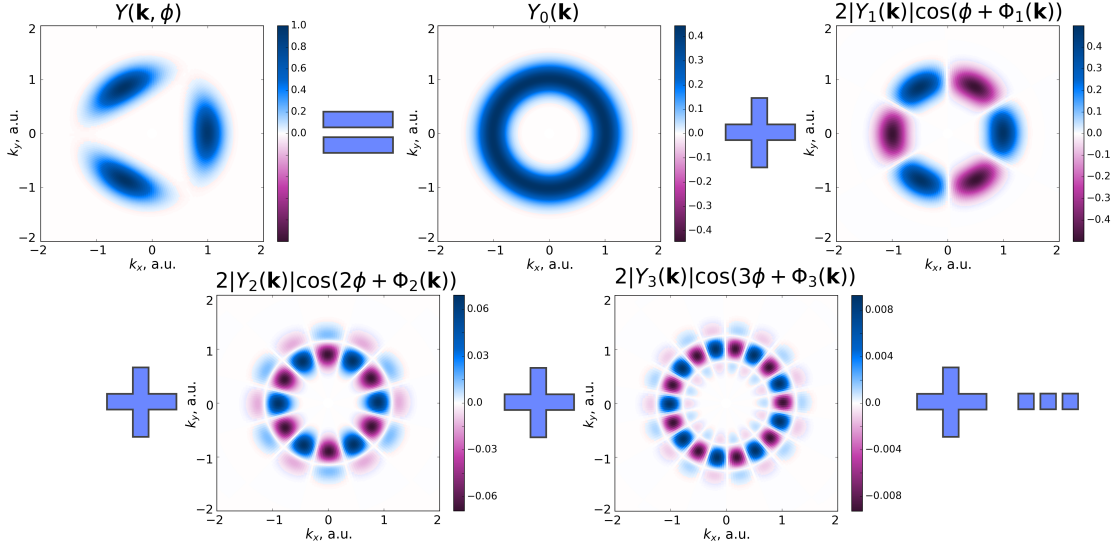


**Figure 2.1: Fourier decomposition (62) of the full PES with respect to the phase  $\phi$  between the two laser components.** Calculation performed within the SFA according to (24) with intercycle interference excluded. The laser field is defined by Eq.(12) with  $a = 1$ ,  $b = 2$ ; intensity and wavelength of the main component  $I_1 = 2 \cdot 10^{14}$  W/cm<sup>2</sup>,  $\lambda_1 = 800$  nm;  $\xi = 0.05$ ,  $\phi = 0$ ; ionization potential  $I_p = 15.8$  eV (argon). Reprinted from [66] with permission. © 2020 by IOP Publishing. All rights reserved.

the laser field, and depends on the final momentum  $\mathbf{k}$  of the photoelectron. The values of the  $\mathbf{k}$ -dependent function  $\Phi_1(\mathbf{k})$  can be, therefore, mapped to ionization times. Due to the symmetry of the main  $\omega$  field, momenta  $\mathbf{k}_{1,2}$  of photoelectrons with opposite signs of the component along the laser field ( $\mathbf{k}_{\parallel,1} = -\mathbf{k}_{\parallel,2}$ ) escape the parent ion at times that differ by  $\omega\Delta t_i = \pi$ . Their contributions are most of all amplified for two-color phase shifts  $\phi_{1,2}$  different by  $\pi$  as well. In turn, this leads to a difference by  $\pi$  in  $\Phi_1(\mathbf{k})$  values for these  $\mathbf{k}_{1,2}$  (see Fig. 2.2 (a)). Electrons that do not simply escape the parent ion and go straight to the detector but undergo rescattering on the parent ion, may eventually end up with the opposite sign of  $\mathbf{k}_{\parallel}$ . Consequently, their contribution to the PES is the highest at shifted values of  $\phi$  compared to ‘direct’ electrons. Thus, in the PoP  $\Phi_1(\mathbf{k})$  the transition between the ‘direct’-dominated and the rescattered-dominated parts of the momentum distribution is indicated by a jump in  $\Phi_1$ . Besides identifying regions of direct and rescattered electrons in PES, additional applications of the PoP will be shown below.

After the first publication [67] devoted to identification of the areas in the PES where different quantum ionization pathways are dominant, the PoP technique was applied in other theoretical and experimental works [68–75]. Its formalism has even been extended to electron-positron pair production from vacuum under an extreme-intense laser field [76]. In the center of this PoP-devoted Chapter 2 is the extension of PoP developed in [66, 77] to analyse PES produced by two-color fields with counter-rotating circular ( $\odot\odot$ ) polarizations. The yield in such a setup inherits from the laser field not just the periodicity in  $\phi$  but also the discrete rotational symmetry, which opens a way for additional applications, as will be shown below.

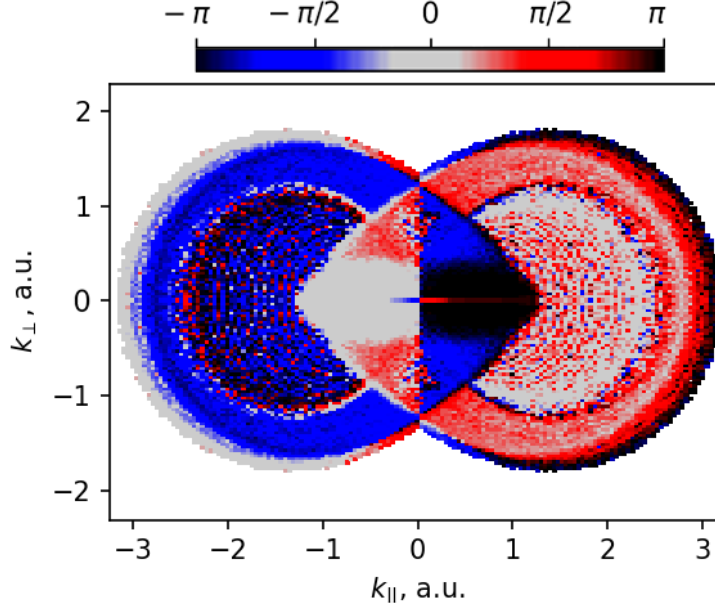


**Figure 2.2:** PoP  $\Phi_1$  for argon in  $\omega - 2\omega$  two-color  $\uparrow\downarrow$  laser field with intensity  $I_1 = 2 \cdot 10^{14} \text{ W/cm}^2$  and wavelength  $\lambda_1 = 800 \text{ nm}$  calculated using CTMC.

## 2.2 CALIBRATING THE INTENSITY OF THE LASER WITH PoP

Part of the results shown below published in [66, 77].

From the technical perspective, the PoP technique is similar to those where the forward-backward asymmetry [78–85] or side streaking [86–90] in the PES is analyzed. The PoP does not explicitly address the PES at selected values of the periodic parameter. The basic idea is instead to study the terms in the Fourier series (62). Perhaps the most clear visual representation of the decomposition (62) is given by PES in circular  $\odot\odot$  fields. For the simplest  $\omega - 2\omega$  case an example is shown in Fig. 2.1.

The main observables of the theory, the terms of the Fourier decomposition of the total spectrum, can be formally evaluated as

$$Y_n(q, \alpha) = \frac{1}{2\pi} \int_0^{2\pi} Y(q, \alpha, \phi) e^{-in\phi} d\phi. \quad (63)$$

The argument of the Fourier component  $\Phi_n(\mathbf{k}) = \arg Y_n(\mathbf{k})$  is the central quantity of interest. It reflects how much does a corresponding component  $Y_n(\mathbf{k})$  lag in phase behind the  $n\phi$  oscillation of the yield and, thus, is called PoP, giving the name to the technique. The magnitude of the Fourier component  $|Y_n(\mathbf{k})|$  is called relative phase contrast (RPC) and reflects the degree of coherence of the measured spectrum to the driver laser phase.

In Section 1.2.4, general formulas for calculating the PES in two-color  $\odot\odot$  polarized laser fields have been derived. There, as was expected from the symmetry of the laser field, the action defining the spectrum was shown to depend on  $\alpha$  and  $\phi$  only through the combination (35):

$$a\theta = a\phi + (a + b)\alpha. \quad (64)$$

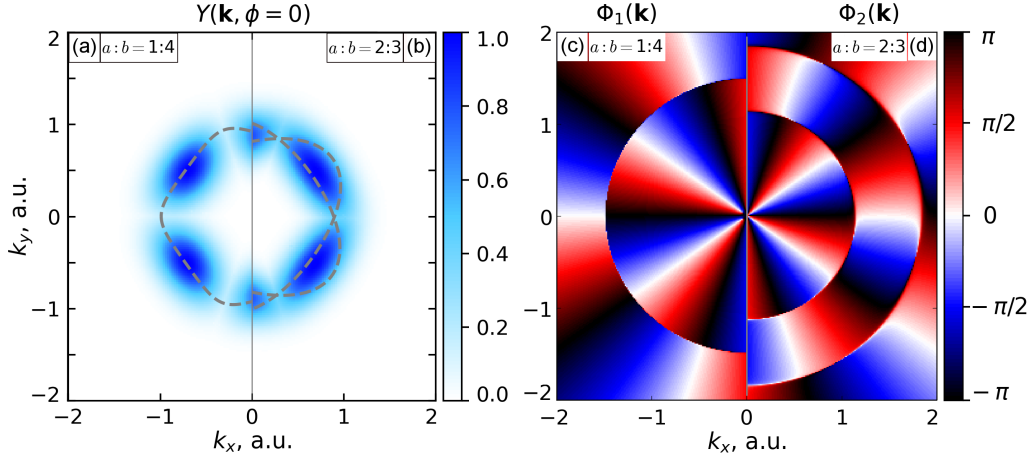


**Figure 2.3: SFA-based PES and PoP  $\Phi_n$  for circular two-color counter-rotating fields** with frequencies  $\omega-4\omega$  (a,c) or  $2\omega-3\omega$  (b,d). Intensity of the first component is  $I = 2 \cdot 10^{14}$  W/cm<sup>2</sup>, its wavelength  $\lambda_1 = 800$  nm,  $\phi = 0$ . (a,b) show the PES, with the negative vector potentials  $-\mathbf{A}(t)$  plotted over them. In (c,d) the correspondent lowest-order PoP are shown:  $\Phi_1(\mathbf{k})$  for the  $\omega-4\omega$  case (c) and  $\Phi_2(\mathbf{k})$  for the  $2\omega-3\omega$  case (d). Adapted from [66] with permission. © 2020 by IOP Publishing. All rights reserved.

The multiplier in front of the angle of emission,  $\alpha$ , in (64) reflects the  $(a+b)$ -fold symmetry of the laser field, leading to the  $(a+b)$  peaks in the PES (see Figs. 2.1 and 2.3 (a)). Another consequence of the  $\theta$ -only dependence is that varying the relative phase delay  $\phi$  will rotate the PES by an angle defined via  $\theta$ , giving thus the following property for the spectrum:

$$Y(q, \alpha, \phi) = Y\left(q, \alpha + \frac{a}{a+b}\phi, 0\right) = Y\left(q, 0, \phi + \frac{a+b}{a}\alpha\right). \quad (65)$$

This property suggests that the dependence on the emission direction angle,  $\alpha$ , can be factored out for each  $Y_n$ , giving simply

$$Y_n(q, \alpha) = Y_n(q, 0)e^{in\frac{a+b}{a}\alpha}. \quad (66)$$

From the periodicity in  $\alpha$  it immediately becomes clear that all harmonics besides multipliers of  $a$  vanish. In Fig. 2.3, two examples with the five-fold symmetry are shown: for the  $a : b = 1 : 4$  case the first non-zero component is  $Y_1(\mathbf{k})$  while for  $a : b = 2 : 3$  it is  $Y_2(\mathbf{k})$ .

One more general property of the Fourier components  $Y_n$  can be derived by analysing the saddle-point equation (36) and the action. Let  $\tau_s(p, \alpha = 0, \phi)$  be a solution to Eq. (36) for a given  $\phi$  at  $\alpha = 0$ . Then it can be shown that  $\tau_s(q, \alpha = 0, -\phi) = 2\pi - \tau_s^*(q, \alpha = 0, \phi)$  is a solution to the same equation but for  $-\phi$ . Substituting these solutions in Eq. (37) for the action and evaluating the resulting imaginary parts gives equal values for both cases:  $\text{Im}S(\phi, t_s(q, \alpha = 0, \phi)) = \text{Im}S(q, -\phi, t_s(\alpha = 0, -\phi))$ . Therefore, for  $\alpha = 0$  (i.e., in  $\mathbf{k} = k\mathbf{e}_x$  direction of emission) the spectrum is symmetric in  $\phi$ . This is justified by examples in

Fig. 2.3. Now Eq. (63) can be conveniently rewritten as

$$Y_n(q, \alpha) = \frac{1}{\pi} \int_0^\pi Y(q, 0, \phi) \cos(n\phi) d\phi e^{in\frac{a+b}{a}\alpha}, \quad (67)$$

and the PoP  $\Phi_n = \arg Y_n$  can be represented as

$$\Phi_n(q, \alpha) = n \frac{a+b}{a} \alpha + \pi \delta_n(q). \quad (68)$$

Here  $\delta_n(q)$  is defined by the sign of the purely real quantity  $Y_n(q, 0)$  and can only be equal to 0 for  $Y_n(q, 0) > 0$  or 1 for  $Y_n(q, 0) < 0$  (without loss of generality). The expression (68) reflects a natural advantage of the PoP technique applied to the case of two-color bicircular counter-rotating laser fields: the only possible type of features in the PoP have circular geometry, centered around  $q = 0$  and represent the flip by a value of  $\pi$ . Thus, the flipping curves for PoP are fully characterized by the correspondent circle radius. By tabulating this radius as a function of some parameter, with all others being fixed, **the PoP technique for two-color  $\odot\odot$  polarized fields may serve as a tool to calibrate the parameters of the laser in focus.**

So far the assumption of weakness of the second component (i.e., of the smallness of  $\xi$ ) has not been used in the derived formulas. The obtained expressions, however, provide only the contribution of ‘direct’ electrons to the total PES. A contribution of those that pass close to the parent ion during their motion in the laser field are neglected. Such electrons would experience rescattering with significant probability. The classical analysis suggests that the current treatment is valid if the vector of the field-driven quiver motion,  $\int^t \mathbf{A}(t') dt'$ , remains safely long at all times  $t$ . This requires the ratio of intensities for the two laser field components,  $I_a/I_b$ , to be far from  $a^4/b^4$  (a justification of this simple argument can be found, e.g., in [91] both by measurements and modeling). The other effect of the Coulomb field of the parent ion is the overall rotation of the PES at an angle defined by the ionized target and the laser parameters [92, 93]. Since the influence of this global rotation will not have any crucial effect on the discussed observables, it will also be neglected further.

Assuming now the weakness of the second component of the field explicitly by considering  $\xi \ll 1$ , the position of the phase flip can be estimated analytically in the case of  $a=1$ , i.e., for 1 :  $b$  frequency ratios (in a more general case,  $a$  different saddle-points would contribute noticeably making the simplistic level of the further analytical treatment insufficient). Expanding then the saddle point in powers of  $\xi$ ,

$$\tau_s = \tau_s^{(0)} + \xi \tau_s^{(1)} + \dots, \quad (69)$$

gives the following expression for the imaginary part of the action (37) with terms up to

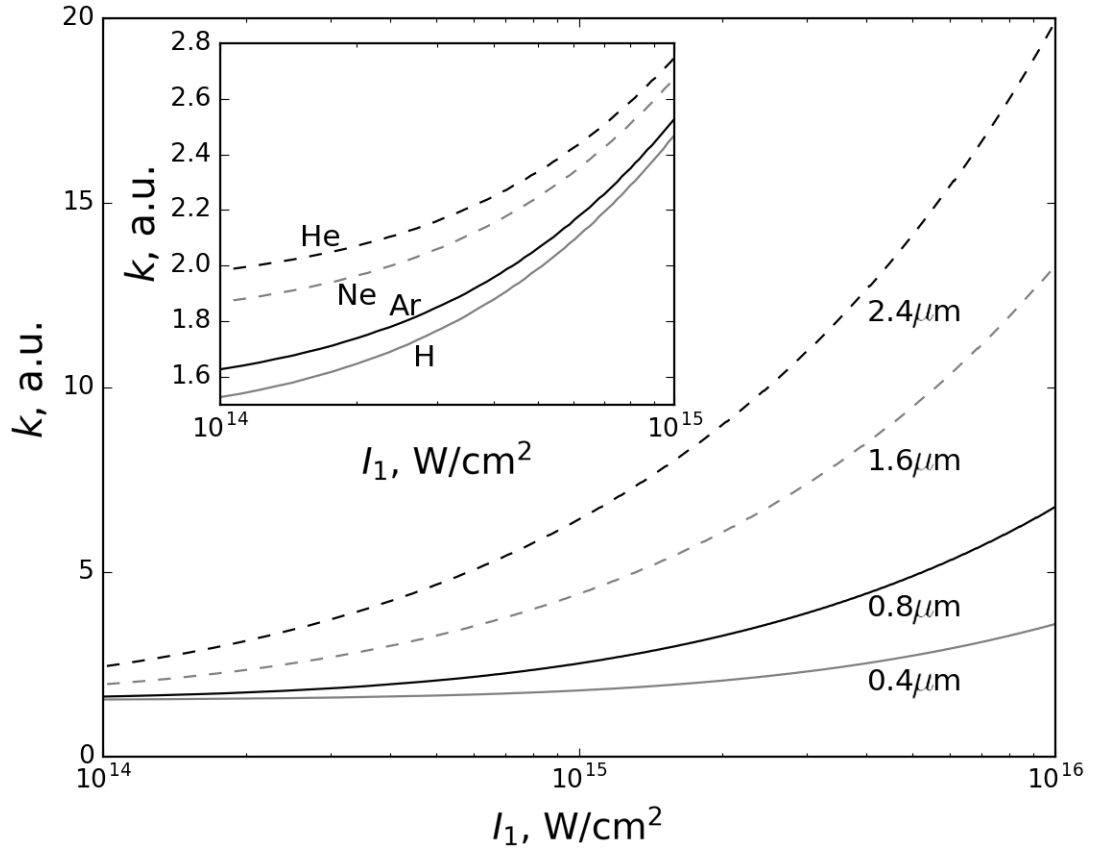


**Figure 2.4: Position of the phase flip of PoP  $\Phi_1$**  as a function of intensity of the main component of the laser field for various wavelengths indicated near each curve. The target chosen is argon and the frequency ratio is  $a : b = 1 : 2$ . Inset: the same function but at fixed wavelength  $\lambda_1 = 800 \text{ nm}$  and various targets being hydrogen, argon, neon and helium is shown. Units in the inset are the same as in the main plot. Adapted from [77].  
 © 2018 by the American Physical Society.

linear in  $\xi$  included:

$$\begin{aligned} \text{Im}S(q, \tau) \simeq \frac{A_0^2}{2\omega} \left\{ \left( 1 + \gamma^2 + q^2 \right) \tau_i^{(0)} - 2q \sinh(\tau_i^{(0)}) \right. \\ \left. + (-1)^b 2\xi \cos \theta \left[ q \frac{1}{b} \sinh(b\tau_i^{(0)}) - \frac{1}{1+b} \sinh((1+b)\tau_i^{(0)}) \right] \right\}. \end{aligned} \quad (70)$$

Here, the imaginary part of the saddle point,  $\tau_i^{(0)}$ , is defined according to (29). Note, that the correction to the saddle point  $\xi\tau_s^{(1)}$  linear in  $\xi$  does not change the action, because the correspondent contributions from the first two terms in (70) eliminate each other. When passing through the zero of the expression in the square brackets,

$$q \sinh(b\tau_i^{(0)}) - \frac{b}{1+b} \sinh((1+b)\tau_i^{(0)}) = 0, \quad (71)$$

the term proportional to  $\cos \theta$  in the Fourier decomposition (62) changes its sign, thus, causing the complex phase  $\Phi_1(q, \alpha)$  to change by a value of  $\pi$  (see Eq. (68)). The upper limit of  $\xi$  where Eq. (71) gives a reasonable analytic prediction is reducing with the increase of  $b$  as other saddle points become less negligible then. Thus, it is best applicable for a configuration with  $a : b = 1 : 2$  frequency ratio: for parameters used in Fig. 2.1 this transcendental equation is satisfied by the radial momentum  $k = 1.86A_0 = 1.76$  a.u., which well agrees with the numerically obtained result (see Fig. 2.9 (a) in the next Section).

One faces here an obvious disadvantage of the application of  $\Phi_1$  for calibration of the laser pulse in the focus. In general, the distribution of photoelectrons produced under a circularly polarized laser field with intensity close or above  $10^{14}$  W/cm<sup>2</sup> from atoms with ionization energy  $I_p/\omega \gg 1$  peaks around radial momentum  $q = 1$ , i.e.,  $p = A_0 = E_0/a\omega$  [8]. In contrast, the flip of  $\Phi_1$  might occur at energies where the ionization probability is low which, in turn, would require long measuring times in order to gain acceptable statistics. Extending the theory to higher-order terms in the series (62) allows to partially bypass this problem. In Fig. 2.5 an example of expansion of the total yield in the Fourier series with several higher components being taken into account is demonstrated. It is seen from Fig. 2.5 that the position of one of the flipping momenta of PoP  $\Phi_2(\mathbf{k}) = \arg Y_2(\mathbf{k})$  can appear closer to the peak of the yield, leading to a significant decrease of the required time needed for a measurement. One should note that achieving the converged behavior for PoP  $\Phi_n$  needs  $n$  times bigger number of phases  $\phi \in [0, 2\pi[$  to be taken into consideration due to its  $n$  times faster oscillation with the variation of  $\phi$  compared to the  $n = 1$  harmonic. This is, however, a minor remark as typically hundreds of phases  $\phi$  are accounted for in the PoP experiments [67, 68, 94] with a scan through a few periods being automated.

Finally, a comment on other existing techniques of in-situ calibration of the laser intensity via measuring PES should be made. For example, in [95, 96] a method based on fitting the whole PES from a short circular laser pulse was proposed. For short linearly polarized carrier-envelope phase (CEP)-stable pulses the function of asymmetry may be used to estimate the peak intensity [83]. Alternatively, fitting with the PPT formula [8, 10] (or with the ADK [9] formula if the tunneling limit of ionization is established) is commonly done provided a scan over different intensities or a scan over the relative phase in a two-color

field is performed. If ionization takes place in the multiphoton regime, intensity can be calibrated by measuring the ponderomotive shift of the ATI peaks (which is proportional to intensity, see Eq. (22)) in PES from water molecules [97, 98]. The PoP-based method proposed in the present thesis may be advantageous. Firstly, the observable it relies on — the radial momentum defining the energy of the PoP flip — is narrowly localized (as were the flips of the PoP in previous experiments [67, 68]). Secondly, taking into account that the variation of the relative phase  $\phi$  only rotates the spectrum and does not deform it, all measurements in the set are performed at constant intensity.

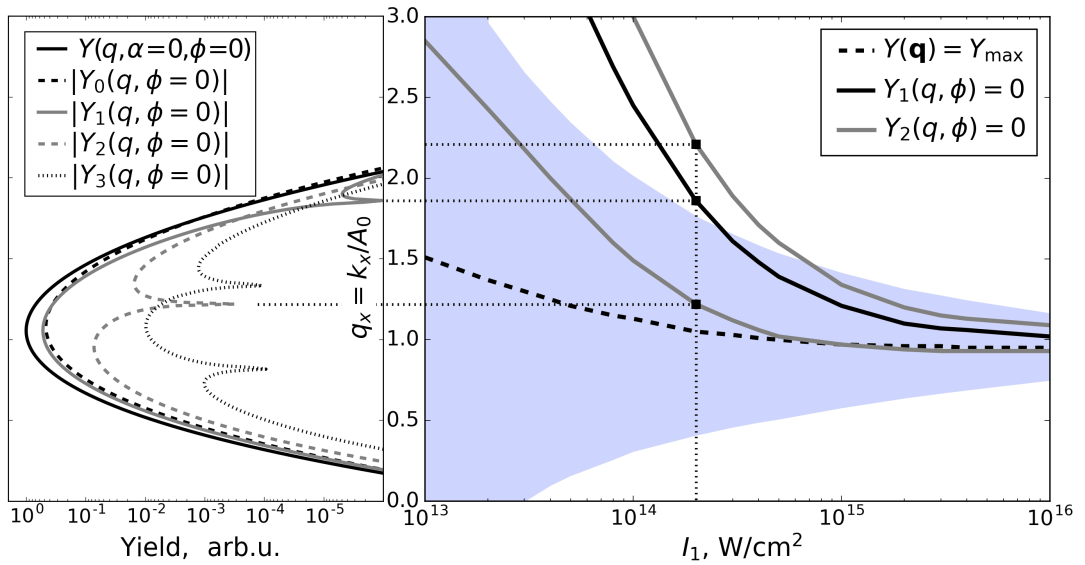


**Figure 2.5:** Left panel: Total spectrum  $Y$  and magnitudes of first few Fourier components  $Y_n$  for  $n = 0-3$  evaluated in the  $q_x = k_x/A_0 > 0$  direction. All parameters are the same as in Fig. 2.1. Sharp minima correspond to momenta where the PoP  $\Phi_n$  flip. Those momenta are labeled with black squares in the right panel. Right panel: Radial momenta of PoP  $\Phi_1$  (black solid line) and  $\Phi_2$  (gray lines) for argon in the two-color  $\omega$ - $2\omega$  laser field with wavelength of the fundamental component  $\lambda_1 = 800$  nm shown as functions of intensity. The region where the spectrum remains above 0.1% of its maximum is denoted by a blue shaded area and the position of this maximum is determined by the dashed black line. Adapted from [66] with permission. © 2020 by IOP Publishing. All rights reserved.

### 2.3 RETRIEVING LASER-COHERENT FEATURES FROM A COMPLEX-TARGET-PRODUCED PES WITH POP TECHNIQUE

Part of the results demonstrated in this Subsection are presented in [66] or are based on those. The work in [66] was done in collaboration with members of the experimental research group ‘Clusters and Nanostructures’ of the University of Rostock who participated in estimating simulation parameters that would be favorable for possible future experiments. The correspondent theoretical modelling was performed by the author of the present thesis.

This Section is devoted to another application of the PoP technique. Spectra of photoelectrons produced during strong-laser-matter interaction contain information about the irradiated target, the laser field and the mechanisms of the intermediate ultrafast phenomena occurring during the ionization process. However, if a target of complex structure is considered, the scattering of the produced photoelectrons in the target might distort or even destroy the correlation between the registered signal and the phase of the ionizing laser field. This complicates the observation of such phenomena as their fingerprints in PES, e.g., high-energy plateaus of the distributions, low-energy structures, ATI-peak patterns and other are smeared out. The PoP technique serves then as a filter with respect to laser-incoherent processes that deform the photoelectron spectra, as will be demonstrated below.

Consider a specific setup where ionization happens from a helium nanodroplet consisting of a few thousand helium atoms as an example of a complex target [99, 100]. Helium nanodroplets are effectively applied as finite-sized spectroscopic matrices for the particles or complexes enclosed in them (dopings) [101–106]. Firstly, thanks to an almost zero temperature inside such a droplet, the influence of rotational and vibrational modes is negligible. Secondly, due to interaction between the doping and the inertial helium surrounding being weak, and, in addition, to optical transparency of helium up to energies about 20 eV, the study of an almost unperturbed species can be conducted in experiments with ultraviolet (UV) or infrared (IR) external radiation regimes. The doping candidates can range from atoms [107] to large atomic clusters [108–111] and complicated biomolecules [107, 112, 113]. In the present thesis, single argon atoms are further considered as dopings. These are known to be of ‘heliophilic’ nature, i.e., after being captured, they move to the center of the droplet and stay localized there [101, 114]. Theoretical investigations of laser-induced electron dynamics in helium droplets with ‘heliophobic’ atomic species (see, e.g. [115–120] and references therein) remain out of scope of this thesis.

The photoelectrons produced initially from the immersed impurity species may experience scattering on helium atoms before they leave the droplet. The resulting recorded PES would then contain a notable contribution of such electrons that already have lost their coherence with the laser during multiple elastic scattering processes. The signal from such laser-incoherent electrons may cover the patterns intrinsic to the weaker signal remaining from unscattered electrons. Therefore, in the experiments with helium droplets, typically the energy distributions and not the angular-resolved PES have been of main interest until

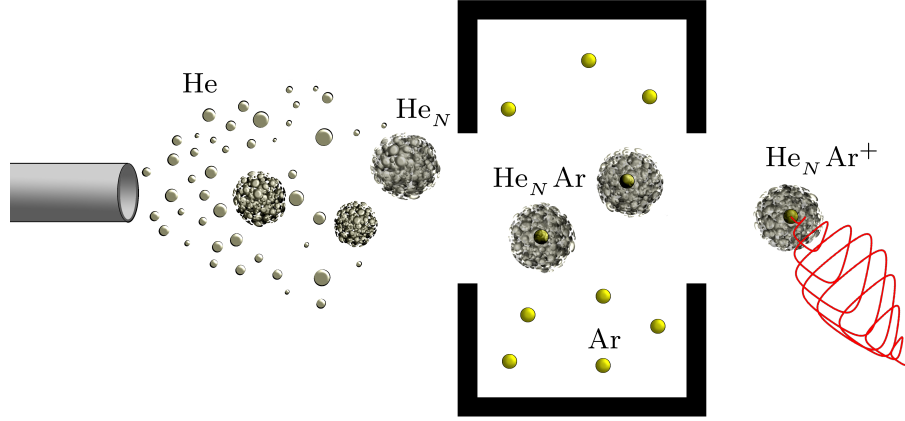


**Figure 2.6: Sketch of the setup used in the calculations.** Each helium droplet of size  $N_{\text{He}}$  captures a single argon atom, which is then ionized by a  $\omega$ - $2\omega$  laser field. Reprinted from [66] with permission. © 2020 by IOP Publishing. All rights reserved.

recent. Here is where the PoP technique advances. Formally, the loss of coherence is equal to a transition of the correspondent yield from higher Fourier components  $Y_n(\mathbf{k})$  in (62) to the lowest,  $Y_0(\mathbf{k})$ . Therefore, a separate study of the terms with  $n > 0$  allows to retrieve the remaining laser-coherent part of the signal dependent on the two-color relative phase  $\phi$ .

A particular setup that the current model will be based on is shown in Fig. 2.6. There, a nanodroplet of few thousands helium atoms passes through the pickup chamber with low-pressure doping gas and collects a single unit of the doping species, which is assumed to have a lower ionization energy than that of helium. After that, this new complex is exposed to an intense laser pulse (of course, not too intense to ionize helium) leading to the ionization of the enclosed particle and leaving the helium surrounding neutral. Technically, a desired mean size of a droplet can be achieved when droplets are created from a gas jet pushed through a narrow nozzle of a given diameter with the backing pressure and the temperature of the nozzle being controlled.

In the follow-up simulation, droplets consisting of  $\overline{N}_{\text{He}} \approx 3 \cdot 10^3$  helium atoms are considered. Such size corresponds to the mean radius  $\overline{R} \approx 3$  nm. This requires 20 bar pressure and 16 K temperature for a nozzle that is  $5\mu\text{m}$  in diameter [121]. Argon atoms are chosen as dopants. One atom per droplet is assumed. The difference between the ionization potential of argon, 15.8 eV, and the one of helium, 24.6 eV, is high enough to neglect the probability of ionization of helium. The ionizing laser pulse is chosen to be two-color with  $\odot\odot$  components of frequencies  $\omega$ - $2\omega$  (i.e.,  $a = 1$ ,  $b = 2$ , and the wavelengths are 800 nm and 400 nm, respectively). The intensity of the main  $\omega$  component is  $I_1 = 2 \cdot 10^{14}$  W/cm<sup>2</sup> while  $I_2 = 2 \cdot 10^{12}$  W/cm<sup>2</sup> ( $\xi = 0.05$ ). The characteristic kinetic energy of the photoelectrons under the chosen laser conditions is  $\langle k^2 \rangle / 2 = 15.4$  eV which is below the ionization or excitation energies of helium. Thus, the scattering is elastic only. Due to the mean distance between the helium atoms being greater than their characteristic sizes, the scattering of an electron is treated in the simplified approximation including a single atom in each event. Taking into account the narrow width of the photoelectron energy

distribution (see Fig. 2.8 (a)), the energy dependence of the scattering cross section can be neglected by taking the total,  $\sigma$ , and differential,  $d\sigma/d\Omega$ , cross sections at fixed  $k^2/2 = 15$  eV. Those values have been taken from [122].

Under the influence of two-color bi-circular laser pulses, the electrons are mainly emitted with momenta close to the  $x$ - $y$  polarization plane (i.e., with negligible  $k_z$ ). Due to the scattering process, they could also end up having their final momenta pointing outside of this plane. What is more important, however, is that such randomly scattered electrons would still contribute to the  $Y_0(\mathbf{k})$  term of the Fourier decomposition (62) only. Other electrons, those that escape unscattered and form  $Y_1$ ,  $Y_2$  and other higher-order terms in (62), should still have momenta located within the vicinity of the polarization plane. Taking this into account, the model in the present example has been restricted to two dimensions (2D), i.e., only the motion in the polarization plane was considered.

The modelling using a MC random walk simulation has been performed in the following way. For the conditions described above, the statistics of a finite number of ionization events  $N_e$  were recorded with initial momenta distributed according to the SFA. Each photoionization event was then followed by the classical laser-free passing through the droplet. The probability of scattering on one of the surrounding atoms of the neutral helium after covering a distance  $s$  was defined as

$$w(s) = 1 - \exp(-n_{\text{He}}\sigma s). \quad (72)$$

Here, the concentration of helium atoms,  $n_{\text{He}}$ , was assumed homogeneous over the volume of a droplet. The values of free paths  $s$  were assigned according to  $s = -(n_{\text{He}}\sigma)^{-1} \log X$

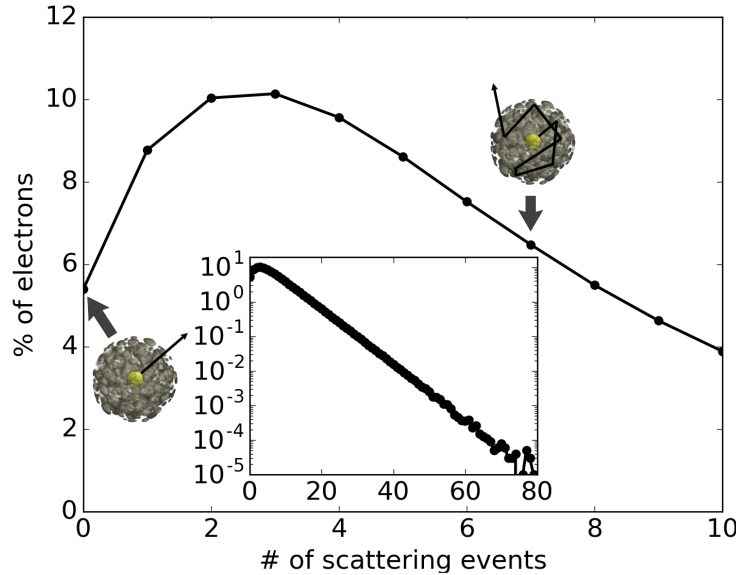


**Figure 2.7: Percentage of electrons that undergo a certain amount of scattering events indicated on the horizontal axis.** The inset demonstrates the same but in the logarithmic scale and for a wider range of scattering events. Droplets consisting of  $N_{\text{He}} = 3 \cdot 10^3$  helium atoms are considered. Laser parameters are as those in Fig. 2.8 Adapted from [66] with permission. © 2020 by IOP Publishing. All rights reserved.

where  $X$  was randomly chosen with a uniform distribution between 0 and 1. If  $s$  is smaller than the current distance to the border of the droplet, the scattering occurs. The scattering angle,  $\vartheta$ , was then chosen randomly from  $-\pi$  to  $\pi$  according to  $d\sigma/d\Omega$ <sup>6</sup>. No restriction for the total number of scattering events was assumed.

In the present example, the probability of multiple elastic scattering on the neutral helium surrounding atoms is relatively high, as demonstrated in Fig. 2.7 showing the percentage of the electrons as a function of scattering events count. Here, only about 6% of the initial number of electrons remained unscattered. An example of the initial distribution calculated according to the SFA is shown in Fig. 2.8 (a). Including here the contribution of the process of scattering on neutral atoms of the helium droplet significantly deforms the distribution (see Fig. 2.8 (b)). The three-fold-symmetric part of the spectrum is now suppressed by the nearly isotropic contribution from the laser-incoherent photoelectrons. After performing similar calculations for  $N_\phi = 20$  different phases  $\phi \in [0, 2\pi[$  (i.e., for 10 values per one period of  $Y_2 e^{i2\phi}$ ), the PoP can be applied, and the position of the phase flips can be determined. The results are presented in Fig. 2.9. Due to low ionization probability at high energies, the flipping of the PoP  $\Phi_1$  (located at  $k = 1.76$  a.u.) remains visible in the absence of scattering only (see Figs. 2.9 (a) and (b)), even after taking a higher number of initial ionization events ( $N_e \geq 2 \cdot 10^8$  for a grid with momentum resolution of  $dk = 0.02$ ). However, instead of increasing the number of photoelectrons (that is formally equivalent to increasing the time of measurement in an experiment) one may address PoP  $\Phi_2$ . As suggested by Fig. 2.5, this requires considerably lower statistics (cf. Figs. 2.9 (c) and (d)) and renders the phase flipping curve observable even when the highest part of the signal comes from the scattered electrons (see Fig. 2.9 (e)). To wind up, **the PoP technique allows to subtract the laser-incoherent part from the total spectrum even if this incoherent contribution is dominant. Application of the PoP technique with respect to higher-order terms of the Fourier decomposition, e.g.,  $\Phi_2$ , may be beneficial in terms of required measurement time compared  $\Phi_1$ .**

---

<sup>6</sup> Positive  $\vartheta$  indicate clockwise rotations in the 2D plane, negative  $\vartheta$  indicate the opposite.

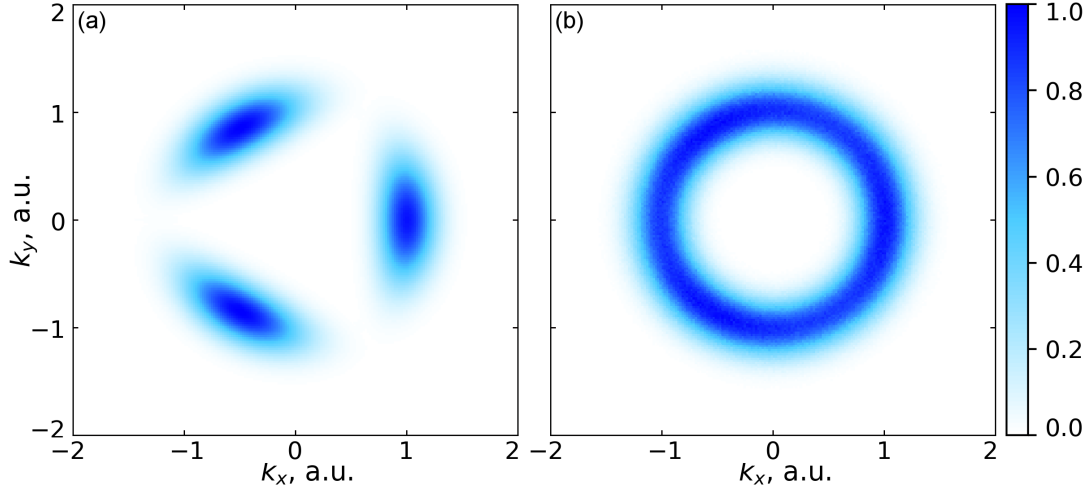


**Figure 2.8:** (a) PES predicted by the SFA for a two-color bicircular laser field with counter-rotating components of frequencies  $\omega$  and  $2\omega$ , interacting with an argon atom. (b) Same but for an argon atom placed in a helium droplet. Droplets consisting of  $N_{\text{He}} = 3 \cdot 10^3$  helium atoms are considered, which leads to blurring of the angular distribution of photoelectrons due to their elastic scattering on neutral atoms of the droplet. Laser parameters: the main component has intensity  $I_1 = 2 \cdot 10^{14}$  W/cm<sup>2</sup> and wavelength  $\lambda_1 = 800$  nm;  $I_2 = 0.01 I_1$  ( $\xi = 0.05$ ),  $\phi = 0$ . The total number of initial ionization events is  $N_e = 2 \cdot 10^7$ . Adapted from [66] with permission. © 2020 by IOP Publishing. All rights reserved.

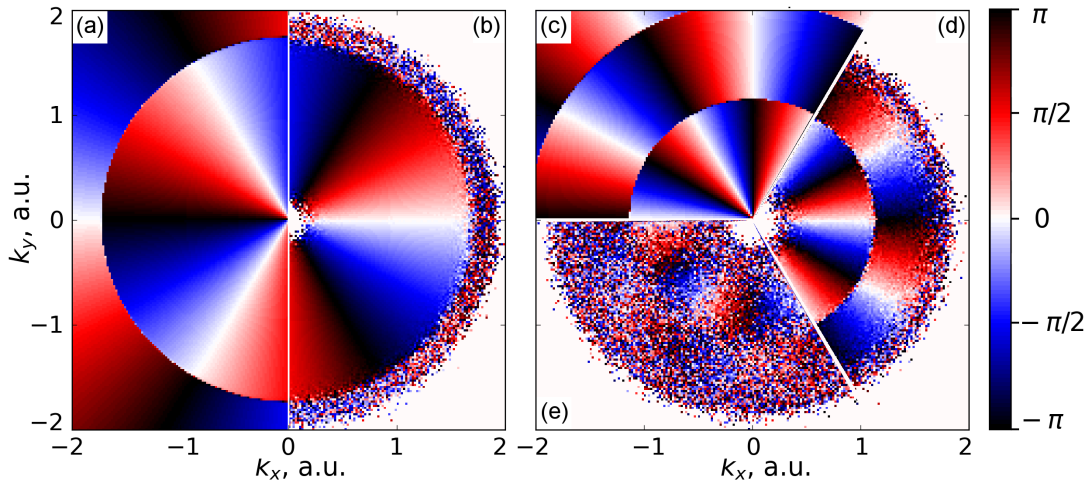


**Figure 2.9:** (a) PoP  $\Phi_1$  from a continuous SFA-based distribution, (b) – the same but for a finite number  $N_e = 2 \cdot 10^8$  of photoelectrons for each phase  $\phi$ . (c) PoP  $\Phi_2$  from a continuous SFA-based distribution, (d) the same but for a finite number  $N_e = 2 \cdot 10^7$  of photoelectrons for each phase  $\phi$ . (e) the same as (d) but with the (multiple) scattering on neutral helium atoms of a surrounding droplet being taken into account. For all cases  $N_\phi = 20$  phases have been taken. Adapted from [66] with permission. © 2020 by IOP Publishing. All rights reserved.

## 2.4 CONCLUSIONS OF CHAPTER 2

- The “Phase-of-the-phase” (POP) technique has been extended to the case of two-color  $\odot\odot$  laser fields having frequencies  $a\omega$ - $b\omega$  with  $a, b$  being coprime. Basic properties have been derived. The main observables, PoP  $\Phi_n$ , are shown to experience sharp flips by  $\pi$  at certain photoelectron energies. The positions of the PoP flips are well-localized in energy and are sensitive to the laser parameters as well as the ionized target. Based on that fact, a method of calibrating the intensity of the laser field in focus using PoP spectroscopy with bi-circular  $\odot\odot$   $a\omega$ - $b\omega$  laser fields has been introduced.
- A way to subtract the laser-incoherent part from the total PES with the help of the PoP technique has been proposed. For demonstration purposes, a MC-based model describing the ionization of argon atoms inside helium nanodroplets has been introduced. The angular structure in the PES from doped helium droplets is masked by a dominant laser-incoherent contribution from electrons that experience multiple collisions on the surrounding helium atoms. The application of the PoP technique to the analysis of such PES reveals the remaining weak laser-coherent part in the total signal.

It is worth mentioning that subtracting the contribution of the electrons generated by laser-incoherent processes of other nature, in example, those created due to thermal emission, should also be possible.

## CHAPTER 3

# OPTIMIZING PLASMA-INDUCED THz RADIATION USING INTENSE TWO-COLOR IONIZING LASER FIELDS

### 3.1 TERAHERTZ RADIATION RESULTING FROM THE INTERACTION OF A STRONG LASER PULSE WITH ATOMIC GASES

The previous Chapter was dedicated to the analysis of the PES produced by a strong laser interacting with systems of different complexity. Apart from being used directly for the determination of the parameters of the ionizing laser or of the parent atomic or molecular ion, the PES may provide a link to other physical processes, which are otherwise harder to examine directly. For instance, the principle of the high-harmonic generation (HHG) is based on the recombination of the electrons with their parent ions, which are initially produced from species in a gas or a solid under the influence of an external strong laser field and which then absorb multiple photons from that laser field [123, 124]. The physics behind the PES and the HHG spectrum here mainly differs at the stage of the interaction of the electron with its parent ion leading to scattering instead of recombination. While the properties of HHG spectra rely essentially on the microscopic response of the system in first place, in the current Section a principally different physical process will be addressed — the generation of low-frequency radiation from a laser-induced plasma. In a nutshell, the mechanism is as follows. A strong laser interacts with a gas and transfers energy to electrons generating a plasma cloud. The electrons' motion taking place in that plasma is not guided exclusively by the laser field but can continue even after the pulse is over. This global plasma movement has an oscillatory nature at frequencies that are related to macroscopic properties of the system. The acceleration of the plasma dipole results in the emission of radiation in that frequency domain. With the proper adjustment of the plasma parameters the characteristic frequencies may be orders of magnitude lower than the initial frequency of the ionizing laser [125–130]. For example, applying an IR laser pulse of femtosecond duration to an atomic gas may generate output radiation in the THz frequency domain (100 – 300 times slower) at the picosecond timescale (10 – 100 times longer).

The interaction of a strong laser with a gaseous target is not the only pathway to create a source of coherent THz radiation [131]. For example, exposing specific non-linear crystals to strong laser beams can also result in the desired frequency conversion [132–138]. The first drawback of this alternative is that the bandwidth of the output radiation is usually restricted to a few THz. Additionally, another obvious obstacle on the way to control the generated THz pulse intensity is the upper limit on the intensity of the

initial laser pulse because surpassing the damage threshold value eventually destroys the crystal. Such limitations are absent in the THz sources based on synchrotrons or on free-electron lasers [139–142]. Those are, however, extremely costly devices of incomparably bigger sizes. A lower price and relative simplicity of a THz source based on laser-induced plasma radiation are not the only differences: a free-electron laser provides a relatively long, essentially multicycle THz pulse. This was the case in [143] where it was used to resolve the ionization dynamics of highly excited atomic states and to probe the spatial geometry of the initial Rydberg state. In contrast, a laser-plasma-based scheme may provide a single-cycle or a sub-cycle broadband pulse of THz radiation. Being substantially shorter than the characteristic time of a Rydberg electron’s motion, a half- or single-cycle THz pulse may be advantageous in the investigation of very-low-energy structures in PES [144]. To this end, the laser-gas-based scheme remains a promising candidate for creating a handy source of coherent THz radiation.

In the experiments aiming, for instance, at the usage of HHG, the efficiency of frequency conversion is rather low (being at the level of  $10^{-4}$  [145, 146]). However, the obtained XUV radiation is intense enough for some applications [147–150]. There, the problem of control over the temporal shaping of the generated attosecond pulses deserves more attention than the problem of efficiency improvement. This is, however, not the case for practical applications of plasma-produced THz radiation. While in the setups based on the optical rectification in non-linear crystals the conversion efficiency reaches the level up to a few percent [136, 151, 152], until recently, the commonly applied laser-plasma-based schemes provided roughly an order of magnitude lower yields [153, 154]. This kept the necessity of improvement of the established experimental setups for the generation of laser-plasma-induced THz radiation out of question. The way towards such an improvement can be targeted by the following simple reasoning. As the creation of coherent THz radiation is attributed to the oscillatory motion of the mean dipole of the electron plasma, the amplitude of the emitted radiation is roughly proportional to the amplitude of the dipole acceleration, which in turn scales roughly as the net momentum of photoelectrons that remains after the laser pulse is over. In other words, the ionizing laser pulse should be tailored such that it maximizes the net photoelectron momentum. This can be reached by several means. Firstly, the temporal shaping of the ionizing pulse may create photoelectrons with a preferable direction of emission. This is achieved either by short pulses with CEP optimization or by relatively long pulses consisting of components with different frequencies. As the first case is strongly dependent on the particular shape of the laser pulse envelope and should be studied uniquely in each specific case of experimental implementation, this optimization pathway will not be discussed in the present thesis. For relatively long multi-color pulses, the finiteness of their duration is further assumed to result only in the necessity of an additional parametric scan near the predicted optimizing conditions.

Hereafter, the focus will be on two-color pulses as a simple but effective experimental approach [131]. Considering the simplest case of  $\uparrow\uparrow$  polarizations, the disadvantage of using a monochromatic pulse is apparent as the temporal symmetry,  $|E(t)| = |E(t + \pi/\omega)|$ , of a laser field leads to a symmetric PES,  $Y(\mathbf{k}) = Y(-\mathbf{k})$ , predicting a zero net momentum.

This is no longer the case for two-color fields, as will be discussed in the next Section where optimization of such pulses to maximize the THz output power will be considered.

The next important point to investigate is optimization in terms of polarization of the ionizing laser, again assuming two-color fields. For instance, in the context of the previous Chapter, the two-color fields with  $a\omega$  and  $b\omega$  components both circular and rotating in opposite directions ( $\odot\odot$ ) were introduced. Due to their symmetry properties, they produce PES with average momentum equal zero and, thus, lead to a zero net photoelectron current, which makes them the worst candidate for THz radiation production (in fact, such fields can be specifically implemented in order to decrease the output radiation from plasma emission if it is undesired). Oppositely, application of two-color fields with corotating circular ( $\odot\odot$ ) polarizations can be beneficial and surpass in power the  $\Updownarrow\Updownarrow$  two-color setups.

An apparent enhancement of the total residual photoelectron current is reached if laser pulses of longer wavelengths at fixed intensity are applied. The created THz radiation, thus, would also amplify significantly. This was confirmed in a number of experiments [153, 155, 156] with two-color  $\Updownarrow\Updownarrow$  pulses. In [156] a conversion efficiency surpassing the 1% level has been reported, similar to modern optical rectification schemes. In the present thesis, it is proposed to combine the benefits of the non-linear polarization together with the application of long-wavelength MIR lasers.

Lastly, the proper restriction of the geometrical volume of the laser-irradiated gaseous medium can also improve the THz outcome. Theoretical investigations in that direction remained out of scope of the present thesis but a short review on them is given at the end of the Chapter.

### 3.2 OPTIMIZING THE INTENSITY RATIO IN A TWO-COLOR LASER FIELD WITH COLINEARLY POLARIZED ( $\uparrow\uparrow$ ) COMPONENTS

Part of the results presented in this Subsection are published in [27].

Typically, in the experiments commercial Ti:sapphire lasers are utilized which provide photons with energy  $\omega \approx 1.5$  eV (wavelength  $\lambda = 800$  nm). For a common duration of  $T \approx 100$  fs, such a pulse consists of 40 optical cycles. Therefore one may safely neglect the influence of its temporal shape on the ionization dynamics and approximate the envelope as constant. Consider a two-color laser field whose components are polarized both along the  $x$  axis and have a frequency ratio 1 : 2. As the combined laser field maximizes only once per optical cycle of the slower component with frequency  $\omega$ , the control over the subsequent dynamics via adjustment of the laser field parameters remains rather simple and effective. The expression (12) for the vector potential then simplifies to

$$\mathbf{A}(t) = \mathbf{e}_x \frac{E_1}{\omega} \left( \cos(\omega t) + \xi \cos(2\omega t + \phi) \right) \equiv \mathbf{e}_x A_0 a(\omega t) \quad (73)$$

with  $A_0 = E_1/\omega$  being the characteristic electron momentum in that field. Creation of the  $2\omega$  component ( $\lambda/2 = 400$  nm) can be technically achieved by placing a non-linear beta barium borate (BBO) crystal in the beam path. Using two wedge-shaped crystals allows precise adjustment of the non-linear medium thickness, giving control over the relative intensities of the fields  $4\xi^2$ . The relative magnitude of the  $2\omega$  field may reach  $2\xi = 0.385$  with such scheme, thus providing intensity ratios up to about  $4\xi^2 \sim 0.1$  [131, 157]. A further increase may be reached, for example, by lowering the  $\omega$  component with a suitable filter or by applying other types of non-linear crystals [158]. For consistency, the adjectives ‘first’ and ‘main’ refer hereafter in this Chapter to the  $\omega$ -component of the laser field while ‘second’ refers to the  $2\omega$ -component, regardless of the ratio of their intensities.

The central quantity of interest, the net photoelectron current, can be evaluated as

$$\mathbf{j}(t) = - \int_0^t dt' n_{\text{at}}(t') \int d^3k \mathbf{k} \partial_t Y(\mathbf{k}, t'). \quad (74)$$

Here,  $\partial_t Y(\mathbf{k}, t') dt'$  is the ionization probability within the time interval  $dt'$  for electrons with final momentum  $\mathbf{k}$ , and  $n_{\text{at}}(t')$  is the concentration of atoms that is assumed uniform. The value of the total ionization rate reads

$$w = \int_0^t dt' \int d^3k \partial_t Y(\mathbf{k}, t'). \quad (75)$$

An estimate of the net momentum  $\mathbf{k}_0$  can be given by addressing the expression for the most probable momentum (such that  $Y(\hat{\mathbf{k}}) = \max Y(\mathbf{k})$ ). The follow-up calculations will again be performed in the framework of the SFA and the saddle-point approximation. Then the answer can be given in a closed-form in the case of one laser component being

sufficiently weaker than the other [27]:

$$\hat{k}_x \approx \frac{E_2}{2\omega} \frac{\gamma^3}{\sqrt{1+\gamma^2} \sinh^{-1} \gamma - \gamma} \cos \phi, \quad E_2 \ll E_1. \quad (76)$$

Here,  $\gamma$  is Keldysh parameter (26). The limiting cases of tunneling ( $\gamma \ll 1$ ) and multiphoton ( $\gamma \gg 1$ ) regimes for this expression were introduced in [128, 130]. In summary,

$$\hat{k}_x \approx \frac{E_2}{2\omega} \cdot 3 \cos \phi, \quad \gamma \ll 1, \quad E_2 \ll E_1 \quad (\xi \ll 1); \quad (77)$$

$$\hat{k}_x \approx \frac{E_2}{2\omega} \frac{\gamma^2}{\ln(2\gamma) - 1} \cos \phi, \quad \gamma \gg 1, \quad E_2 \ll E_1 \quad (\xi \ll 1/\gamma). \quad (78)$$

Similarly, if the  $2\omega$  component is dominant, one finds [128, 130]

$$\hat{k}_x \approx \frac{E_1}{\omega} \frac{3}{4} \sin \left( \frac{\pi(n + 1/2) + \phi}{2} \right), \quad \gamma \ll 1, \quad E_2 \gg E_1 \quad (\xi \gg \gamma); \quad (79)$$

$$\hat{k}_x \approx \frac{E_1}{\omega} \sqrt{\frac{\gamma}{2\xi}} \frac{1}{\ln(2\gamma/\xi) - 1} \sin \left( \frac{\pi(n + 1/2) + \phi}{2} \right), \quad \gamma \gg 1, \quad E_2 \gg E_1 \quad (\xi \gg 1/\gamma). \quad (80)$$

The variable  $n$  in (79-80) takes values  $n = 0, 1, 2, 3$  with one of them giving the biggest peak in the spectrum, depending on the phase  $\phi$ . In brackets additional  $\gamma$ -dependent conditions are introduced, delineating the validity of the correspondent expressions according to the strength of the  $2\omega$  field that might start dominating the ionization process even without the condition  $\xi \sim 1$  fulfilled. In Eq. (80) the parameter  $\gamma/\xi$  is the Keldysh parameter for the  $2\omega$  field.

In both of the limiting cases  $E_2 \ll E_1$  and  $E_2 \gg E_1$  the most probable momentum scales linearly with the amplitude of the *weaker* field component. Therefore, conditions optimizing this value and, correspondingly, the net photoelectron current and, finally, the THz output power, should exist. Finding optimal intensities and the relative phase between the fields is the key aspect of this Section.

In principle, for a strictly periodic field as the one defined above in Eq. (73), the momentum distribution consists of delta-peaks, which makes the integration over energy (i.e., over  $d|\mathbf{k}|$ ) in (75) trivial. This ATI-peaks pattern caused by intercycle interference might affect the value of the average momentum but makes a noticeable contribution only in the multiphoton regime. Next, integration over angles  $d\Omega_{\mathbf{k}}$  can be performed approximately by taking into account a fast decrease of the signal with increasing perpendicular momentum  $k_{\perp}$ , and a Gaussian type of that dependence at small  $k_{\perp}$  [10]. The total ionization rate then reads

$$w = 2 \sqrt{\frac{\omega^5}{\sinh^{-1}(\gamma)}} \sum_{n \geq N_{\min}} \mathcal{F} \left( \sqrt{\sinh^{-1}(\gamma) k_n^2 / \omega} \right) \times [|\mathcal{M}(k_x = k_n)|^2 + |\mathcal{M}(k_x = -k_n)|^2]. \quad (81)$$

Here,

$$\mathcal{F}(x) = e^{-x^2} \int_0^x e^{t^2} dt \quad (82)$$

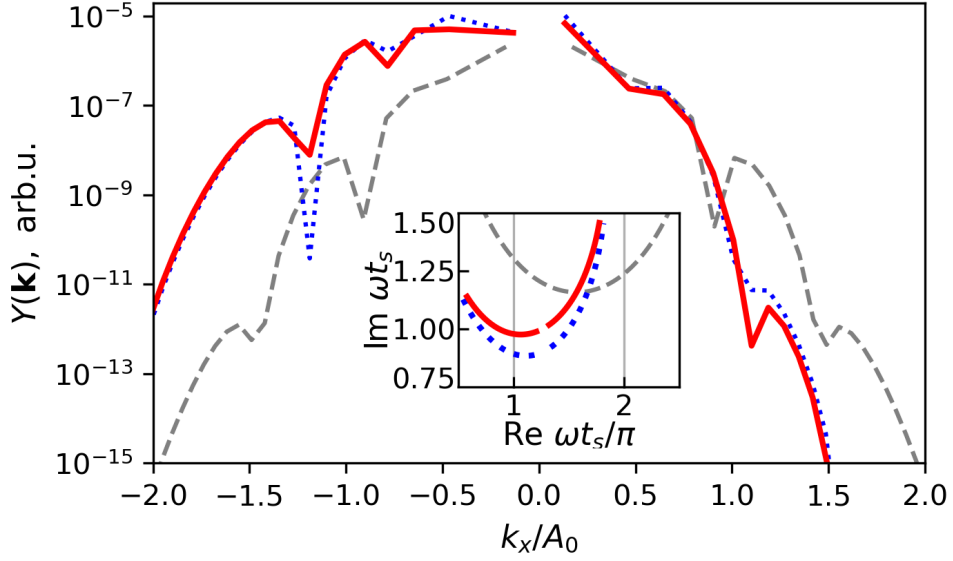


**Figure 3.1: PES for argon in a two-color field with colinear components** as a function of dimensionless momentum  $q_x = k_x/A_0$  with  $q_\perp = 0$  calculated within the SFA with prefactor (87) included. The main component of the  $\uparrow\downarrow$  laser field has intensity  $I_1 = 6.2 \cdot 10^{13} \text{ W/cm}^2$  ( $E_1 = 0.042$ ) and wavelength  $\lambda_1 = 800 \text{ nm}$  ( $\omega = 0.056$ ). The temporal shape is defined according to (73) with  $\xi = 0.15$ . Result obtained with exact solutions to the saddle-point equation (42) is shown with red thick solid lines, result calculated with approximate saddle-points (43-44) – with blue dotted lines. The PES in absence of the  $2\omega$  field ( $\xi = 0$ ) is shown with grey dashed lines. The inset demonstrates the saddle point  $\tau_1$  (see Eq. (43)) in the complex time plane changing with momentum. Line types in the subplot are the same as in the main plot. Adapted from [27]. © 2015 by the American Physical Society.

is the Dawson function [159]. Summation is taken over momenta  $k_n$  defined according to the energy conservation law (22) with the lower limit  $N_{\min}$  restricting  $k_n^2 \geq 0$ . The function  $\mathcal{M}(k_x = k_n)$  represents a contribution to the ionization amplitude from one optical cycle. For laser fields of long but finite duration (such that  $\omega T \gg 2\pi$ ) the expression for the ionization rate can be obtained by replacing the constant amplitudes  $E_{1,2}$  by slow-varying envelopes  $E_{1,2}(t)$  in (73).

For times  $t > \tau_{\text{sat}}$  at which the ionization reaches its saturation, the photoelectron current becomes proportional to the net photoelectron momentum:  $j_x = -n_0 k_0$ . Performing analogous calculations as for function (81) but now with additional weight  $k_x$ , one gets

$$k_0 = \frac{2}{w} \sqrt{\frac{\omega^5}{\sinh^{-1}(\gamma)}} \sum_{n \geq N_{\min}} \mathcal{F}\left(\sqrt{\sinh^{-1}(\gamma) k_n^2 / \omega}\right) \times k_n [|\mathcal{M}(k_x = k_n)|^2 - |\mathcal{M}(k_x = -k_n)|^2] \quad (83)$$

with  $w$  being defined according to (81). Evaluation of the amplitude  $\mathcal{M}$  with exponential accuracy can be performed within the saddle-point method using the results presented in Section 1.2.6.

Figure 3.1 shows the PES along polarization axis. This distribution is strictly symmetric and leads to a zero net photoelectron momentum in the absence of the second

component of the laser field ( $\xi = 0$ ). However, already at  $\xi \sim 0.15$  the left-right symmetry noticeably breaks, also increasing the total ionization probability quite significantly. Comparison of the two calculations, one using the exact solutions to (42) and the other using the approximate formulas (43-44), shows that the latter remain quite precise even at  $\gamma \simeq 1$ .

### 3.2.1 CORRECTIONS TO THE IONIZATION PROBABILITY WITHIN THE SFA FOR $\Updownarrow$ TWO-COLOR FIELDS

While (83) is conserved if  $\mathcal{M}$  is scaled by a constant, the total ionization rate  $w$  defined above in Eq. (81) depends on the global magnitude of  $\mathcal{M}$ . The value  $w$  gives an estimate for the saturation time:

$$\tau_{\text{sat}} \simeq 1/w. \quad (84)$$

The upper limit  $\nu_2$  for the output THz radiation frequency is related to the smaller of the times  $\tau_{\text{sat}}$  and the pulse duration  $T$ , raising the importance of the accuracy in the evaluation of the ionization rate. At this point, the following two types of improvements to the PES must be introduced which were not crucial in the context of Chapter 2 and, thus, were neglected there. Firstly, the prefactor  $P$  in Eq. (24) can no longer be ignored. The evaluation of  $P(\mathbf{k}, t_s)$  is described in detail in [4, 6, 160]. For an electron in an atomic state with a characteristic atomic momentum  $\kappa = \sqrt{2I_p}$ , orbital quantum number  $\ell$  and magnetic number  $m$  the result for the photoionization amplitude has the following form:

$$\mathcal{M}(\mathbf{k}) = \sum_j M_{\mathbf{k}}(t_{s,j}) = \sum_j \mathcal{P}_{\ell m}(\mathbf{k}, t_{s,j}) e^{iS_0(\mathbf{k}, t_{s,j})}. \quad (85)$$

Here, the prefactor reads

$$\mathcal{P}_{\ell m} = C_{\kappa\ell} \sqrt{\frac{\kappa}{S_0''(t_{s,j})}} Y_{\ell m}(\mathbf{n}) \quad (86)$$

where  $Y_{\ell m}$  are spherical functions of complex unit vector  $\mathbf{n} = (\mathbf{k} + \mathbf{A}(t_s))/\kappa$  and  $C_{\kappa\ell}$  is the asymptotic coefficient of a bound state in an atom. An approximate value for  $C_{\kappa\ell}$  can be taken, e.g., from [10]. For ground states of atoms and negatively charged ions it is of the order of one (exactly 1 for hydrogen and equal  $1/\sqrt{2}$  for a zero-range potential). As this coefficient depends on the particular atoms being ionized, argon gas is assumed throughout this Chapter. The ground state for the single active valence electron is  $3p$  and  $C_{\kappa 1} = 0.95$ . Due to the probability of ionization significantly dropping with the increase of the magnetic quantum number  $|m|$  [10], considering the ionization from  $m = 0$  states exclusively is sufficient. To this end, the required formula for the prefactor reads

$$\mathcal{P}_{10}(\mathbf{k}, t_{s,j}) = iC_{\kappa 1} \sqrt{\frac{\mp 3i}{\pi E_0 a'(\omega t_{s,j})}}, \quad j = 1, 2, 3, 4 \quad (87)$$

with  $a'(\omega t)$  being the derivative of a function defined in Eq. (73) and  $+$  or  $-$  signs referring to saddle points  $\omega t_{s1,3}$  or  $\omega t_{s2,4}$ , accordingly. Details of the derivation can be found, e.g., in Appendix A of [6].

The other correction to the SFA-predicted ionization rate reflects the influence of the Coulomb potential of the residual ion on the post-ionization movement of a free electron in a laser field. In the framework of Chapter 2, circular fields with a small amplitude of the second component were mainly considered. The generated laser-driven electrons followed spiral classical trajectories and did not return close to the parent ion. Therefore, the influence of the latter was safely omitted there. Now that the two-color linear laser fields are considered, the inclusion of a correspondent correction becomes necessary as it significantly increases the ionization rate (see, e.g., articles [161–164], reviews [6, 10] and references therein). For small or moderate values of the Keldysh parameter,  $\gamma \simeq 1$ , the influence of the Coulomb field can be taken into account by introducing its contribution,  $U_C(r) = -Z/r$  to the action:

$$S_0 \rightarrow S_0 + S_C, \quad (88)$$

$$S_C = Z \int_{t_s}^{\infty} \frac{dt}{r_0(t)}. \quad (89)$$

Here,  $\mathbf{r}_0(t)$  is the Coulomb-free classical trajectory of an electron in the laser field obtained by solving the classical equation of motion

$$\ddot{\mathbf{r}}_0(\mathbf{t}) = -\mathbf{E}(\mathbf{t}) \quad (90)$$

but with initial conditions corresponding to the complex-valued velocity:

$$\mathbf{r}_0(t_s) = 0, \quad \dot{\mathbf{r}}_0^2(\mathbf{t}_s) = (\mathbf{k} + \mathbf{A}(\mathbf{t}_s))^2 = -2\mathbf{I}_p. \quad (91)$$

The initial time is defined as the saddle point  $t_s$ , which is a complex number making the trajectory  $\mathbf{r}_0(t)$  complex even at real times  $t$ . The denominator in (89) is analytically continued to the complex plane as  $\sqrt{\mathbf{r}_0(t)^2}$  [6, 164]. In the limit  $t \rightarrow t_s$  the solution to Eq. (90) with initial conditions (91) gives  $\mathbf{r}_0(t)^2 \approx -2I_p(t - t_s)^2$ , making the action (89) diverge logarithmically at its lower limit. This can be easily cured with a regularization procedure by matching the action (89) to the asymptotic form of the wavefunction of the initial state in the way it was shown in [161]. The regularized action then reads [6]

$$S_C = -in_* \ln(2iI_p t_*) + \int_{t_s}^{t_*} \left\{ \frac{Z}{r_0(t)} + \frac{in_*}{t - t_s} \right\} dt. \quad (92)$$

Here,  $n_* = Z/\sqrt{2I_p}$  is the effective quantum number and  $t_* \rightarrow \infty$  is a real number whose value does not affect the observables.

Evaluating the action (92) along the trajectory that leads to the most probable momentum  $\hat{\mathbf{k}}$  suffices to estimate the Coulomb-related multiplier in the total ionization rate. For a monochromatic field,  $\xi = 0$ , this momentum is equal to zero, and the correspondent saddle point is  $\omega t_s = \pi/2 + i \sinh^{-1} \gamma$  (see Sec. 1.2.3). Computing (92) for an arbitrary momentum  $\mathbf{k}$  would require an accurate choice of the integration path: additionally to the second-order zero at  $t = t_s$ , the complex-valued function  $\mathbf{r}_0(t)^2$  has other first-order zeros which are the branching points of the integrand in (92) [165, 166]. Thanks to the

trajectory for the most probable momentum being real along the real time axis, no regularization procedure is required, and the integration path can be reduced to the vertical segment between  $t_s$  and  $t_0 = \text{Re } t_s$  as the integral along the real time axis does not change the imaginary part of the Coulomb action and does not affect the magnitude of the final Coulomb-related factor (93) in the ionization rate. Integration in (92) is then conducted analytically, giving the well-known result [10, 161]

$$Q_C = \left| e^{iS_C} \right|^2 = \left( \frac{2}{F} \right)^{2\bar{Z}} \quad (93)$$

for the Coulomb factor, magnifying the ionization yield. The constant  $F$  here is the so-called reduced laser field, which is equal to the ratio of the laser field strength and the characteristic electric field strength in an atomic bound state:

$$F = \frac{E_1}{E_{\text{at}}} = \frac{E_1}{(2I_p)^{3/2}}. \quad (94)$$

Its value is typically about  $0.01 \div 0.1$  in strong-field ionization experiments. Thus, the Coulomb field drastically increases the total ionization rate compared to the zero-range potential case. The Coulomb correction (92) to the action could be evaluated more precisely if the Coulomb force was included in Eq. (90) [6, 167]. However, the related contribution giving an additional factor [167]

$$Q_{C,2} = \left( 1 + \frac{2\gamma}{e} \right)^{-2\bar{Z}}, \quad e = 2.718... \quad (95)$$

to (93) is only important for  $\gamma \gg 1$  and can be safely omitted throughout the following calculations.

In the general case of a two-color field (73) with  $\xi \neq 0$ , one has to perform the integration in (92) numerically. The most probable trajectory then relates to the momentum  $\hat{k}_x = A_0 \hat{q}_x$  aligned with the polarization axis. This trajectory has no imaginary part along the real time axis and is described by the saddle-point equation giving the initial time  $\tau_s = \omega t_s$  together with the initial condition (90):

$$\hat{q}_x \tau_{i,j} + \cos \tau_{r0} \sinh \tau_{i,j} + \frac{\xi}{2} \cos(2\tau_{r0} + \phi) \sinh(2\tau_{i,j}) = 0 \quad (96)$$

where  $\tau_{s0} = \tau_{r0} + i\tau_{i0}$ . Again, the integration in (89) can be reduced to the vertical line between  $t_s$  and  $t_0 = \text{Re } t_s$  of the total complex path. Performing the respective calculation of (89) for each of the saddle points  $t_{s1}, \dots, t_{s4}$  (43-44) gives the ionization amplitude

$$\mathcal{M}(\mathbf{k}) \approx \sum_j \mathcal{P}(\mathbf{k}, t_{s,j}) e^{iS_0(\mathbf{k}, t_{s,j}) + iS_C(\hat{\mathbf{k}}, t_{s,j})}. \quad (97)$$

By inserting (97) in Eq. (81) one may achieve an estimate for the total ionization probability  $W = wT$ , which is displayed in Fig. 3.2. This quantity strongly depends on the intensity of the second component of the laser  $I_2$ . Increasing  $2\xi$  from 0 to 0.5 gives ap-

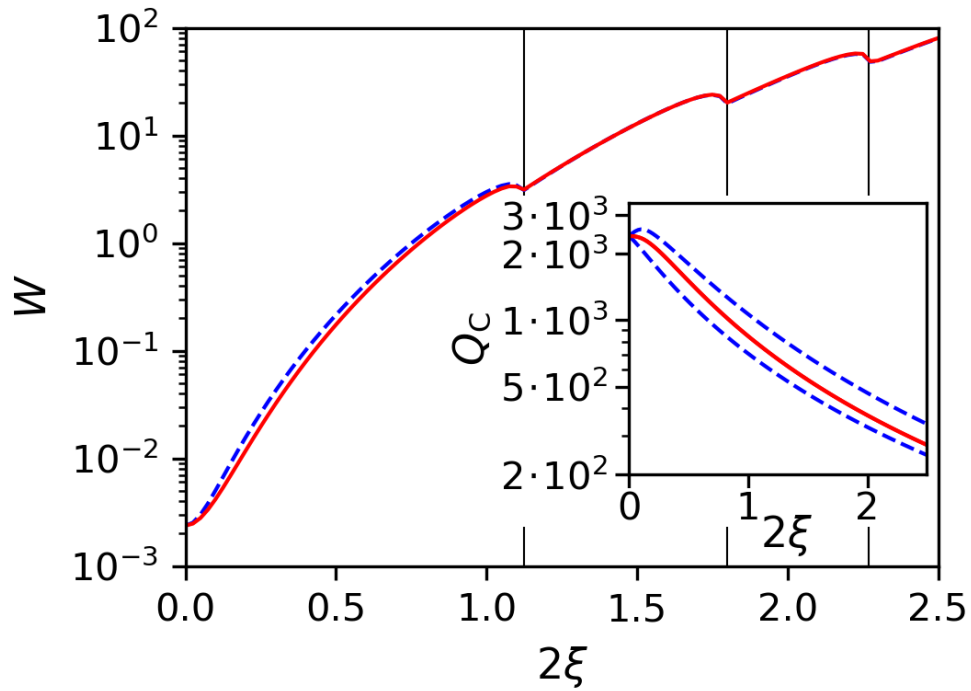


**Figure 3.2: Ionization probability estimate**  $W = wT$  as a function of  $2\xi$  for argon irradiated by a  $T = 100$ -fs-long pulse from a Ti:sapphire laser ( $\lambda = 800$  nm) with  $I_1 = 5 \cdot 10^{13}$  W/cm<sup>2</sup>. Result for the phase shift  $\phi = 0$  between the components is shown with a red thick solid line, for  $\phi = \pi/2$  with a blue dashed. Values of  $\xi$  corresponding to closings of the ionization channels are indicated with black vertical lines. The inset shows the Coulomb factor  $Q_C = |\exp(iS_C)|^2$  as a function of  $2\xi$  for  $\phi = 0$  (red solid line) and  $\phi = \pi/4$  (blue dashed line). In the latter case, these Coulomb factors differ for saddle points  $t_{s1}$  and  $t_{s2}$ . Adapted from [27]. © 2015 by the American Physical Society.

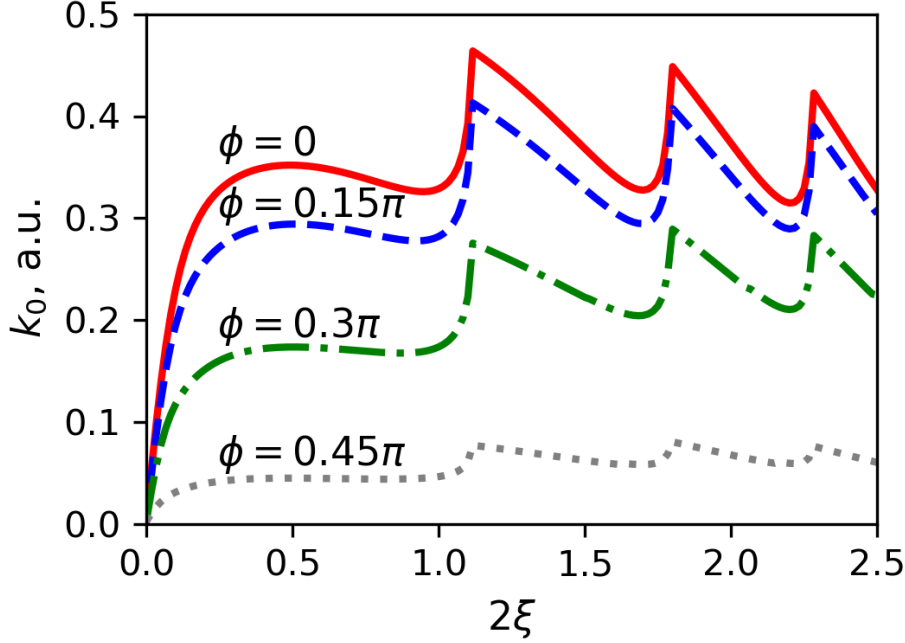


**Figure 3.3:** Average photoelectron momentum as a function of  $2\xi$  for various relative phase shifts  $\phi$  between the components of the laser field calculated according to Eq. (83) for argon. Laser intensity is chosen  $I = 5 \cdot 10^{13} \text{W/cm}^2$ , wavelength is equal to  $\lambda = 800 \text{nm}$ .

proximately an order of magnitude higher ionization degree. The ionization probability  $W$  provides the value of  $\xi_{\text{sat}}$ , which (at other parameters being fixed) optimizes the scheme so that the condition  $\tau_{\text{sat}} \simeq T$  is satisfied. At values  $\xi > \xi_{\text{sat}}$  the saturation occurs within a short fraction of the laser pulse, raising the upper limit of further emitted frequencies  $\nu_2$ . As a result, the radiation spectrum extends far beyond the THz domain. Therefore, one has to avoid conditions for which  $W \gg 1$  in the optimization of the THz output. For parameters from Fig. 3.2 one has  $2\xi_{\text{sat}} \approx 0.9$ .

Besides that, Fig. 3.2 allows to conclude that the phase shift  $\phi$  only weakly affects the ionization probability. However, as shown in Fig. 3.3, it strongly influences the average photoelectron momentum  $k_0$  (see definition in Eq. (83)) and, consequently, the average residual current  $j_0 \sim -k_0$ . One may conclude from Fig. 3.3 that the phase shift  $\phi = 0$  (in a two-color field described by (73)) remains optimal at all values of  $\xi$  and not just in the limit of small  $\xi$  when the current scales linearly with the weaker field (see Eq. (77)). This linear dependence of the photoelectron current on the value of  $2\xi$  only lasts until  $2\xi \approx 0.2 \div 0.3$ , which coincides with the limitation  $2\xi \ll 1/\gamma$  on its applicability established in [128, 130]. For  $2\xi \geq 0.5$  the value of the rate is determined mostly by the second harmonic. However, although the first harmonic hardly ionizes the gas, it still introduces the asymmetry necessary for the generation of a nonzero net current.

Next, Fig. 3.4 demonstrates the dependence of the net photoelectron momentum on the intensity  $I_1$  of the main component of the laser. The expected increase is observed at small intensities reaching the peak around  $I_1 \approx 3 \cdot 10^{14} \text{W/cm}^2$  with a subsequent decline. This behaviour reflects the competition between the two factors. Namely, the linear growth of

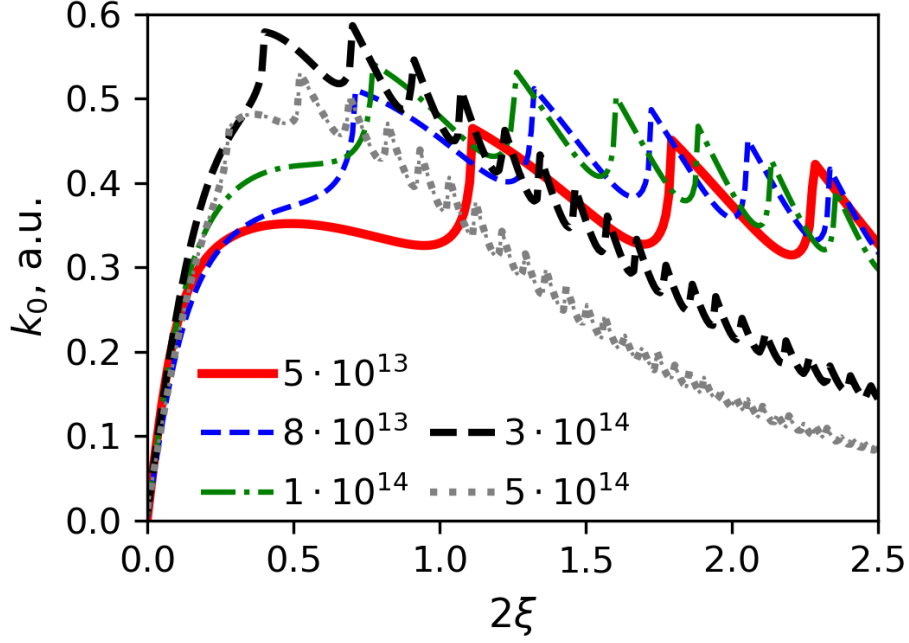


**Figure 3.4: Average photoelectron momentum as a function of  $2\xi$  for various intensities  $I_1$  of the main laser field:**  $3 \cdot 10^{13}$  W/cm<sup>2</sup> (red thick solid line),  $8 \cdot 10^{13}$  W/cm<sup>2</sup> (blue dashed),  $3 \cdot 10^{14}$  W/cm<sup>2</sup> (green dash-dotted),  $5 \cdot 10^{14}$  W/cm<sup>2</sup> (black dashed),  $8 \cdot 10^{14}$  W/cm<sup>2</sup> (grey dotted). Other parameters: argon,  $\lambda = 800$  nm,  $\phi = 0$ . Adapted from [27]. © 2015 by the American Physical Society.

the characteristic momentum  $A_0$  with the increase of the field amplitude  $E_1$  is opposed to the non-linear behaviour of the net photoelectron momentum  $q_0 = k_0/A_0$  as a function of  $\xi$ . Therefore, despite the ionization saturation, **the intensity of the main component in a two-color linearly polarized laser field can be optimized for the generation of THz radiation, maximizing the net photoelectron current.** This is achieved at  $I_1 \approx 3 \cdot 10^{14}$  W/cm<sup>2</sup> for parameters as those in Fig. 3.4.

At last, the question of optimization with respect to the field-strength ratio  $2\xi$  should be addressed. Oppositely to the linear growth at small  $\xi$ , at large values of  $\xi$  the net photoelectron momentum  $k_0$  decreases. This agrees with the dependence predicted in Eq. (80), as then the regime where the  $\omega$ -component plays the role of a small perturbation is reached [126, 128, 130]. To avoid the case of saturation, consider now the total intensity  $I_1 + I_2$  being fixed rather than fixing  $I_1$ . Such settings are also simpler for performing a parametric scan experimentally. To this end, in Fig. 3.5 the average momentum  $k_0$  is displayed at constant  $I_1 + I_2$  for all  $\xi$ . The most important outcome from Figs. 3.4–3.5 is that **the net photoelectron current maximizes at almost equal intensities of the two-color laser components** ( $2\xi \simeq 1$ ). Both of them contribute sufficiently non-linearly. Achieving these conditions in an experiment requires the additional check that the saturation of ionization does not occur earlier. Such optimization takes place for parameters as those in Fig. 3.3.

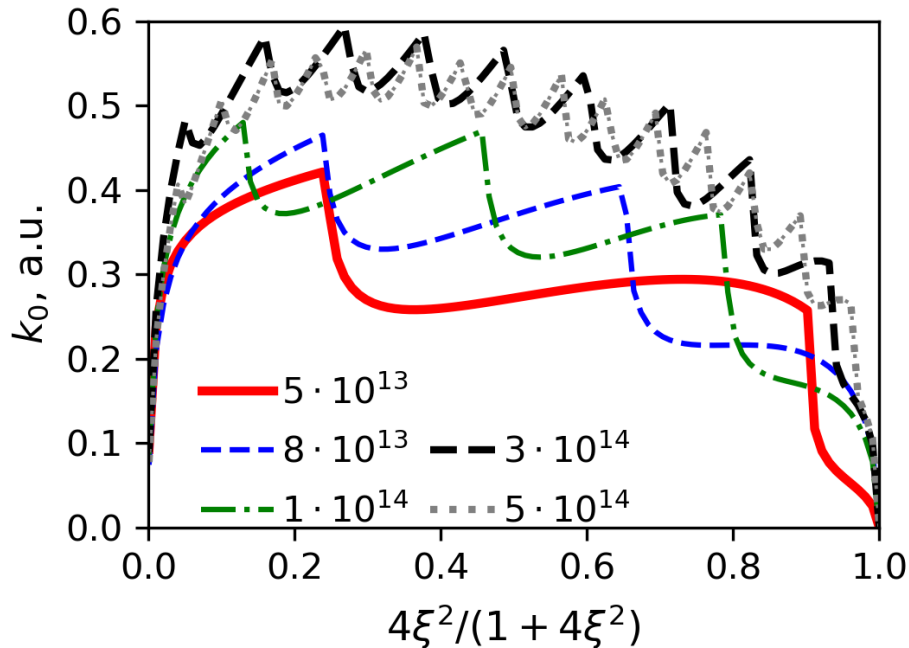


**Figure 3.5:** Average photoelectron momentum as a function of  $I_2/(I_1 + I_2)$  for various total intensities  $I_1 + I_2$  of the combined two-color laser field:  $3 \cdot 10^{13}$  W/cm<sup>2</sup> (red thick solid line),  $8 \cdot 10^{13}$  W/cm<sup>2</sup> (blue dashed),  $3 \cdot 10^{14}$  W/cm<sup>2</sup> (green dash-dotted),  $5 \cdot 10^{14}$  W/cm<sup>2</sup> (black dashed),  $8 \cdot 10^{14}$  W/cm<sup>2</sup> (grey dotted). Other parameters: argon,  $\lambda = 800$  nm,  $\phi = 0$ .

Interestingly, due to the increase of the ponderomotive energy (23)

$$U_p = \frac{E_1^2}{4\omega^2}(1 + \xi^2) \quad (98)$$

and discrete jumps of the threshold number of photons  $N_{\min}$  in (22), the ionization rate becomes non-monotonic in correspondent narrow domains of  $\xi$  (see the vertical lines in Fig. 3.2). As the lowest threshold for ionization disappears accordingly, the denominator in (83) reduces, which leads to the sharp peak in the net photoelectron momentum value as seen in Figs. 3.3–3.5. However, in the experimental realization this effect might be masked by the averaging of the signal over the focal spot and by the finiteness of the pulse duration.

Finally, it should be mentioned that the problem of intensity optimization was recently generalized by considering other  $a\omega : b\omega$  frequency ratios, namely,  $2 : 3$  and  $1 : 4$  [168]. With the total intensity  $I_a + I_b$  fixed, the optimal frequency ratio (among the studied in [168] and, presumably, in general) is confirmed to be  $1 : 2$ , and the optimal intensity ratio is close to  $1 : 1$ , confirming the results presented in [27] and in the present thesis.

### 3.3 OPTIMIZING POLARIZATIONS OF AN INTENSE TWO-COLOR FIELD COMPONENTS

Part of the results shown in this Subsection are presented in [169].

This Section of the thesis is devoted to optimization of the photoelectron current with a focus being made on the polarizations of the two-color laser fields. A substantial number of previously conducted experiments as well as theoretical investigations in the area of plasma-induced THz radiation creation have been aimed at the case of linear polarization of the ionizing laser [27, 125–129]. Studies addressing elliptical or circular polarizations also exist though and were devoted to gaining control over the polarization of the resulting THz radiation [170, 171]. Importantly, in [172] it was reported that the usage of bi-circular two-color fields may exceed the THz power almost 5 times compared to the case of  $\uparrow\uparrow$  fields (at equal intensities  $(1 \div 5) \cdot 10^{14} \text{ W/cm}^2$  of the main, 800 nm, component and a 20 times weaker component with doubled frequency). There, the benefit of the scheme with the main field being circularly polarized was demonstrated experimentally and theoretically using the theory of tunnel ionization. As follows from Eq. (77) in the previous Section, in the tunneling limit for ionization by two-color bi-linear fields, the scaling for the net momentum reads  $A_2 = \xi A_0$  [128, 130, 173] which is still much less than  $A_0$  as long as  $\xi \ll 1$ . The latter condition is, apparently, not easy to overcome in the experiment.

Without the second component at all ( $\xi = 0$ ), the net photoelectron momentum corresponding to a linearly polarized field has a value of the order of  $\sqrt{F} A_0$ , with  $F$  being the reduced laser field, which is equal to ratio between the laser field and the characteristic atomic field strength (see Eq. (94)). Importantly, ionization is efficient already for fields correspondent to  $F \ll 1$  [6, 10]. For example, in [172] the gases of argon or xenon that have  $I_p=12.1 \text{ eV}$  and  $15.8 \text{ eV}$ , respectively, were used as targets. The intensities were in the range  $I \sim (1 \div 5) \cdot 10^{14} \text{ W/cm}^2$ , which corresponds to  $F \simeq 0.03 \div 0.08$ .

In contrast to this, a circularly polarized field produces photoelectrons with momenta of the order of  $A_0$ , i.e.,  $1/\sqrt{F}$  times higher. Complementing such a field with the double-frequency component, even of much weaker intensity, breaks the symmetry and creates a preferable direction of emission <sup>7</sup>. To this end, the THz radiation generation using a two-color field of a configuration with  $\odot\odot$  or circular and linear ( $\odot\uparrow$ ) polarizations at different laser wavelengths is further examined. The second component is assumed to be weak compared to the first one throughout this Chapter.

As previously, the analysis will begin from considering the problem in a single-atom approximation, and the laser field will be defined through its vector potential parametrized according to Eq. (12). The frequency ratio will be fixed to  $a : b = 1 : 2$ , and the polarization

---

<sup>7</sup> For a circularly polarized second component of such a field this statement is only valid if the two polarizations are  $\odot\odot$  ( $\epsilon_a = \epsilon_b$  in Eq. (99)). Otherwise, as was discussed previously, a two-color field with  $\odot\odot$  polarizations ( $\epsilon_a = -\epsilon_b$  in Eq. (99)) obeys an  $(a+b)$ -fold symmetry which is then inherited by the PES, leading to zero net momentum. The experimental confirmation of this reasoning can be found in [172]. One should note that  $\odot\odot$  can instead be used for another kind of frequency conversion — at comparable intensities  $I_a \sim I_b$  they are known to be efficient in HHG with additional control over the polarization of the output radiation [174–180].

of the main  $\omega$  component will be restricted to circular ( $\epsilon_a = 1$ ). The resulting formula for the vector potential reads

$$\mathbf{A}(t) = A_0 f(t) \left[ \begin{aligned} &\left( \cos(\omega t) + \xi \cos(2\omega t + \phi) \right) \mathbf{e}_x \\ &+ \left( \sin(\omega t) + \epsilon_2 \xi \sin(2\omega t + \phi) \right) \mathbf{e}_y \end{aligned} \right]. \quad (99)$$

Here,  $\epsilon_2$  is the ellipticity of the second  $2\omega$  component. The value  $\epsilon_2 = \pm 1$  corresponds to  $\circ\circ$  polarization and  $\epsilon_2 = 0$  to  $\circ\uparrow$ . The form of the envelope of the laser pulse is chosen

$$f(t) = 1 - \sin^4 \left( \frac{\omega t}{2n_c} \right), \quad \omega t \in [0, 2\pi n_c] \quad (100)$$

where  $n_c$  is the total number of optical cycles in the pulse.

In order to determine the optimal polarizations for the components of a two-color laser field defined via the vector potential according to Eq. (99), the PES in the  $x$ - $y$  polarization plane have been computed. As before, the wavelength of the main component was chosen equal to the commonly applied  $\lambda = 800$  nm (Ti:sapphire laser) and the intensity was taken equal to  $I_1 + I_2 = 10^{14}$  W/cm<sup>2</sup> with  $I_1 : I_2 = 0.95 : 0.05$ . For benchmarking via numerically solving the TDSE with QPROP 2.0 [49], a pulse duration of  $n_c = 3$  optical cycles was considered. Further, a comparison to the prediction from the SFA has been made. The SFA-based calculations were performed with the effect of the residual ion Coulomb field omitted. This approximation is adequate here, since the classical trajectories of photoelectrons created by such a field have an almost spiral shape and never return close to the origin (this would remain valid even at high  $I_2$  intensities, see, e.g., [181]). The influence of the Coulomb field then mainly affects the orientation of the PES, globally rotating it in the polarization plane without changing the width of the distribution or the average momentum energy of photoelectrons [92, 93]. Such a rotation would result in the change of the output THz radiation polarization though, and in fact could be used as an independent measure for this Coulomb effect. The control of the THz radiation polarization is addressed, e.g., in [170, 171, 182–184] but remains out of scope of the present thesis.

The calculated PES are presented in Figs. 3.6 and 3.7. The correspondent conclusions can be summarized as follows:

- In the case of  $\circ\circ$  polarizations (see Fig. 3.6 (a) and (b)) a quantitative agreement between the two approaches (numerical solution to the TDSE and semi-analytic SFA) is achieved. This is complemented by Fig. 3.7 (a), which shows momentum distributions along the net photoelectron momentum  $\langle \mathbf{k} \rangle$ , integrated over the transverse momentum. As expected, the net photoelectron momentum appears to be close to  $|\langle \mathbf{k} \rangle| \simeq A_0$  and are noticeably higher than those for  $\uparrow\uparrow$  fields.
- In the case of  $\circ\uparrow$  polarizations at relative phase value  $\phi = 0$  (see Fig. 3.6 (c), (d)) or  $\phi = -\pi/2$  (see Fig. 3.6 (e), (f)) the results agree on a qualitative level only. Importantly, the SFA predicts substantially sharper peaks than the exact solution

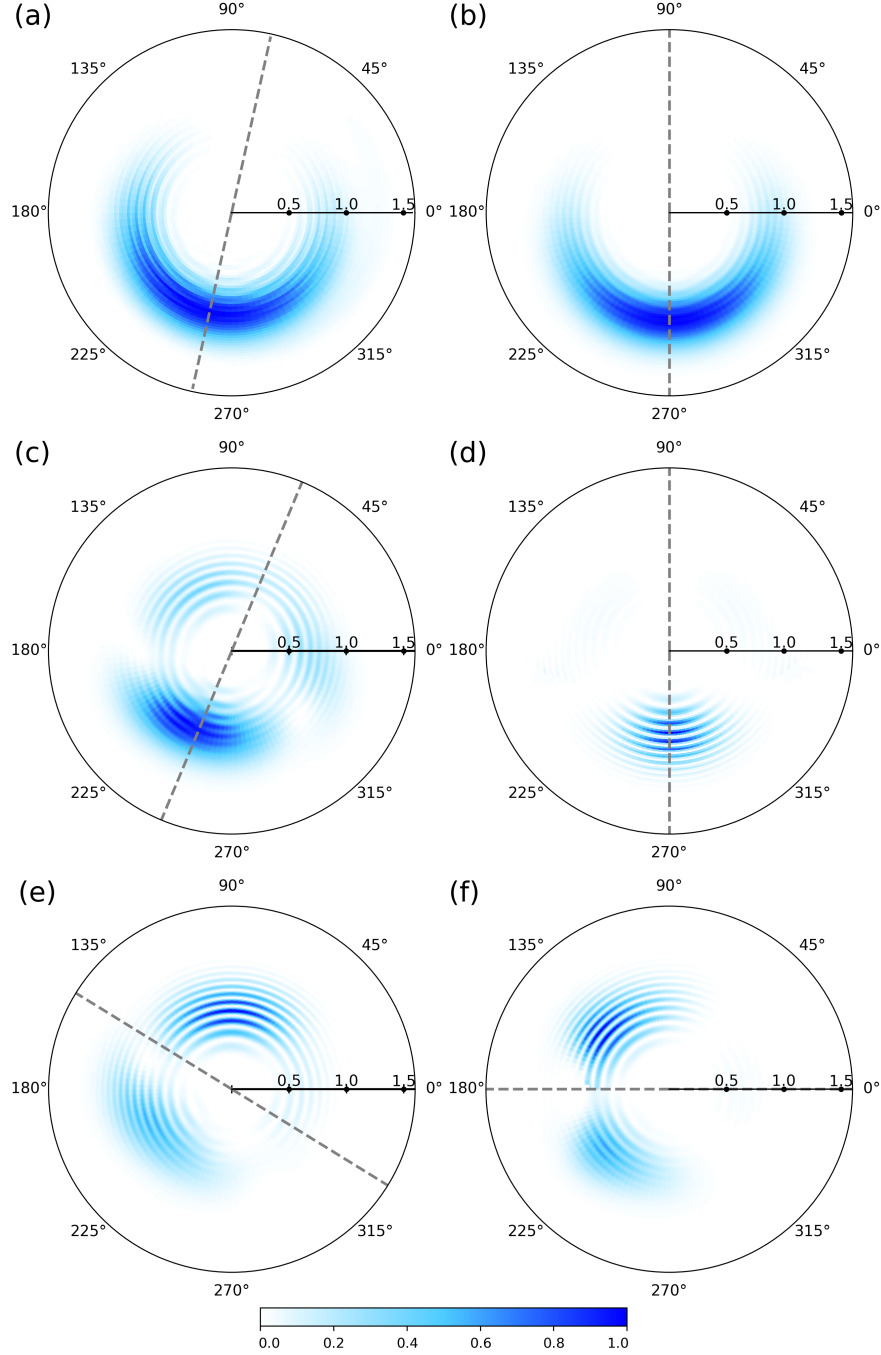


**Figure 3.6: Momentum distribution in the polarization plane for hydrogen in a two-color field** with  $n_c = 3$  cycles of total duration defined according to (99) with wavelengths 800 and 400 nm. Their total intensity is  $I_1 + I_2 = 10^{14}$  W/cm<sup>2</sup> and the ratio between them is  $I_2 : I_1 = 0.95 : 0.05$ . In (a, c, e) the results obtained from the numerically solved TDSE are shown, in (b, d, f) those predicted by the SFA. Polarization of the main  $\omega$  component is circular ( $\odot$ ). Polarization of the  $2\omega$  component is either (a, b) circular corotating ( $\odot$ ) or (c-f) linear ( $\downarrow$ ) with phase shift  $\phi = 0$  in (a-d) and  $\phi = -\pi/2$  in (e, f). The dotted lines show the axes along the average momentum  $\mathbf{k}_0$ . Horizontal lines indicate radial momentum values in atomic units. Adapted from [169]. © 2018 by the American Physical Society.

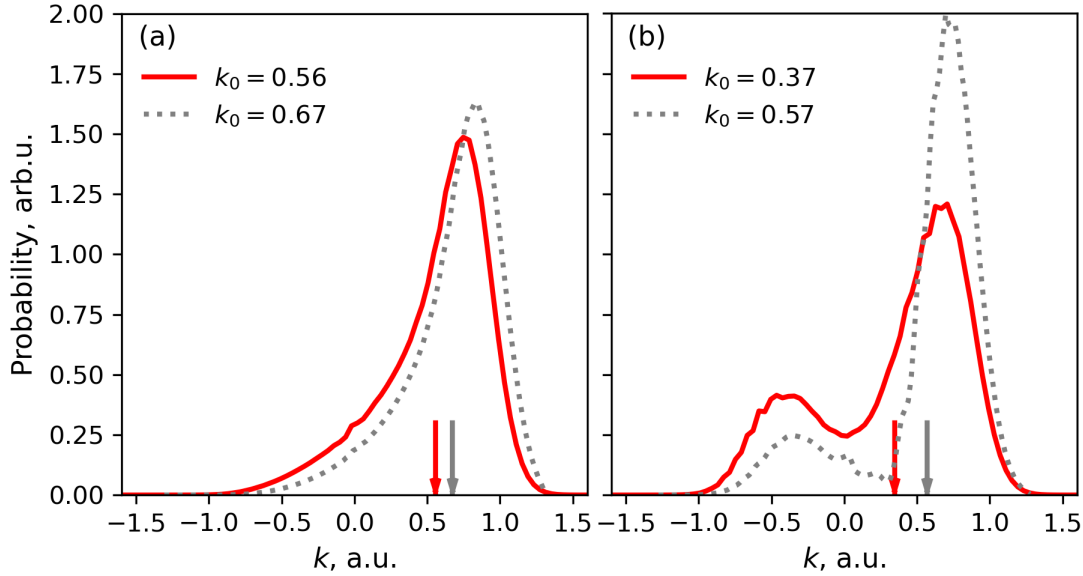


**Figure 3.7:** PES along the net momentum  $k_0$  axis and integrated over the **transverse momentum** indicated by dashed lines in Fig. 3.6. Red solid lines show the TDSE-based prediction, grey dotted – the SFA-based. Subplot (a) demonstrates the distribution for a  $\bigcirc\bigcirc$  field (i.e., the integrated data of Fig. 3.6 (a, b)), subplot (b) shows the distribution for a  $\bigcirc\uparrow$  fields taken from Fig. 3.6 (c, d). Characteristic field momentum is equal to  $A_0 = 0.64$  a.u., and the values of the net momenta are displayed in the legends. Adapted from [169]. © 2018 by the American Physical Society.

to the TDSE. Comparing the net photoelectron momenta between all TDSE-based results in Fig. 3.7 shows that the  $\bigcirc\uparrow$  configuration is less effective than  $\bigcirc\bigcirc$ . Additionally, Figs. 3.6 (c–f) reveal that changing the relative phase  $\phi$  in Eq. (99) for a  $\bigcirc\uparrow$  scheme significantly deforms the resulting PES. By this, the output radiation becomes strongly dependent on the fluctuations in the relative phase  $\phi$ . The same drawback is intrinsic to applications of two-color co-linear fields ( $\uparrow\uparrow$ , see previous Section) and bi-elliptical fields [185].

To wind up, Figs. 3.6 and 3.7 suggest that **bi-circular co-rotating ( $\bigcirc\bigcirc$ ) polarizations are optimal for efficient generation of THz radiation.**

### 3.4 OPTIMAL WAVELENGTHS IN AN INTENSE TWO-COLOR LASER FIELD

Part of the results of this Subsection are presented in [169].

Up to this Section, all theoretical investigations in the present Chapter were focused on the application of two-color laser pulses with wavelengths of their components equal to 800nm and 400nm, being a specific example of a 1 : 2 frequency ratio. Configurations with other ratios (2 : 3, 3 : 4, 1 : 4, etc.) are also capable of creating strong net photoelectron currents from a gaseous media, at least when the intensities of the two components are comparable in magnitude (see, e.g., [168, 186, 187] where this case was investigated for  $\uparrow\uparrow$

polarizations). Using pulses with incommensurate frequencies at comparable intensities may give additional control over the phase of the emitted THz radiation [188]. Nonetheless, in [186] it has been predicted (at least at equal intensities  $I_a = I_b = 10^{14}$  W/cm<sup>2</sup> and for a wavelength of the  $a\omega$  component equal to 800 nm) that the magnitude of the residual current gets maximized if  $a : b$  frequency ratios are chosen equal to either 1 : 2 or 2 : 1. Besides that, considering the fact that schemes with other ratios are more difficult to arrange in an experiment, their development is less promising. In all following investigations of this Section the ratio will also be restricted to 1 : 2. The polarization of the two-color field will be fixed to  $\odot\odot$ , as it was shown to be superior over others in the previous Section. The central issue to consider is whether it is advantageous to use wavelengths higher than the commonly applied 800nm and 400nm. The strength of the second component of the total field is again restricted to be weak compared to the first ( $\xi \ll 1$ ), making the Coulomb-free SFA-based analysis applicable. Besides that, as discussed above, configurations with  $\xi \ll 1$  are easier in their experimental implementation while the net photoelectron current still scales with the magnitude of the main component of the laser.

The major part of the calculations are performed within the SFA. The main reason for working within the SFA and not obtaining the PES directly with the accurate numerical TDSE solver is the computational demand of the latter in the case of non-linearly polarized laser fields. In particular, for the parameters in Figs. 3.6 and 3.7 the convergence of the solution with respect to the numerical grid was reached by expanding the wavefunction in spherical harmonics corresponding to orbital quantum numbers up to  $\ell_{\max} = 50$ , which corresponds to 2500 channels of different  $\ell$  and  $m$  in the total expansion in spherical harmonics (47) being involved. Increasing the wavelength of a laser would result in a further extension of this upper boundary, making such calculations impracticable (for more details about numerical complexity in QPROP see Chapter 1.3 and [45, 49, 51]).

In the previous Section, the results were additionally verified by the comparison to the numerical solutions to the TDSE. The accuracy of the results obtained with the SFA is known to improve in the tunneling regime, i.e., when the Keldysh parameter,  $\gamma$ , becomes less than one. For argon exposed to a laser pulse with intensity  $3 \cdot 10^{14}$  W/cm<sup>2</sup> and wavelength  $\lambda = 800$  nm,  $1.6 \mu\text{m}$ ,  $2.4 \mu\text{m}$  or  $4.0 \mu\text{m}$ , the Keldysh parameter is equal to  $\gamma = 0.93/a$  with  $a = 1, 2, 3$  or  $5$ , correspondingly. Therefore, the SFA-predicted results should even better coincide with the numerical solutions to the TDSE at long wavelengths than it was the case for 800 nm shown in Fig. 3.7 (a).

In order to account for the enhancement in the output THz power with the increase of the laser wavelength beyond the single-atom response level, the following model including collective movement of the electron plasma has been established:

- The first and biggest simplification is the reduction of the dynamics in the model to the one-dimensional (1D) case. For that purpose the value of  $z$ , the coordinate in the laser propagation direction, is taken fixed. Secondly, the initial PES is taken in the  $k_x$ - $k_y$  polarization plane with  $k_z = 0$  (see Fig. 3.8 (a)) and is then integrated over the axis transverse to the net photoelectron momentum direction,  $\mathbf{k}_0$ , which is indicated by a grey dashed line in Fig. 3.8 (a). The resulting 1D PES are displayed in

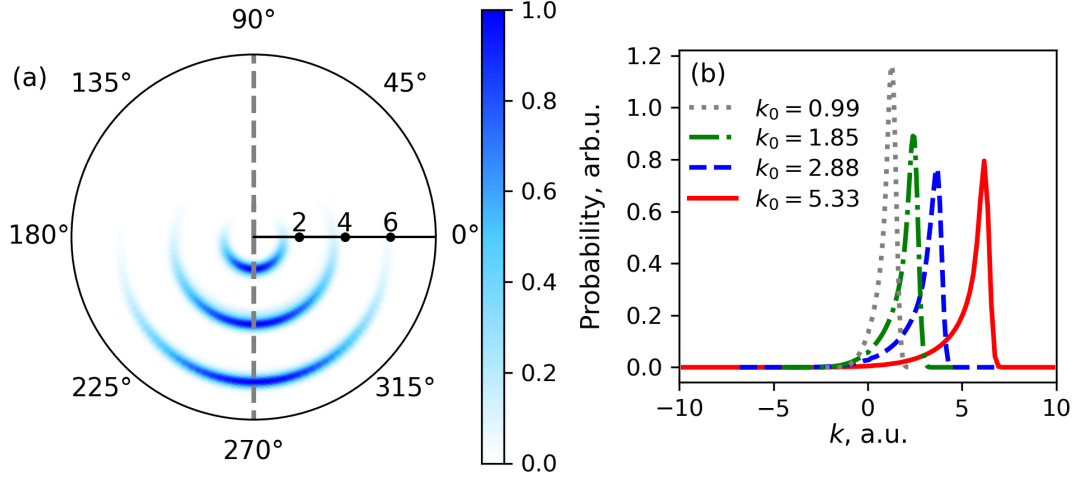


**Figure 3.8: PES for argon irradiated by a two-color laser field.** From center to the boundary of the subplot (a) the spectra for laser wavelengths 800 nm, 2.4  $\mu\text{m}$  and 4.0  $\mu\text{m}$  are shown. In (b), the PES along the net momentum  $\mathbf{k}_0$  axis and integrated over the transverse momentum (grey dashed line in (a)) are shown for the wavelength of the main component equal to 800 nm (dotted grey line), 1.6  $\mu\text{m}$  (dash-dotted green), 2.4  $\mu\text{m}$  (dashed blue) or 4.0  $\mu\text{m}$  (red solid). The values of the net momentum  $k_0$  are indicated in the legend. In each case the total laser intensity is equal to  $I_1 + I_2 = 3 \cdot 10^{14} \text{W}/\text{cm}^2$  with  $I_1 : I_2 = 0.95 : 0.05$ , and the total pulse duration is  $T_p = 25.88$  fs.

Fig. 3.8 (b). The electrons dynamics are described in the (1+1) dimensional phase-space  $(x, k)$ , and layers with different values of the spatial coordinate  $z$  are treated independently. Such an approximation is reasonable due to a narrow momentum distribution in the direction of the laser pulse propagation:  $\Delta k_z \simeq \sqrt{I_p F} \ll \sqrt{I_p}$  and  $\Delta k_z \ll A_0$ . Certainly, this geometry of the model forbids any investigation of the polarization and the geometrical properties of the emitted THz radiation.

- Secondly, the initial distribution of electrons in the plasma (see left column in Fig. 3.9) is treated as instantaneously formed while the THz radiation emission occurs progressively at sufficiently longer times. Indeed, frequencies of about  $\nu = 10$  THz correspond to times about  $1/\nu \simeq 100$  fs. These times are approximately four times longer than the duration of the laser pulse used in [172]. For the pulses of  $T_p \sim 25$  fs duration used in the present simulations this contrast is even higher, thus, making the assumption well justified.
- Finally, the influence of various layers of plasma is addressed as follows. The plasma layers located at different  $z$  coordinates contribute coherently to the total output radiation if the phase difference between them remains small at opposite edges of the full radiating area. Assuming the gas to be confined in a  $100 \mu\text{m}$ -long tube (as was the case in [172]) ensures having this value comparable to the THz radiation wavelength, meanwhile still being sufficiently smaller than the Rayleigh length for a weakly focused laser pulse. In such a scheme where the gaseous medium is limited in space in all directions and emits almost as a dipole, the effects of light propagation can be safely omitted.

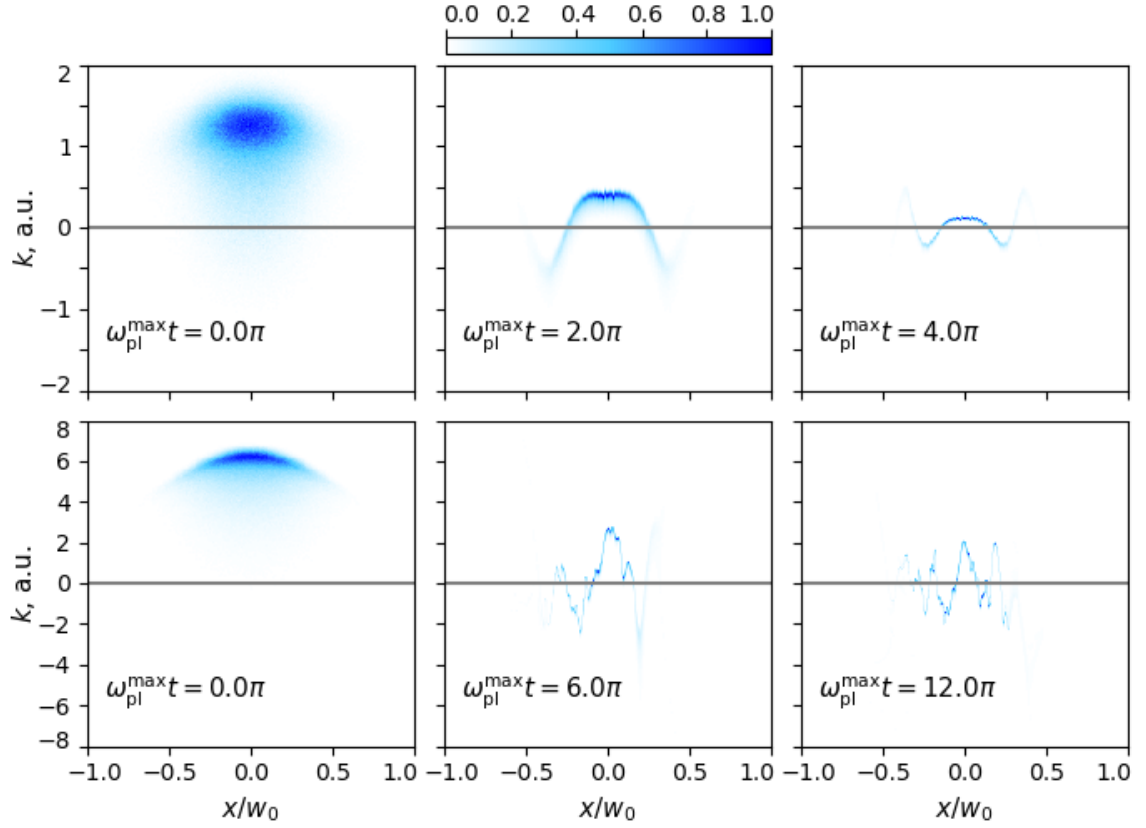


**Figure 3.9: Distribution function  $f_{z=0}(k, x, t)$  of electrons in the  $(x, k)$  plane at different times  $t$ .** Upper row corresponds to the laser wavelength 800 nm, lower – to 4  $\mu$ m. The peak laser intensity is  $I = 3 \cdot 10^{14}$  W/cm<sup>2</sup>. Characteristic length scale  $w_0 = 10$   $\mu$ m is equal to the Gaussian central beam waist (see Eq. (104)). The highest plasma frequency is  $\omega_{\text{pl}}^{\text{max}} = 2\pi \cdot 10$  THz. In each subplot the data is normalized on its maximum.

Under these approximations, the laser-free plasma dynamics can be described by the Vlasov-Maxwell equations for the electron distribution function  $f_z(k, x, t)$  defined in the phase-space at fixed  $z$ :

$$\{\partial_t + v_x \partial_x + E_x(x, t) \partial_k\} f_z(k, x, t) = 0 \quad (101)$$

$$\partial_x E_x(x, t) = 4\pi \int f_z(k, x, t) dk - 4\pi n_{i,z}(x). \quad (102)$$

Here,  $n_{i,z}(x)$  is the concentration of the static ions. Its value is equal to the initial concentration of electrons:

$$n_{i,z}(x) = n_{e,z}(x, t=0) = \int f_z(k, x, t=0) dk. \quad (103)$$

Importantly, the presence of the ionic background in Eq. (102) influences the net acceleration of the electron cloud and, consequently, the dipole radiation occurring after the laser pulse is over. The initial density (103) is calculated approximately according to the tunnel ionization formula for argon in a laser field with Gaussian intensity profile:

$$I_z(x) = \frac{I_0}{1+z^2/z_R^2} \exp\left(-\frac{2x^2}{w_0^2 [1+z^2/z_R^2]}\right). \quad (104)$$

Here,  $w_0$  is the Gaussian beam waist and  $z_R = \pi w_0^2/\lambda$  is the Rayleigh length. The parametric dependence (104) on the  $z$  coordinate enters Eqs. (101), (102) implicitly by determining the fixed  $n_{i,z}(x)$  and initial  $n_{e,z}(x, t=0)$ . The pair of Eqs. (101), (102) was solved with the help of the particle-in-cell (PIC) method in the region  $x \in [-5w_0, +5w_0]$  with the beam waist being  $w_0 = 10 \mu\text{m}$  for 21 layers with different  $z \in [-100 \mu\text{m}, 0]$ . For layers with  $z \in [0, +100 \mu\text{m}]$  the symmetry property was used:  $f_{-z}(k, x, t) = f_{+z}(k, x, t)$ . The boundary conditions for  $x$  were taken periodic. No limitation for the maximal electron momentum was assumed. Both these conditions did not affect the dynamics, because the ionic background enabled only a negligible fraction of electrons to reach the boundaries in the  $x$  direction. And even for those electrons that did reach the boundaries their momenta did not exceed the mean values characteristic for the applied laser pulse by more than a few times.

The vital feature of the constructed model is the inclusion of the effects of electron-ion and electron-electron collisions. The characteristic frequencies of those can be estimated according to the formulas [189]

$$\nu_{ei} \simeq \nu_{ee} \simeq \frac{4\pi n_e \Lambda}{T_{\text{eff}}^{3/2}} \equiv \nu \quad (105)$$

with  $\Lambda \simeq 5$  being the Coulomb logarithm and  $\nu_{ei}$  being the ion-electron collision frequency that is defined though transfer of momentum and not of energy [189]. This value can be estimated by introducing the effective temperature

$$T_{\text{eff}} = (\Delta k)^2/2, \quad (106)$$

defined via the momentum spread  $\Delta k$ . The latter can be obtained from the SFA (see Fig. 3.8). For an initial plasma density equal to  $n_e = 10^{18} \div 10^{19} \text{ cm}^{-3}$  (which is typical in the THz radiation generation experiments with two-color lasers) and the momentum spread equal to  $\Delta k \approx (0.3 \div 1.0) \text{ a.u.}$ , the collision frequency belongs to the interval between  $10^{11} \div 10^{13} \text{ s}^{-1}$ , which corresponds to timescales of  $0.1 \div 10 \text{ ps}$ , i.e., fits in the THz domain. A relatively fast decay of the plasma oscillations may significantly influence the irradiated spectrum. Inclusion of the collisions into the electron dynamics results in the following form of the equation of motion:

$$\ddot{x}_a(t) = -E_x(x_a, t) - \nu \dot{x}_a(t). \quad (107)$$

All values in Eq. (107) scale with charges  $Q_a$  and masses  $M_a$  of the macroparticles so that the equation eventually remains independent of them. At  $\nu = 0$  energy conservation has been successfully reproduced. Other types of elastic and inelastic collisions of electrons with atoms have been neglected in the model. For electrons with energies  $k^2/2 \approx 20 \div 500 \text{ eV}$ , corresponding to momenta according to the distributions in Fig. 3.8, the cross sections of elastic scattering and those of impact ionization are close to the geometrical cross section of an atom. In particular, for argon atoms, the impact-ionization cross section remains below  $\sigma_{\text{max}} \approx 3 \cdot 10^{-16} \text{ cm}^2$  [190]. Thus, taking the residual concentration of neutral atoms after laser-induced ionization equal to  $n_a \simeq 10^{18} \text{ cm}^{-3}$  and the same value for the concentration of electrons, one concludes that during the time of about  $\tau = 1 \text{ ps}$  the process of impact ionization could increase the electron concentration by  $\sigma_{\text{max}} n_a k_0 \tau \approx 0.1$  of its initial value. Here,  $k_0$  is the mean photoelectron momentum extracted from Fig. 3.8. Hence, the parameters used in the calculations shown in the present thesis suggest that the contribution of the impact ionization process to the plasma dynamics would not increase the plasma density by more than  $\sim 10\%$ .

The main parameters that determine the plasma dynamics are the initial distribution of electrons in the phase space  $f(k, x, t = 0)$ , the local plasma frequency

$$\omega_{\text{pl},z}(x) = \sqrt{4\pi n_{e,z}(x)} \quad (108)$$

and the collision frequency (105). By manipulating the wavelength, the intensity profile and the duration of the laser pulse, a desired degree of ionization (and, correspondingly, a required electron concentration,  $n_e$ ) can be achieved as well as a certain form of initial electron distribution function  $f(k, x, t = 0)$  and certain effective temperature  $T_{\text{eff}}$ . The plasma frequency varies from its maximal value  $\omega_{\text{pl}}^{\text{max}}$  reached in the center of the plasma spot down to zero at its edges. The degree of ionization and, hence, the value of  $\omega_{\text{pl}}^{\text{max}}$ , can be controlled by changing the duration of the pulse, the pressure in the gas chamber and the intensity of the laser. Consider, for example, argon gas under 200 mbar pressure irradiated by a laser with intensity equal to  $3 \cdot 10^{14} \text{ W/cm}^2$  and pulse duration of 40 fs. The PPT formula [10] predicts the degree of ionization to be about 40% giving  $\omega_{\text{pl}}^{\text{max}} \approx 6 \cdot 10^{13} \text{ s}^{-1}$ . This corresponds to  $\nu^{\text{max}} \approx 10 \text{ THz}$ . Exemplary snapshots of the plasma spot for such conditions are shown in Fig. 3.9. The damping of the oscillations due to the collision

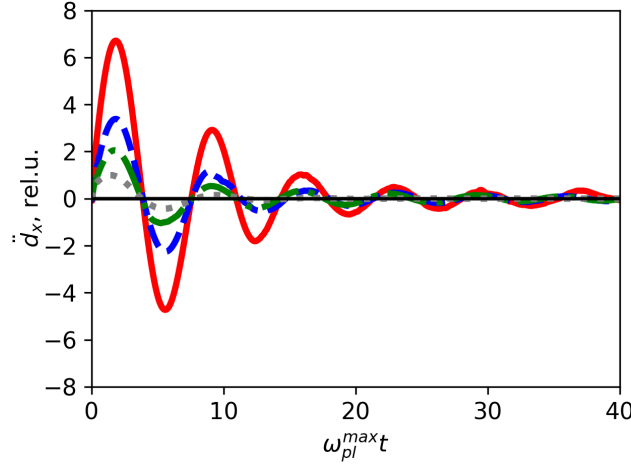


**Figure 3.10:** Dipole acceleration computed according to (109) as a function of time for argon under 200 mbar pressure irradiated by a two-color laser field of intensity  $3 \cdot 10^{14}$  W/cm<sup>2</sup> with the main component's wavelength being equal to 800 nm (dotted grey line), 1.6  $\mu\text{m}$  (dash-dotted green), 2.4  $\mu\text{m}$  (dashed blue) or 4.0  $\mu\text{m}$  (red solid).

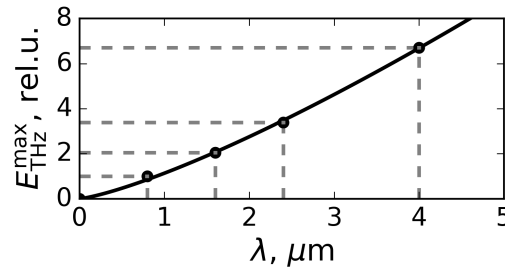


**Figure 3.11:** Relative magnitude of the electric field strengths as a function of the laser wavelength  $\lambda$ . All parameters are as in Fig. 3.10. The solid line represents the fitting with (110). Reprinted from [169]. © 2018 by the American Physical Society.

processes is less pronounced in the longer wavelength case. This effect is clearly observed in the time evolution of the total dipole acceleration of the whole plasma:

$$\ddot{d}_x(t) = -\Delta y \int dz \int dx n_{e,z}(x, t) \ddot{x}(t). \quad (109)$$

Its value is shown in Fig. 3.10. In (109),  $\Delta y = 100 \mu\text{m}$  is the width of plasma spot along the axis in the polarization plane orthogonal to the mean plasma oscillation direction. This value has been fixed for all laser wavelengths in order to exclude its possible influence on the emitted dipole radiation power. The electric field strength of the THz radiation is proportional to (109), which makes possible to extract the relative values of these amplitudes  $E_{\text{THz}}^{\text{max}}(\lambda)$ . The correspondent dependence on  $\lambda$  shown in Fig. 3.11 can be fitted with the power law

$$E_{\text{THz}}^{\text{max}}(\lambda) \sim \lambda^{1.28}. \quad (110)$$

This agrees well with the estimate for the magnitude of the initial current  $|\mathbf{j}| \sim A_0 \sim \lambda$  [153].

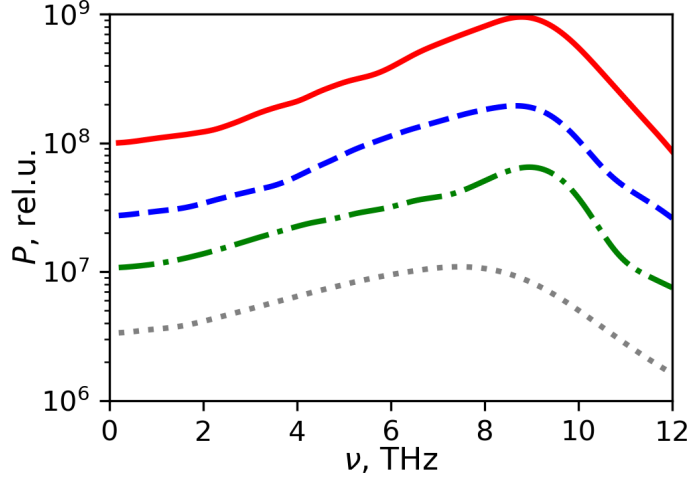


**Figure 3.12: Relative spectral density of the radiated power computed according to Eq. (111) for argon under 200 mbar pressure irradiated by a two-color laser field of intensity  $3 \cdot 10^{14}$  W/cm<sup>2</sup> with the main component's wavelength being equal to 800 nm (dotted grey line), 1.6  $\mu$ m (dash-dotted green), 2.4  $\mu$ m (dashed blue) or 4.0  $\mu$ m (red solid). Adapted from [169]. © 2018 by the American Physical Society.**

Next, the relative spectral power of the radiation is estimated by considering the Fourier transform of the dipole (109) and squaring its modulus,

$$P(\nu) \sim |\ddot{d}_x(\nu)|^2, \quad \ddot{d}_x(\nu) = \int_0^\infty \ddot{d}_x(t) e^{-i2\pi\nu t} dt. \quad (111)$$

The result for various wavelengths is shown in Fig. 3.12 and provides two main outcomes. Firstly, for various values of the laser wavelength  $\lambda$ , oscillations at the local plasma frequency (108) result in a relatively broad spectrum of radiation, maximized around  $\nu^{\max}$ . In the high-frequency region ( $\nu > \nu^{\max}$ ) the emission is noticeably weaker while for  $\nu < \nu^{\max}$  the decay with decreasing frequency is not that abrupt due to contributions from the edges of the plasma volume. Collisional energy losses lead to an additional decay of the oscillations and, as a result, in broadening of the frequency spectrum, especially for smaller wavelengths where the initial momentum spread  $\Delta k$  is narrower and the effective temperature  $T_{\text{eff}}$  is lower (see Fig. 3.8). As known from previous works [125, 131, 170, 184, 191–195], a commonly applied 800 nm laser field generates a plasma cloud that produces an almost single-cycle THz burst. The total dipole of a plasma induced by a longer wavelength survives at least for few more oscillations. This causes the total emitted energy  $W$  to increase with the wavelength in addition to the squared laser-related scaling (110). The value of  $W$  can be calculated by integrating (111) over the frequency range  $\Delta\nu = 0.1 \div 10$  THz. This quantity is shown in Fig. 3.13 as a function of wavelength of the laser. The wavelength dependence can be fitted with the power law

$$W(\lambda) \sim \lambda^{2.8}, \quad (112)$$

which slightly surpasses the squared (110) law. Such a scaling is in well understood from

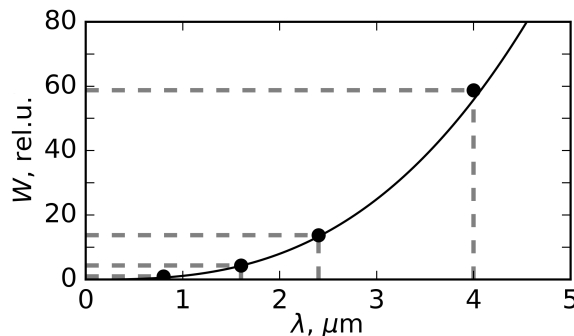


**Figure 3.13:** Total energy emitted in frequency range  $\Delta\nu = 0.1 \div 10$  THz as a function of wavelength of the main component of the two-color laser pulse. The black line indicates the power law fitting according to Eq. (112). Reprinted from [169]. © 2018 by the American Physical Society.

the following simple estimate. The total emitted energy is proportional to the square of the electric field strength (110) and to the THz pulse duration, which grows with increasing laser wavelength due to the reduction of the effective collisional frequency (105). If the gaseous target was not restricted to a small volume, an additional  $\lambda^2$  multiplier would appear in (112) due to the  $w_0 \sim \lambda$  dependence of the beam waist on the wavelength (if the same optical lens would be used for various wavelengths of the laser pulse). In that case, the joint contribution of all  $\lambda$ -dependencies finally leads to an increase of the total energy emitted in the THz domain with increasing laser wavelength according to a  $W(\lambda) \sim \lambda^{4.8}$  power law. This scaling is in good agreement with the experimentally observed power law  $\lambda^{4.6 \pm 0.5}$  [153].

At this point, several remarks on the limitations on the increase of the THz power should be made. First of all, in the case when the laser interacts with the gas that is located inside a large chamber or when it simply interacts with the ambient air, plasma filaments with the length of few centimeters or even few dozens centimeters can be created [196–199]. To describe such an experiment correctly, one would need to account for the propagation of the THz signal as well as the propagation of the ionizing laser pulse. Interestingly, at specific conditions the step of propagation in the plasma channel may also cause amplification of the THz or sub-THz pulses accompanied by narrowing of its frequency spectrum [200, 201]. Oppositely, in [172] a 100  $\mu\text{m}$ -long tube filled with gas was used, and the dependence of the THz power on the backup pressure in the range below 70 mbar was observed to be quadratic, which implies that the plasma emits coherently when the interaction region is restricted down to a small volume. Also, a significantly higher efficiency of the THz output power per unit electron in a tightly confined space has been theoretically predicted in [195]. Secondly, it should be noted that using the same optical lens would result in weaker focusing for longer wavelengths, thus reducing the peak intensity of the laser beam and, eventually, the output THz power [153]. This gives an additional complication for conducting comparative experiments with the same intensity profile. Thirdly, it should be noted that at high velocities of photoelectrons the inelastic collisions with atoms start playing a more significant role, resulting in a faster decay of the residual current. This,

eventually, raises the complexity of the required modelling.

### 3.5 CONCLUSIONS OF CHAPTER 3

- THz radiation resulting from ionization of argon gas by a two-color intense laser field with colinearly polarized components of wavelengths 800 nm and 400 nm is optimized at an intensity of the main component  $I \approx (1 \div 2) \cdot 10^{14}$  W/cm<sup>2</sup> and  $2\xi = E_2/E_1 \approx 0.5 \div 1$  (i.e., at similar intensities).
- Due to the  $2\omega$  component of the laser field being more efficient for ionization, the regime in which the  $\omega$  component of the laser pulse plays the role of a perturbation is reached already at small values of  $\xi$  ( $\xi \simeq 0.1$  for the particular setup from Fig. 3.3). Nevertheless, in such cases the main component still strongly modifies the net photoelectron current although it already weakly affects the ionization dynamics. In the limiting case of  $1/\xi \ll 1$  a purely linear scaling with  $E_1$  is reached [126, 128, 130].
- The optimal polarizations in the  $\omega$ - $2\omega$  two-color laser are circular  $\circ\circ$ . Besides being remarkably superior compared to  $\uparrow\uparrow$  pulses in terms of the net photoelectron current, the  $\circ\circ$  scheme is also advantageous against  $\circ\uparrow$  configurations because the output power does not depend on the relative phase  $\phi$  between the components of the laser.
- Substantially non-linear THz radiation power amplification  $W(\lambda) \sim \lambda^{4.8}$  is achieved when wavelengths  $\lambda$  and  $\lambda/2$  higher than commonly applied 800 nm and 400 nm are considered. Such a scaling is in good agreement with the one observed in [153].

## CHAPTER 4

# TIME-ENERGY ANALYSIS OF PHOTOELECTRON QUANTUM DYNAMICS

In the present Section the sub-laser-cycle time-resolved analysis of the evolution of quantum processes is addressed. In particular, observables that can be represented with the help of integrals over time,

$$P(\Omega) = \left| \int dt \langle a_\Omega(t) \rangle \right|^2, \quad (113)$$

are examined. Inserting a short-time-limited function (called a time window) into the integrand, one may perform a fruitful analysis of the frequencies that are most pronounced in the vicinity of a certain moment in time and gain useful auxiliary knowledge about the sub-cycle dynamics of the system. In practice, the simplest and commonly used window is Gaussian:

$$w_G(t - t_0) = \frac{1}{\sqrt{2\pi t_w^2}} e^{-(t-t_0)^2/2t_w^2}. \quad (114)$$

Such a way of analysis is nowadays an insightful tool in the research related to the HHG [84, 202–211]. The process of HHG is commonly described on the semiclassical level assuming the validity of the Larmor formula

$$P(\Omega) \sim |\ddot{\mathbf{r}}(\Omega)|^2 \quad (115)$$

for the dipole radiation from charged particles moving with an acceleration  $\ddot{\mathbf{r}}(t)$ . Here,

$$\ddot{\mathbf{r}}(\Omega) = \int dt \ddot{\mathbf{r}}(t) e^{-i\Omega t} \quad (116)$$

is the Fourier transform of the acceleration. An example for a HHG spectrum is shown in Fig. 4.1. Setting the time width  $t_w$  equal to a small fraction of an optical period of the central laser frequency  $\omega$  (typically  $t_w \sim (0.1 - 0.3) \cdot 2\pi/\omega$ ) one may visualize the energy spectrum of photon emission caused by the electron-ion recombination process at sub-laser-cycle timescale and identify the dominating times around which photons of a certain frequency are emitted. The quantity

$$P(t_0, \Omega) = \left| \int \frac{dt}{\sqrt{2\pi t_w^2}} \langle a_\Omega(t) \rangle e^{-(t-t_0)^2/2t_w^2} \right|^2 \quad (117)$$

is called the (modulus-squared) Gabor transform of  $P(\Omega)$ . According to the classical scenario of HHG called the three-step model [123, 124], the contribution to high-energy photon emission occurs twice per laser cycle, mainly in the vicinity of times when the electric field reaches zero, forming a sequence of high-energy photon bursts, the so-called

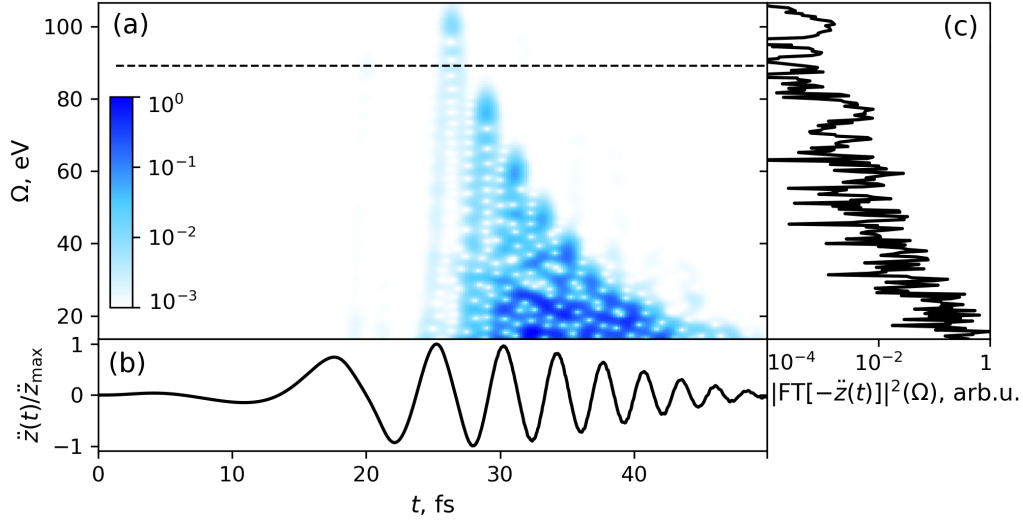


**Figure 4.1:** (a) Gabor-transformed spectrum of HHG computed according to Eq. (117) with  $t_w = 0.1 \cdot 2\pi/\omega$ . Laser intensity is equal to  $I = 10^{14}$  W/cm<sup>2</sup> and central wavelength  $\lambda = 1600$  nm. (b) Dipole acceleration. Its shape is built from the temporal profile of the laser electric field and the high-frequency oscillations from HHG process. (c) The total spectrum of HHG. Horizontal dashed line in (a) indicates the classical cutoff  $\Omega_{\max} = I_p + 3.17U_p$  [124, 214]. The data are normalized to their maxima.

‘attosecond train’ [212]. Based on this knowledge, a variety of techniques to control and optimize the emitted XUV light have been introduced. In Fig. 4.1, results of a calculation based on the numerical solution to the TDSE confirming this classical picture are shown for a chirped pulse (see, e.g., [213] for the short-time Fourier transform applied to HHG in chirped pulses).

Besides the process of HHG, another physical observable, the momentum-resolved PES, is of central interest for optimization of various experiments involving laser-matter interaction as was highlighted in previous chapters of the present thesis. Below this formalism is extended to the numerical study of the PES.

## 4.1 TIME-OF-FLIGHT ANALYSIS OF PES

Part of the results shown below are published in [215].

In modern research devoted to characterisation of the momentum distributions of the laser-driven photoelectrons, ‘numerical solutions to the TDSE’ are commonly strongly associated with final (i.e., time-integrated) PES. Such spectra can be compared to those measured in experiments. The same time, a deeper analysis is often performed by comparing the TDSE-based spectra to the ones produced from simplified theories, in which a PES can be disentangled into pieces of different origin. One of the efficient state-of-the-art methods to retrieve a laser-induced PES from a numerical solution to the TDSE is tSURFF, described in Section 1.3.3. In tSURFF, The amplitude of photoionization is represented as a flux through a certain surface  $S$ , integrated over the registration time  $t$

(see Eq. (53)):

$$a_{\mathbf{k}} = \int_0^\infty dt \partial_t a_{\mathbf{k}}(t) = \int_0^\infty dt \int_S d\mathbf{S} \mathbf{j}_{\mathbf{k}}(\mathbf{r}, t). \quad (118)$$

A comparison of the expression

$$Y(\mathbf{k}) = \left| \int_0^\infty dt \partial_t a_{\mathbf{k}}(t) \right|^2 \quad (119)$$

for the PES with Eq. (113) suggests that one may inherit the benefits of the short-time Fourier analysis, which was introduced above in the context of HHG. Applying a Gaussian window of sub-laser-cycle width to the integrand in (119) gives

$$\partial_t \tilde{a}_{\mathbf{k}}(t_0) = \int_0^T \frac{dt}{\sqrt{2\pi t_w^2}} \partial_t a_{\mathbf{k}}(t) e^{-\frac{(t-t_0)^2}{2t_w^2}}, \quad (120)$$

which coincides with the zero-frequency component of the Gabor transform. This method is further referred to as the time-of-flight (TOF) method. Importantly, the transform (120) keeps the total amplitude and the yield conserved, as integration over  $t_0$  recovers (118), and

$$\tilde{Y}(\mathbf{k}) = \left| \int_{-\infty}^\infty dt_0 \left( \int_0^T \frac{dt}{\sqrt{2\pi t_w^2}} \partial_t a_{\mathbf{k}}(t) e^{-\frac{(t-t_0)^2}{2t_w^2}} \right) \right|^2 = Y(\mathbf{k}). \quad (121)$$

In practise, a smooth time window is usually applied at times approaching  $T$  to suppress the effects of its finiteness. If this is the case, the flux is zero close and beyond the limits  $t_0 = 0$  and  $t_0 = T$ , which enables a safe replacement of the limits  $\pm\infty$  for  $t_0$  in (121) by 0 and  $T$ .

In the example shown in Fig. 4.2, a time window of width  $\omega t_w = 0.2\pi$ , i.e., a tenth of a laser cycle, is taken. This ensures that only intracycle interference are captured at such subcycle time resolution. Interestingly, this reveals a number of discrete portions of electrons being registered. The arrival of the last portion of the flux coincides well with the classical estimate (55)

$$T = T_p + \frac{R}{k_{\min}} \quad (122)$$

for the time  $T$  required to capture the signal from electrons with momentum bigger than  $k_{\min}$ . Furthermore, other discrete portions are also well fitted by a general expression for classical trajectories:

$$\mathbf{R} = \int_{t_i}^{t_{\text{reg}}} dt' \mathbf{A}(t') + \mathbf{k}(t_{\text{reg}} - t_i). \quad (123)$$

Here,  $t_i$  is the initial moment when the electron has gained its canonical momentum  $\mathbf{k}$  and  $t_{\text{reg}}$  is the time when this electron reaches the sphere located at distance  $R$  from the residual ion. At energies  $E_k < (2 \div 4)U_p$  the yield is mainly represented by ‘direct’ electrons. According to the SMM (see Section 1.2.1), the probability of ionization is the highest in the vicinity of the times when the electric field  $|\mathbf{E}(t)|$  peaks. At higher energies  $E_k < 10U_p$  the signal is formed by scattered electrons. Those obtain their final canonical momentum  $k$  after scattering, and the highest  $k$  values correspond to times when the vector potential  $|\mathbf{A}(t)|$  peaks (here, only first-order returns are considered), i.e., when  $|\mathbf{E}(t)|$  reaches zero

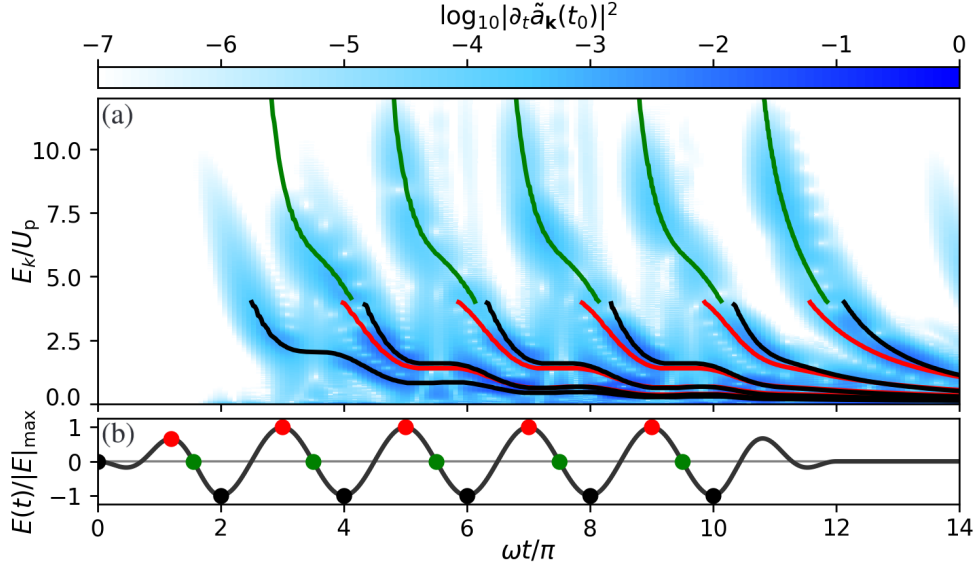


**Figure 4.2:** (a) Time-energy-resolved PES from argon in the laser propagation direction computed according to Eq. (120). The data are normalized to their maxima. Laser intensity is equal to  $I = 10^{13}$  W/cm<sup>2</sup> and wavelength  $\lambda = 2000$ nm. Flux-capturing surface is set at  $R = 350$  a.u. For electrons that originate from times  $t_i$  when  $|E(t_i)| = E_{\max}$  and that have energies  $E_k < 4U_p$ , the arrival times  $t_{\text{reg}}$  according to (123) are indicated by red and black lines; for those that originate from times  $t_i$  when  $E(t_i) = 0$  and that have energies  $E_k > 4U_p$  the arrival times are indicated by green lines. (b) Laser field strength  $E(t)$  with points referring to colored lines in (a). Adapted from [215].

in the case of a linearly polarized pulse [39]. Inverting Eq. (123) to  $t_0 = t_{\text{reg}}(\mathbf{k}, t_i)$ , solving for  $t_i$  that fulfills  $E(t_i) = 0$  or  $A(t_i) = 0$  and drawing the solutions over the density plot in Fig. 4.2, one finds a fairly good agreement.

#### 4.1.1 TIME-OF-FLIGHT DESCRIPTION OF THE ATTOCLOCK

The time-of-flight analysis just introduced is not restricted to linear polarization. Consider the problem of ionization by the strong field described via

$$\mathbf{A}(t) = A_0(t) \begin{pmatrix} \sin(\omega t) \\ \epsilon \cos(\omega t) \end{pmatrix} \quad (124)$$

with highly elliptical polarization ( $\epsilon = 0.882$ ). This and other parameters are chosen to match those from [216, 217]: intensity  $I = 10^{14}$  W/cm<sup>2</sup>, wavelength  $\lambda = 800$ nm. Under such conditions the ionization probability is exponentially damped for non-zero momentum components in the laser propagation direction,  $k_z$ . Taking into account that the visualization of functions dependent on more than two variables is inconvenient, the application of the TOF method to the angle-resolved PES will be demonstrated below with averaging over the radial momentum axis,  $k_r = \sqrt{k_x^2 + k_y^2} \equiv k$  and with restriction to the polarization plane only (i.e., to  $k_z = 0$ ):

$$Y(k_z = 0, \alpha, t) = \int dk \, k \left| \int_0^t dt_0 \, \partial_t \tilde{a}_{\mathbf{k}}(t_0) \right|^2. \quad (125)$$

Photoelectrons emission is expected to be strongly enhanced twice per optical cycle in the vicinity of times  $t_A$  when the electric field  $|\mathbf{E}(t)|$  peaks. The directions of emission  $\alpha$  are along the negative vector potential

$$-\mathbf{A}(t_A) = |\mathbf{A}(t_A)| \begin{pmatrix} \cos \alpha \\ \sin \alpha \end{pmatrix} \quad (126)$$

giving the two opposite values close to  $\alpha \sim \pm\pi/2$ . Let the envelope  $A_0(t)$  be of the ‘1-4-1’ form (i.e., having a 4-cycle flat-top middle part and 1-cycle rampings at edges, as in Fig. 4.2(b)). Local extrema of the ionization rate should then be observed within the central four cycles only. In Fig. 4.3, the angular PES (125) as a function of maximal registration time  $t$  is shown. The average momentum at those angles is

$$\langle k(\alpha) \rangle = \frac{\int dk k^2 Y(k, \alpha)}{\int dk k Y(k, \alpha)} \simeq 0.8 \text{ a.u.} \quad (127)$$

Setting the flux-capturing surface at  $R = 200$  a.u. predicts the flux of electrons emitted in the direction  $\alpha$  to reach this surface predominantly around times

$$t = t_A(\alpha) + \frac{R}{\langle k(\alpha) \rangle} \sim t_A + 2.5 \cdot 2\pi/\omega. \quad (128)$$

This simple estimate is in good agreement with the results displayed in Fig. 4.3(c,d) for a short-range binding potential. However, for a Coulomb potential this agreement breaks (see Figs. 4.3(a,b)) and a shift of about

$$\omega\Delta t = -\Delta\phi \sim 0.12\pi \quad (129)$$

is observed (see also Fig. 4.4). Thus, **the TOF analysis sorts out in detail the effect of angular shift of the PES in highly elliptical laser fields, which makes it useful for the description of the so-called ‘attoclock’ experiments [218–221]** that aim at mapping of registration-, ionization- or tunneling-time delays to this shift.

A remark on the alternative approach proposed in [216, 217] should be given at this point. In these articles, the time-resolved formation of the PES is addressed by constructing the ‘Wigner-distribution-like’ function. Although giving a quasiprobability function (meaning that this distribution is in general not positive-definite) and allowing for peculiar artifacts (see, e.g., [222–224] and discussion in [217]), it provides a useful tool for zooming into the subcycle electron ionization dynamics predicted within the SFA-based calculations. In the particular example considered above in the present thesis the TOF analysis of the TDSE-based simulation gives a fairly good agreement with it.

#### 4.1.2 FORMATION OF THE QUANTUM INTERFERENCE STRUCTURE

After demonstrating the benefit of the short-time Fourier analysis together with the tSURFF method it is time to pass the baton to its extension iSURFV (see Section 1.3.4). Recently, a way to visualize the formation of intercycle interference patterns and of the rescattering plateau was proposed [225]. The idea is based on the fact that at times  $t_E$  that corre-

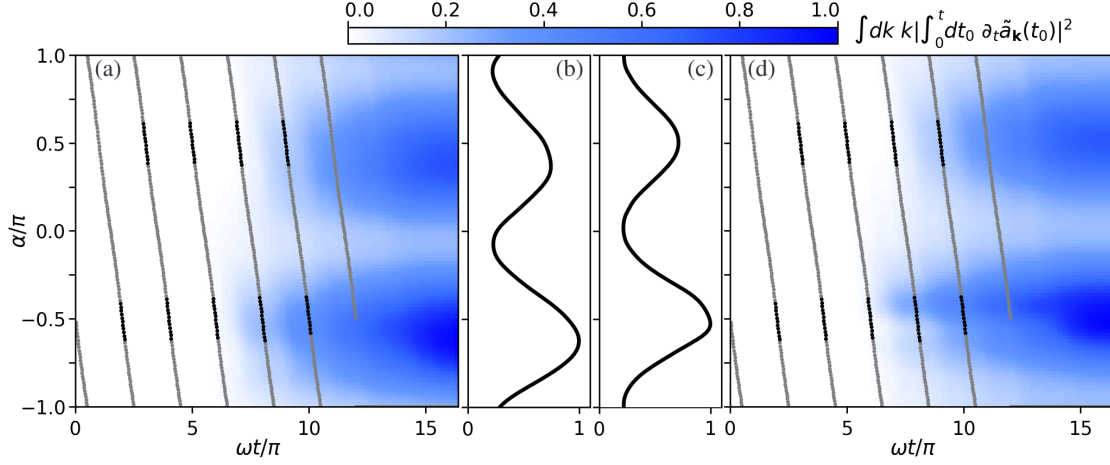


**Figure 4.3: (a,d) Cumulative yield as a function of maximal registration time  $t$  calculated according to Eq. (125) and plotted vs emission angle  $\alpha$ .** Laser intensity  $I = 10^{14} \text{W/cm}^2$ , wavelength  $\lambda = 800 \text{nm}$ , ellipticity  $\epsilon = 0.882$ . Flux-capturing surface is set at  $R = 200$  a.u. Gray lines show angles of  $-\mathbf{A}(t)$ , black lines on top of them – angles where  $|\mathbf{E}(t)| > 0.986 E_{\text{max}}$ . (b,c) Total angular distributions, i.e., sections through  $t = T$  of (a,d). (a,b) show results for hydrogen, (c,d) for short-range potential with same ionization potential  $I_p = 13.6 \text{eV}$ . Data in each subplot are normalized to their maxima. Adapted from [215].

spond to nodes of the laser field strength ( $\mathbf{E}(t_E) = 0$ ) the Hamiltonian becomes equal to the laser-free one (in [225] the length gauge was adapted). By projecting out the bound part  $|\psi_{\text{bound}}(t_E)\rangle$  from the total wavefunction  $|\Psi(t_E)\rangle$  one may calculate the momentum distribution of free electrons that would correspond to the ionization by a laser pulse that is suddenly shut down at  $t_E$ . Transferring this recipe to the velocity gauge, one may evaluate the spectrum at times  $t_A$  where  $\mathbf{A}(t_A) = 0$ . Once  $|\Psi(t_A)\rangle$  is obtained, the vector potential can be turned off at subsequent times ( $\mathbf{A}(t > t_A) = 0$ ), giving green light to the application of the iSURFV method, which efficiently computes the contribution to the PES from a field-free propagation dictated by a time-independent Hamiltonian  $\hat{H}_0$  [51–53]. The resulting partial amplitude of the PES is defined according to Eqs. (56,59,60), apart

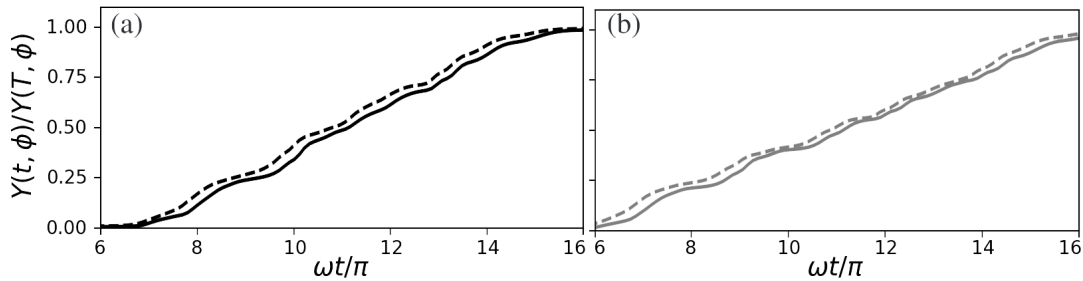


**Figure 4.4: A section through the time and angle resolved distributions shown in Fig. 4.3(a,d) along angles  $\alpha$  where the yield reaches local maxima, i.e.,  $\alpha = -0.616\pi$  (solid black) and  $\alpha = 0.373\pi$  (solid gray) for hydrogen,  $\alpha = -0.495\pi$  (dashed black) and  $\alpha = 0.495\pi$  (dashed gray) for short-range potential.** Data for each curve are normalized to their maxima. Adapted from [215].

from  $T_p$  being now replaced by  $t_A$ :

$$a_{\mathbf{k}}^{(\infty)}(t_A) = a_{\mathbf{k}}(t_A) + \delta a_{\mathbf{k}}^{(\infty)}(t_A), \quad (130)$$

$$\delta a_{\mathbf{k}}^{(\infty)}(t_A) = \int_{S_R} d\mathbf{S}_{\mathbf{r}} \mathbf{J}_{\mathbf{k}}^{(\infty)}(\mathbf{r}, t_A). \quad (131)$$

The processes of formation of the intercycle interference and the rescattering plateau are shown in Fig. 4.5 by a set of snapshots of the PES. Notwithstanding that such intermediate spectra are gauge-dependent, as is the discrete set of time instants when they are evaluated (e.g.,  $t_E$  for the length gauge are  $\pi/2\omega$ -shifted against  $t_A$  for the velocity gauge), they still may act as a good mediator between the fully numerical results and those calculated within approximate semi-analytical methods. For example, as was discussed in Section 1.2, in the SFA-based theories the amplitude  $a_{\mathbf{k}}^{\text{SFA}}(T)$  of the PES is also represented via an integral over time, which can be evaluated using the saddle-point method (see Section 1.2.2),

$$a_{\mathbf{k}}^{\text{SFA}}(T) = \sum_{\text{Re } t_s < T} M_{\mathbf{k}}(t_s), \quad (132)$$

where the saddle points can be interpreted as the complex ionization times  $t_s$  that contribute predominantly. Restricting the ionization times in the summation in (132) to those that have  $\text{Re } t_s < t_A$  (or  $\text{Re } t_s < t_E$  in the length gauge) reveals the build-up of the PES [39, 226–228] that is similar to the above-described sudden termination of the laser in the TDSE simulations.

#### 4.1.3 REMOVING THE QUANTUM INTERFERENCE PATTERN FROM THE PES OBTAINED WITH NUMERICAL SOLUTIONS TO THE TDSE

In most SFA-based examples demonstrated in the present thesis the interference between various saddle points contributing to the amplitude of the PES has been neglected. This can be achieved by replacing the squared modulus of the sum over the saddle points (see Eq. (24)) by the squared sum of the moduli,

$$Y_{\text{abs}}^{\text{SFA}}(\mathbf{k}) = \left( \sum_s |M_{\mathbf{k}}(t_s)| \right)^2. \quad (133)$$

In principle, using instead a sum over squared moduli (i.e., removing the interference patterns rather than replacing them all by constructive interference) is a better choice, as it lets the total rate grow linearly with the increase of the pulse duration, but for the sake of introducing a way to directly compare the TDSE-based calculations with the SFA-based ones, formula (133) will be adapted. The type of interference playing a primary role in ionization by long intense pulses is that between the signals from subsequent optical cycles (ATI-peak pattern defined according Eq. (22)). Removing it greatly simplifies the observed spectra revealing their main shape that otherwise may be obscured (see, e.g., [87, 228]). Interestingly, once the PES is accurately resolved, application of the Fourier transform with subsequent low-pass filtering and reverse transformation may successfully remove

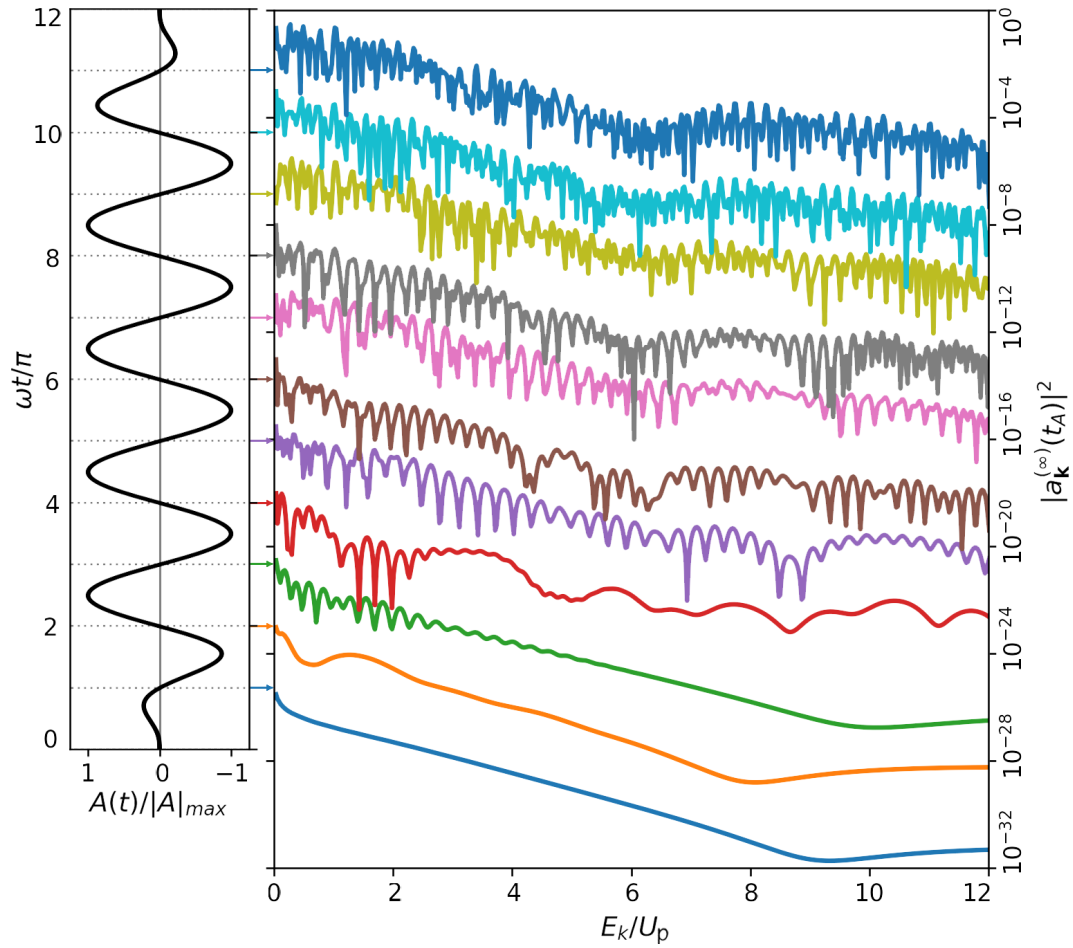


**Figure 4.5:** (a) Vector potential  $A(t)$ . (b) Time-energy-resolved photoelectron spectrum from argon in laser polarization direction with the laser vector potential suddenly switched off at times when it reaches zero. Spectra were calculated using the amplitude (130). Results are shifted along the vertical axis for better visualization. Laser wavelength  $\lambda = 800\text{nm}$ , intensity  $I = 10^{14}\text{W/cm}^2$ . Adapted from [215].

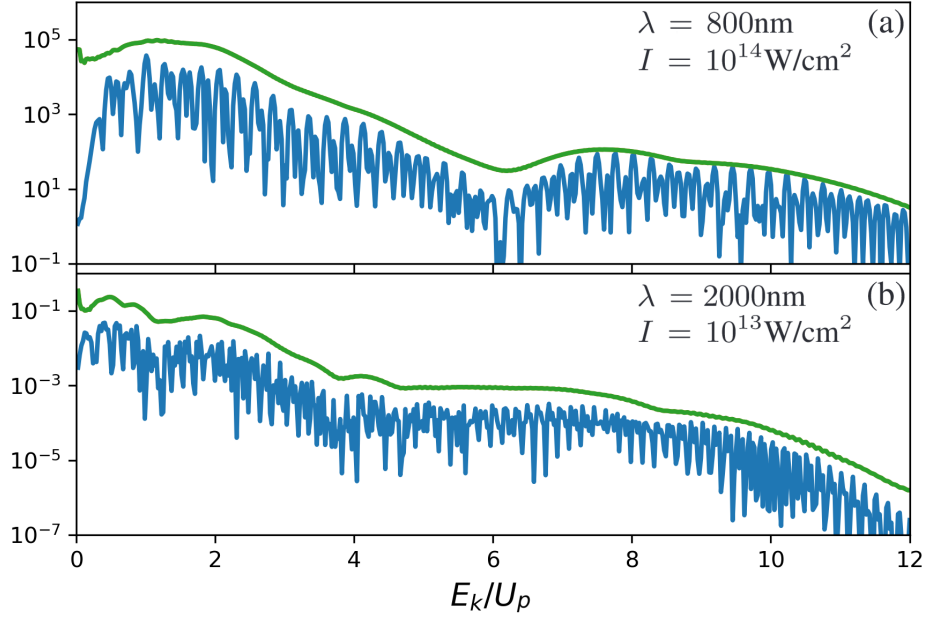


**Figure 4.6: Demonstration of elimination of long-timescale interference patterns from PES.** The spectra are calculated for argon according to Eq. (121) (blue) and according to Eq. (134) (green). Laser pulses with a ‘1-4-1’ envelope (see text) were used in both examples with (a)  $\lambda = 800\text{nm}$  at  $I = 10^{14}\text{W/cm}^2$  ( $U_p = 3.85\omega$ ) and (b)  $\lambda = 2000\text{nm}$  at  $I = 10^{13}\text{W/cm}^2$  ( $U_p = 6.02\omega$ ). A gap at low energies (mostly pronounced in (a)) is due to the finite upper time limit  $T = T_p + 500$  a.u. in the application of tSURFF. Reprinted from [215].

the ATI-peaks pattern [229] regardless what is the nature of the original spectrum — an experimental measurement or a calculation. However, the total number  $E_k^{\text{max}}/\omega$  of such peaks in the PES scales with the intensity  $I$  and the wavelength  $\lambda$  of the laser pulse as  $\sim I\lambda^3$  (since the maximal energy  $E_k^{\text{max}}$  is about  $\sim 10U_p$  and the ponderomotive energy  $U_p$  scales as  $\sim I\lambda^2$ ). For intensities  $I \gtrsim 10^{14}\text{ W/cm}^2$  and wavelengths  $\lambda \gtrsim 2\mu\text{m}$ , unfortunately, this number easily exceeds one or few hundreds, unavoidably requiring a tinier and tinier energy grid to be captured. And while in the experimental case this does not become a big issue since this pattern is simply washed out due to the non-homogeneous intensity distribution, the computational cost to calculate PES generally scales linearly with the total number of energy bins in it. At this point, **the way to effectively subtract the ATI-peaks pattern based on the TOF analysis of the PES can be established by using the modulus of the time-averaged integrand in Eq. (120), giving**

$$\tilde{Y}_{\text{abs}}(\mathbf{k}) = \left( \int_0^T dt_0 \left| \int_0^T \frac{dt}{\sqrt{2\pi t_w^2}} \partial_t a_{\mathbf{k}}(t) e^{-\frac{(t-t_0)^2}{2t_w^2}} \right| \right)^2. \quad (134)$$

Figure 4.6 shows the PES calculated with Eqs. (120) and (134). Application of the latter successfully removes the pattern of the ATI peaks, as desired.

A remark concerning the comparison with the SFA should be made: since in the SFA the time integral (or the sum over saddle points) is taken over the ionization, not the

registration time, Eq. (133) does not directly match with Eq. (134) where integration over registration times is performed instead. Nevertheless, both ‘tricks’ effectively remove the pattern of the ATI peaks from the PES.

## 4.2 CONCLUSIONS OF CHAPTER 4

- The formation of the PES from atoms in strong laser fields is analysed with respect to the time of registration of the electron signal (TOF analysis). Using the state-of-the-art numerical methods for calculating PES (the tSURFF and iSURFV methods), the PES are acquired directly from the numerical solutions to the TDSE. In the obtained TOF-dependent spectra, the characteristic semiclassical fingerprints are identified, thus, making the semiclassical description applicable to the time-resolved PES and not only to the final, time-integrated ones.
- The TOF analysis is shown to be suitable for a description of the formation not only of the energy-resolved but also of the angular-resolved spectrum. A particular example of the ionization by a highly elliptical pulse demonstrates the TOF to be useful for the analysis of 'attoclock' experiments.
- Using the structure of the TOF spectrum, a possibility of removing the highly oscillating pattern of the ATI peaks from the total PES is demonstrated. Importantly, with this method, the resolution of the momentum grid no longer requires to be tinier than the width of the ATI peaks in order to ensure that the momentum bins do not accidentally coincide with the nodes of the spectrum.

## CONCLUSIONS AND OUTLOOK

In this thesis, various aspects of the mechanism of interaction of strong laser fields with gaseous matter have been addressed, and specific applications of the related processes have been considered.

In Chapter 2, the Phase-of-the-phase (PoP) technique – a method of characterizing the photoelectron spectra (PES) in two-color fields based on the Fourier decomposition of those with respect to the phase shift between the components – was addressed and an extension of that to the case of counter-rotating circularly polarized ( $\odot\odot$ ) fields was introduced. It was proved analytically that the terms of the Fourier decomposition can be factorized into parts that depend on either the angle of emission or on the energy of the photoelectron. The latter dependence manifests in the phases  $\Phi_n$  of those terms, the PoP, only in a form of sharp flips of their value. Using the sharpness of these flips together with their location being sensitive to the laser and target parameters, a method of calibrating the intensity in focus of a laser was proposed. Next, as the Fourier decomposition in the PoP technique is performed with respect to the relative phase between the components of a two-color field, the Fourier terms of non-zero order should only originate from the laser-coherent part of the total PES. Thus, applying the PoP analysis to a PES containing some laser-incoherent contribution should ensure no influence of the latter when non-zero Fourier terms are addressed. Based on that, a way to reveal the weak laser-coherent signal from an incoherent-dominated PES was demonstrated. Such treatment is, therefore, advantageous for the analysis of PES produced from complex systems.

In Chapter 3, a different application of two-color fields was addressed. Provided specific conditions are fulfilled, they may efficiently generate a PES with a well-pronounced preferable direction of emission, creating a significantly strong residual photoelectron current that lives long after the laser pulse. Oscillatory movement of the photoelectron plasma causes radiation at characteristic plasma frequencies (that are much smaller than that of the laser) resulting, thus, in a mechanism of frequency conversion and creating a plasma-based source of THz radiation. In the present thesis, a number of optimizations of the two-color field configurations were proposed, aiming at maximizing the residual current in a plasma and, correspondingly, maximizing the output power of radiation in the THz frequency domain. Firstly, a commonly used scheme with  $\Updownarrow\Updownarrow$  polarizations is shown to be most efficient at intensities of the laser components being relatively close. The experimental realization of such a setup is difficult, therefore alternative configurations are studied further: based on simplistic estimates, a  $\odot\Updownarrow$  or a  $\odot\odot$  field is supposed to be more efficient than  $\Updownarrow\Updownarrow$  at low intensities of the second component of the laser. This assumption, justified by previous experimental observations for the  $\odot\odot$  case, is validated in the thesis by computations based on the strong-field approximation and on the fully numerical approach. Importantly, arguments for the  $\odot\odot$  configuration being the optimal choice are provided. Lastly, the commonly applied laser frequencies are 800 and 400 nm (Ti:sapphire laser) while the laser fields of longer wavelengths should produce higher residual photocurrents.

Thus, it is suggested to combine the application of the MIR lasers together with  $\sigma\sigma$  polarizations. An essentially non-linear dependence of the total energy emitted in the THz domain predicts a drastic increase in the conversion efficiency compared to commonly used setups.

In Chapter 4, a method of characterizing the numerically obtained PES was proposed based on the application of the surface-flux methods of calculating the PES from a solution to the TDSE, combined with the time-of-flight analysis of it. The arising time-resolved PES with time resolution below an optical cycle of a laser were shown to be built of portions of electron flux registered at discrete times well coinciding with the semi-classically predicted. Giving an additional degree of freedom that is commonly integrated out, this allows to compare the numerical ab-initio simulations with the physically transparent semiclassical theories of various degree of analyticity. The new method gives a way to not just identify but ‘crop’ the contributions of various physical mechanisms. Moreover, being initially purely quantum and ab initio, it is applicable also in ionization regimes beyond semiclassical theories, for example over-the-barrier ionization or when the excited states play a significant role.

## REFERENCES

- [1] Keldysh, L. V. Ionization in the field of a strong electromagnetic wave. *Zh. Eksp. Teor. Fiz.* **20**, 1307 (1965).
- [2] Faisal, F. H. M. Multiple absorption of laser photons by atoms. *Journal of Physics B: Atomic and Molecular Physics* **6**, L89 (1973).
- [3] Reiss, H. R. Effect of an intense electromagnetic field on a weakly bound system. *Phys. Rev. A* **22**, 1786–1813 (1980).
- [4] Milošević, D. B., Paulus, G. G., Bauer, D. & Becker, W. Above-threshold ionization by few-cycle pulses. *Journal of Physics B: Atomic, Molecular and Optical Physics* **39**, R203 (2006).
- [5] Milošević, D. B., Bauer, D. & Becker, W. Quantum-orbit theory of high-order atomic processes in intense laser fields. *J. Mod. Opt.* **53**, 125–134 (2006).
- [6] Popruzhenko, S. V. Keldysh theory of strong field ionization: history, applications, difficulties and perspectives. *Journal of Physics B: Atomic, Molecular and Optical Physics* **47**, 204001 (2014).
- [7] Wolkow, D. M. Über eine Klasse von Lösungen der Diracschen Gleichung. *Zeitschrift für Physik* **94**, 250–260 (1935).
- [8] A. M. Perelomov, V. S. P. & Terentev, M. V. Ionization of atoms in an alternating electric field: II. *Sov. Phys. JETP* **23**, 924 (1966).
- [9] Delone, N. B. & Krainov, V. P. Tunneling and barrier-suppression ionization of atoms and ions in a laser radiation field. *Physics - Uspekhi* **41**, 469–485 (1998).
- [10] Popov, V. S. Tunnel and multiphoton ionization of atoms and ions in a strong laser field (Keldysh theory). *Phys. Usp.* **47**, 855–885 (2004).
- [11] Li, M., Geng, J.-W., Liu, H., Deng, Y., Wu, C., Peng, L.-Y., Gong, Q. & Liu, Y. Classical-quantum correspondence for above-threshold ionization. *Phys. Rev. Lett.* **112**, 113002 (2014).
- [12] Arbó, D. G., Persson, E. & Burgdörfer, J. Time double-slit interferences in strong-field tunneling ionization. *Phys. Rev. A* **74**, 063407 (2006).
- [13] Arbó, D. G., Ishikawa, K. L., Schiessl, K., Persson, E. & Burgdörfer, J. Intracycle and intercycle interferences in above-threshold ionization: The time grating. *Phys. Rev. A* **81**, 021403 (2010).
- [14] Huismans, Y., Gijbetsen, A., Smolkowska, A. S., Jungmann, J. H., Rouzée, A., Logman, P. S. W. M., Lépine, F., Cauchy, C., Zamith, S., Marchenko, T., Bakker,

- J. M., Berden, G., Redlich, B., van der Meer, A. F. G., Ivanov, M. Y., Yan, T.-M., Bauer, D., Smirnova, O. & Vrakking, M. J. J. Scaling laws for photoelectron holography in the midinfrared wavelength regime. *Physical Review Letters* **109**, 013002 (2012).
- [15] Maxwell, A. S., Al-Jawahiry, A., Das, T. & Faria, C. F. d. M. Coulomb-corrected quantum interference in above-threshold ionization: Working towards multitrajectory electron holography. *Phys. Rev. A* **96**, 023420 (2017).
- [16] Dran, M. & Arbó, D. G. Moiré patterns in doubly differential electron-momentum distributions in atomic ionization by mid-infrared lasers. *Phys. Rev. A* **97**, 053406 (2018).
- [17] Shvetsov-Shilovski, N. I. & Lein, M. Effects of the coulomb potential in interference patterns of strong-field holography with photoelectrons. *Physical Review A* **97**, 013411 (2018).
- [18] Ke, Q., Zhou, Y., Tan, J., He, M., Liang, J., Zhao, Y., Li, M. & Lu, P. Two-dimensional photoelectron holography in strong-field tunneling ionization by counter rotating two-color circularly polarized laser pulses. *Optics Express* **27**, 32193 (2019).
- [19] de Morisson Faria, C. F. & Maxwell, A. S. It is all about phases: ultrafast holographic photoelectron imaging. *Reports on Progress in Physics* **83**, 034401 (2020).
- [20] Mandrysz, M., Kübel, M., Zakrzewski, J. & Prauzner-Bechcicki, J. S. Rescattering effects in streaking experiments of strong-field ionization. *Phys. Rev. A* **100**, 063410 (2019).
- [21] Wiese, J., Olivieri, J.-F., Trabatttoni, A., Trippel, S. & Küpper, J. Strong-field photoelectron momentum imaging of OCS at finely resolved incident intensities. *New Journal of Physics* **21**, 083011 (2019).
- [22] Willenberg, B., Maurer, J., Keller, U., Daněk, J., Klaiber, M., Teeny, N., Hatsagortsyan, K. Z. & Keitel, C. H. Holographic interferences in strong-field ionization beyond the dipole approximation: The influence of the peak and focal-volume-averaged laser intensities. *Phys. Rev. A* **100**, 033417 (2019).
- [23] Wiese, J., Onvlee, J., Trippel, S. & Küpper, J. Strong-field ionization of complex molecules. *Phys. Rev. Research* **3**, 013089 (2021).
- [24] Jašarević, A., Hasović, E., Kopold, R., Becker, W. & Milošević, D. B. Application of the saddle-point method to strong-laser-field ionization. *Journal of Physics A: Mathematical and Theoretical* **53**, 125201 (2020).
- [25] Amini, K., Biegert, J., Calegari, F., Chacón, A., Ciappina, M. F., Dauphin, A., Efimov, D. K., de Morisson Faria, C. F., Giergiel, K., Gniewek, P., Landsman, A. S., Lesiuk, M., Mandrysz, M., Maxwell, A. S., Moszyński, R., Ortmann, L., Pérez-Hernández, J. A., Picón, A., Pisanty, E., Prauzner-Bechcicki, J., Sacha, K.,

- Suárez, N., Zaïr, A., Zakrzewski, J. & Lewenstein, M. Symphony on strong field approximation. *Reports on Progress in Physics* **82**, 116001 (2019).
- [26] Barth, I. & Smirnova, O. Nonadiabatic tunneling in circularly polarized laser fields: Physical picture and calculations. *Phys. Rev. A* **84**, 063415 (2011).
- [27] Popruzhenko, S. V. & Tulsy, V. A. Control of terahertz photoelectron currents generated by intense two-color laser radiation interacting with atoms. *Physical Review A* **92**, 033414 (2015).
- [28] Armstrong, G. S. J., Khokhlova, M. A., Labeye, M., Maxwell, A. S., Pisanty, E. & Ruberti, M. Dialogue on analytical and ab initio methods in attoscience. *The European Physical Journal D* **75**, 209 (2021).
- [29] Zhang, Q., Lan, P. & Lu, P. Empirical formula for over-barrier strong-field ionization. *Physical Review A* **90**, 043410 (2014).
- [30] Tong, X. M. & Lin, C. D. Empirical formula for static field ionization rates of atoms and molecules by lasers in the barrier-suppression regime. *Journal of Physics B: Atomic, Molecular and Optical Physics* **38**, 2593–2600 (2005).
- [31] Hart, G. A. & Goodfriend, P. L. Hellmann pseudopotential parameters for atoms with one valence electron. *The Journal of Chemical Physics* **53**, 448–449 (1970).
- [32] Schweizer, W., Faßbinder, P. & González-Férez, R. Model potentials for alkali metal atoms and Li-like ions. *Atomic Data and Nuclear Data Tables* **72**, 33–55 (1999).
- [33] Milošević, M. Z. & Simonović, N. S. Calculations of rates for strong-field ionization of alkali-metal atoms in the quasistatic regime. *Physical Review A* **91**, 023424 (2015).
- [34] Moiseyev, N. Derivations of universal exact complex absorption potentials by the generalized complex coordinate method. *Journal of Physics B: Atomic, Molecular and Optical Physics* **31**, 1431–1441 (1998).
- [35] Scrinzi, A. Infinite-range exterior complex scaling as a perfect absorber in time-dependent problems. *Phys. Rev. A* **81**, 053845 (2010).
- [36] Szeftel, J. Absorbing boundary conditions for one-dimensional nonlinear schrödinger equations. *Numerische Mathematik* **104**, 103–127 (2006).
- [37] Fevens, T. & Jiang, H. Absorbing boundary conditions for the schrödinger equation. *SIAM Journal on Scientific Computing* **21**, 255–282 (1999).
- [38] Antoine, X., Arnold, A., Besse, C., Ehrhardt, M. & Schädle, A. A review of transparent and artificial boundary conditions techniques for linear and nonlinear Schrödinger equations. *Commun. Comput. Phys.* **4**, 729–796 (2008).
- [39] Kopold, R., Becker, W. & Kleber, M. Quantum path analysis of high-order above-threshold ionization. *Optics Communications* **179**, 39–50 (2000).

- [40] Mihailescu, A. A new approach to theoretical investigations of high harmonics generation by means of fs laser interaction with overdense plasma layers. combining particle-in-cell simulations with machine learning. *Journal of Instrumentation* **11**, C12004–C12004 (2016).
- [41] Gherman, A., Kovács, K., Cristea, M. & Toşa, V. Artificial neural network trained to predict high-harmonic flux. *Applied Sciences* **8**, 2106 (2018).
- [42] White, J. & Chang, Z. Attosecond streaking phase retrieval with neural network. *Optics Express* **27**, 4799 (2019).
- [43] Lytova, M., Spanner, M. & Tamblyn, I. Deep learning and high harmonic generation. *arXiv:2012.10328v2* (2021).
- [44] Shvetsov-Shilovski, N. I. & Lein, M. Deep learning for retrieval of the internuclear distance in a molecule from interference patterns in photoelectron momentum distributions. *arXiv:2108.08057v1* (2021).
- [45] Bauer, D. & Koval, P. Qprop: A Schrödinger-solver for intense laser-atom interaction. *Computer Physics Communications* **174**, 396 – 421 (2006).
- [46] Schafer, K. J. & Kulander, K. C. Energy analysis of time-dependent wave functions: Application to above-threshold ionization. *Physical Review A* **42**, 5794–5797 (1990).
- [47] Bauer, D. (ed.) *Computational Strong-Field Quantum Dynamics* (De Gruyter, Berlin / Boston, United States, 2017).
- [48] Fetić, B., Becker, W. & Milošević, D. B. Extracting photoelectron spectra from the time-dependent wave function: Comparison of the projection onto continuum states and window-operator methods. *Phys. Rev. A* **102**, 023101 (2020).
- [49] Mosert, V. & Bauer, D. Photoelectron spectra with Qprop and t-SURFF. *Computer Physics Communications* **207**, 452 – 463 (2016).
- [50] Tao, L. & Scrinzi, A. Photo-electron momentum spectra from minimal volumes: the time-dependent surface flux method. *New Journal of Physics* **14**, 013021 (2012).
- [51] Tulskey, V. & Bauer, D. Qprop with faster calculation of photoelectron spectra. *Computer Physics Communications* **251**, 107098 (2020).
- [52] Serov, V. V., Derbov, V. L., Sergeeva, T. A. & Vinitisky, S. I. Hybrid surface-flux method for extraction of the ionization amplitude from the calculated wave function. *Physical Review A* **88** (2013).
- [53] Morales, F., Bredtmann, T. & Patchkovskii, S. iSURF: a family of infinite-time surface flux methods. *Journal of Physics B: Atomic, Molecular and Optical Physics* **49**, 245001 (2016).
- [54] Manolopoulos, D. E. Derivation and reflection properties of a transmission-free absorbing potential. *The Journal of Chemical Physics* **117**, 9552–9559 (2002).

- [55] Maxwell, A. S., Armstrong, G. S. J., Ciappina, M. F., Pisanty, E., Kang, Y., Brown, A. C., Lewenstein, M. & de Morisson Faria, C. F. Manipulating twisted electrons in strong-field ionization. *Faraday Discussions* **228**, 394–412 (2021).
- [56] Kang, Y., Pisanty, E., Ciappina, M., Lewenstein, M., de Morisson Faria, C. F. & Maxwell, A. S. Conservation laws for electron vortices in strong-field ionisation. *The European Physical Journal D* **75** (2021).
- [57] Bray, A. C., Maxwell, A. S., Y. Kissin, M. R., Ciappina, M. F., Averbukh, V. & Faria, C. F. D. M. Polarization in strong-field ionization of excited helium. *arXiv:2106.05668v1* (2021).
- [58] Boran, Y., Hart, N., Kaya, N., Zhou, J., Kolomenski, A. & Schuessler, H. Energy and angular distributions of electrons from sodium atoms photo-ionized with femtosecond laser pulses. *Journal of Physics B: Atomic, Molecular and Optical Physics* **54**, 145401 (2021).
- [59] Lai, Y. H., Rao, K. S., Liang, J., Wang, X., Guo, C., Yu, W. & Li, W. Resonance-enhanced high harmonic in metal ions driven by elliptically polarized laser pulses. *Optics Letters* **46**, 2372 (2021).
- [60] Wang, C., Li, X., Liu, X., Jie Li, S. Z., Yang, Y., Song, X., Chen, J., Yang, W. & Ding, D. Decoding electron tunnelling delay time by embracing wave-particle duality. *arXiv:2104.06144v1* (2021).
- [61] Morishita, T., Le, A.-T., Chen, Z. & Lin, C. D. Accurate retrieval of structural information from laser-induced photoelectron and high-order harmonic spectra by few-cycle laser pulses. *Physical Review Letters* **100**, 013903 (2008).
- [62] Okunishi, M., Morishita, T., Prümper, G., Shimada, K., Lin, C. D., Watanabe, S. & Ueda, K. Experimental retrieval of target structure information from laser-induced rescattered photoelectron momentum distributions. *Phys. Rev. Lett.* **100**, 143001 (2008).
- [63] Blaga, C. I., Xu, J., DiChiara, A. D., Sistrunk, E., Zhang, K., Agostini, P., Miller, T. A., DiMauro, L. F. & Lin, C. D. Imaging ultrafast molecular dynamics with laser-induced electron diffraction. *Nature* **483**, 194–197 (2012).
- [64] Xu, J., Blaga, C. I., Zhang, K., Lai, Y. H., Lin, C. D., Miller, T. A., Agostini, P. & DiMauro, L. F. Diffraction using laser-driven broadband electron wave packets. *Nature Communications* **5**, 4635 (2014).
- [65] Peng, L.-Y., Jiang, W.-C., Geng, J.-W., Xiong, W.-H. & Gong, Q. Tracing and controlling electronic dynamics in atoms and molecules by attosecond pulses. *Physics Reports* **575**, 1–71 (2015).
- [66] Tulskey, V. A., Krebs, B., Tiggesbäumker, J. & Bauer, D. Revealing laser-coherent electron features using phase-of-the-phase spectroscopy. *Journal of Physics B: Atomic, Molecular and Optical Physics* **53**, 074001 (2020).

- [67] Skruszewicz, S., Tiggesbäumker, J., Meiwes-Broer, K.-H., Arbeiter, M., Fennel, T. & Bauer, D. Two-color strong-field photoelectron spectroscopy and the phase of the phase. *Phys. Rev. Lett.* **115**, 043001 (2015).
- [68] Almajid, M. A., Zabel, M., Skruszewicz, S., Tiggesbäumker, J. & Bauer, D. Two-color phase-of-the-phase spectroscopy in the multiphoton regime. *Journal of Physics B: Atomic, Molecular and Optical Physics* **50**, 194001 (2017).
- [69] Beaulieu, S., Comby, A., Clergerie, A., Caillat, J., Descamps, D., Dudovich, N., Fabre, B., Généaux, R., Légaré, F., Petit, S., Pons, B., Porat, G., Ruchon, T., Taïeb, R., Blanchet, V. & Mairesse, Y. Attosecond-resolved photoionization of chiral molecules. *Science* **358**, 1288–1294 (2017).
- [70] Gong, X., Lin, C., He, F., Song, Q., Lin, K., Ji, Q., Zhang, W., Ma, J., Lu, P., Liu, Y., Zeng, H., Yang, W. & Wu, J. Energy-resolved ultrashort delays of photoelectron emission clocked by orthogonal two-color laser fields. *Phys. Rev. Lett.* **118**, 143203 (2017).
- [71] Porat, G., Alon, G., Rozen, S., Pedatzur, O., Krüger, M., Azoury, D., Natan, A., Orenstein, G., Bruner, B. D., Vrakking, M. J. J. & Dudovich, N. Attosecond time-resolved photoelectron holography. *Nature Communications* **9**, 2805 (2018).
- [72] Würzler, D., Eicke, N., Möller, M., Seipt, D., Sayler, A. M., Fritzsche, S., Lein, M. & Paulus, G. G. Velocity map imaging of scattering dynamics in orthogonal two-color fields. *Journal of Physics B: Atomic, Molecular and Optical Physics* **51**, 015001 (2017).
- [73] Tan, J., Li, Y., Zhou, Y., He, M., Chen, Y., Li, M. & Lu, P. Identifying the contributions of multiple-returning recollision orbits in strong-field above-threshold ionization. *Optical and Quantum Electronics* **50**, 57 (2018).
- [74] Han, M., Ge, P., Wang, J., Guo, Z., Fang, Y., Ma, X., Yu, X., Deng, Y., Wörner, H. J., Gong, Q. & Liu, Y. Complete characterization of sub-Coulomb-barrier tunnelling with phase-of-phase attoclock. *Nature Photonics* (2021).
- [75] Tan, J., Xu, S., Han, X., Zhou, Y., Li, M., Cao, W., Zhang, Q. & Lu, P. Resolving and weighing the quantum orbits in strong-field tunneling ionization. *Advanced Photonics* **3**, 035001 (2021).
- [76] Braß, J., Milbradt, R., Villalba-Chávez, S., Paulus, G. G. & Müller, C. Two-color phase-of-the-phase spectroscopy applied to nonperturbative electron-positron pair production in strong oscillating electric fields. *Phys. Rev. A* **101**, 043401 (2020).
- [77] Tulskey, V. A., Almajid, M. A. & Bauer, D. Two-color phase-of-the-phase spectroscopy with circularly polarized laser pulses. *Phys. Rev. A* **98**, 053433 (2018).
- [78] Zharebtsov, S., Süßmann, F., Peltz, C., Plenge, J., Betsch, K. J., Znakovskaya, I., Alnaser, A. S., Johnson, N. G., Kübel, M., Horn, A., Mondes, V., Graf, C., Trushin,

- S. A., Azzeer, A., Vrakking, M. J. J., Paulus, G. G., Krausz, F., Rühl, E., Fennel, T. & Kling, M. F. Carrier-envelope phase-tagged imaging of the controlled electron acceleration from SiO<sub>2</sub> nanospheres in intense few-cycle laser fields. *New Journal of Physics* **14**, 075010 (2012).
- [79] Seiffert, L., Köhn, J., Peltz, C., Kling, M. F. & Fennel, T. Signatures and mechanisms of plasmon-enhanced electron emission from clusters in few-cycle laser fields. *Journal of Physics B: Atomic, Molecular and Optical Physics* **50**, 224001 (2017).
- [80] Gao, C.-Z., Dinh, P. M., Reinhard, P.-G., Suraud, E. & Meier, C. Forward-backward asymmetry of photoemission in C<sub>60</sub> excited by few-cycle laser pulses. *Physical Review A* **95**, 033427 (2017).
- [81] Luo, S., Li, M., Xie, H., Zhang, P., Xu, S., Li, Y., Zhou, Y., Lan, P. & Lu, P. Angular-dependent asymmetries of above-threshold ionization in a two-color laser field. *Physical Review A* **96**, 023417 (2017).
- [82] Kübel, M., Burger, C., Siemering, R., Kling, N. G., Bergues, B., Alnaser, A. S., Ben-Itzhak, I., Moshhammer, R., de Vivie-Riedle, R. & Kling, M. F. Phase- and intensity-dependence of ultrafast dynamics in hydrocarbon molecules in few-cycle laser fields. *Molecular Physics* **115**, 1835–1845 (2017).
- [83] Kübel, M., Arbeiter, M., Burger, C., Kling, N. G., Pischke, T., Moshhammer, R., Fennel, T., Kling, M. F. & Bergues, B. Phase- and intensity-resolved measurements of above threshold ionization by few-cycle pulses. *Journal of Physics B: Atomic, Molecular and Optical Physics* **51**, 134007 (2018).
- [84] Azoury, D., Krüger, M., Orenstein, G., Larsson, H. R., Bauch, S., Bruner, B. D. & Dudovich, N. Self-probing spectroscopy of xuv photo-ionization dynamics in atoms subjected to a strong-field environment. *Nature Communications* **8**, 1453 (2017).
- [85] Zhang, Y., Kellner, P., Adolph, D., Zille, D., Wustelt, P., Würzler, D., Skruszewicz, S., Möller, M., Sayler, A. M. & Paulus, G. G. Single-shot, real-time carrier-envelope phase measurement and tagging based on stereographic above-threshold ionization at short-wave infrared wavelengths. *Optics Letters* **42**, 5150 (2017).
- [86] Eicke, N. & Lein, M. Extracting trajectory information from two-color strong-field ionization. *Journal of Modern Optics* **64**, 981–986 (2017).
- [87] Xie, X., Wang, T., Yu, S. G., Lai, X. Y., Roither, S., Kartashov, D., Baltuška, A., Liu, X. J., Staudte, A. & Kitzler, M. Disentangling intracycle interferences in photoelectron momentum distributions using orthogonal two-color laser fields. *Phys. Rev. Lett.* **119**, 243201 (2017).
- [88] Yu, X., Li, M., Han, M. & Liu, Y. Controlling backward-scattering photoelectron holography by attosecond streaking. *Physical Review A* **98**, 013415 (2018).

- [89] Richter, M., Kunitski, M., Schöffler, M., Jahnke, T., Schmidt, L. P. H., Li, M., Liu, Y. & Dörner, R. Streaking temporal double-slit interference by an orthogonal two-color laser field. *Phys. Rev. Lett.* **114**, 143001 (2015).
- [90] Richter, M., Kunitski, M., Schöffler, M., Jahnke, T., Schmidt, L. P. H. & Dörner, R. Ionization in orthogonal two-color laser fields: Origin and phase dependences of trajectory-resolved coulomb effects. *Physical Review A* **94**, 033416 (2016).
- [91] Mancuso, C. A., Hickstein, D. D., Dorney, K. M., Ellis, J. L., Hasović, E., Knut, R., Grychtol, P., Gentry, C., Gopalakrishnan, M., Zusin, D., Dollar, F. J., Tong, X.-M., Milošević, D. B., Becker, W., Kapteyn, H. C. & Murnane, M. M. Controlling electron-ion rescattering in two-color circularly polarized femtosecond laser fields. *Phys. Rev. A* **93**, 053406 (2016).
- [92] Goreslavski, S. P., Paulus, G. G., Popruzhenko, S. V. & Shvetsov-Shilovski, N. I. Coulomb asymmetry in above-threshold ionization. *Physical Review Letters* **93**, 233002 (2004).
- [93] Torlina, L., Morales, F., Kaushal, J., Ivanov, I., Kheifets, A., Zielinski, A., Scrinzi, A., Muller, H. G., Sukiasyan, S., Ivanov, M. & Smirnova, O. Interpreting attoclock measurements of tunnelling times. *Nature Physics* **11**, 503–508 (2015).
- [94] Krebs, B., Tulskey, V. A., Kazak, L., M. Zabel, D. B. & Tiggesbäumker, J. Phase-of-the-phase electron momentum spectroscopy on single metal atoms in helium nanodroplets. *arxiv.org:2102.08150* (2021).
- [95] Alnaser, A. S., Tong, X. M., Osipov, T., Voss, S., Maharjan, C. M., Shan, B., Chang, Z. & Cocke, C. L. Laser-peak-intensity calibration using recoil-ion momentum imaging. *Phys. Rev. A* **70**, 023413 (2004).
- [96] Smeenk, C., Salvail, J. Z., Arissian, L., Corkum, P. B., Hebeisen, C. T. & Staudte, A. Precise in-situ measurement of laser pulse intensity using strong field ionization. *Optics Express* **19**, 9336 (2011).
- [97] Boguslavskiy, A. E., Mikosch, J., Gijsbertsen, A., Spanner, M., Patchkovskii, S., Gador, N., Vrakking, M. J. J. & Stolow, A. The multielectron ionization dynamics underlying attosecond strong-field spectroscopies. *Science* **335**, 1336–1340 (2012).
- [98] Treiber, L., Thaler, B., Heim, P., Stadlhofer, M., Kanya, R., Kitzler-Zeiler, M. & Koch, M. Observation of laser-assisted electron scattering in superfluid helium. *Nature Communications* **12**, 4204 (2021).
- [99] Buchenau, H., Knuth, E. L., Northby, J., Toennies, J. P. & Winkler, C. Mass spectra and time-of-flight distributions of helium cluster beams. *The Journal of Chemical Physics* **92**, 6875–6889 (1990).
- [100] Barranco, M., Guardiola, R., Hernández, S., Mayol, R., Navarro, J. & Pi, M. Helium nanodroplets: An overview. *Journal of Low Temperature Physics* **142**, 1–81 (2006).

- [101] Toennies, J. & Vilesov, A. Superfluid helium droplets: A uniquely cold nanomatrix for molecules and molecular complexes. *Angewandte Chemie International Edition* **43** (20), 2622 (2004).
- [102] Stienkemeier, F. & Lehmann, K. K. Spectroscopy and dynamics in helium nanodroplets. *Journal of Physics B: Atomic, Molecular and Optical Physics* **39**, R127–R166 (2006).
- [103] Tiggesbäumker, J. & Stienkemeier, F. Formation and properties of metal clusters isolated in helium droplets. *Phys. Chem. Chem. Phys.* **9**, 4748–4770 (2007).
- [104] Bünermann, O. & Stienkemeier, F. Modeling the formation of alkali clusters attached to helium nanodroplets and the abundance of high-spin states. *The European Physical Journal D* **61**, 645–655 (2011).
- [105] Yang, S. & Ellis, A. M. Helium droplets: a chemistry perspective. *Chem. Soc. Rev.* **42**, 472–484 (2013).
- [106] Mudrich, M. & Stienkemeier, F. Photoionisation of pure and doped helium nanodroplets. *International Reviews in Physical Chemistry* **33**, 301–339 (2014).
- [107] Wang, C. C., Kornilov, O., Gessner, O., Kim, J. H., Peterka, D. S. & Neumark, D. M. Photoelectron imaging of helium droplets doped with xe and kr atoms. *The Journal of Physical Chemistry A* **112**, 9356–9365 (2008).
- [108] Diederich, T., Döppner, T., Fennel, T., Tiggesbäumker, J. & Meiwes-Broer, K.-H. Shell structure of magnesium and other divalent metal clusters. *Phys. Rev. A* **72**, 023203 (2005).
- [109] Tiggesbäumker, J. & Stienkemeier, F. Formation and properties of metal clusters isolated in helium droplets. *Physical Chemistry Chemical Physics* **9**, 4748 (2007).
- [110] Döppner, T., Diederich, T., Przystawik, A., Truong, N. X., Fennel, T., Tiggesbäumker, J. & Meiwes-Broer, K. H. Charging of metal clusters in helium droplets exposed to intense femtosecond laser pulses. *Physical Chemistry Chemical Physics* **9**, 4639 (2007).
- [111] Fennel, T., Meiwes-Broer, K.-H., Tiggesbäumker, J., Reinhard, P.-G., Dinh, P. M. & Suraud, E. Laser-driven nonlinear cluster dynamics. *Rev. Mod. Phys.* **82**, 1793–1842 (2010).
- [112] Dong, F. Vibrational transition moment angles in isolated biomolecules: A structural tool. *Science* **298**, 1227–1230 (2002).
- [113] Lehmann, K. K. & Scoles, G. The ultimate spectroscopic matrix? *Science* **279**, 2065–2066 (1998).
- [114] Ancilotto, F., Lerner, P. B. & Cole, M. W. Physics of solvation. *Journal of Low Temperature Physics* **101**, 1123–1146 (1995).
- [115] Stienkemeier, F., Higgins, J., Ernst, W. E. & Scoles, G. Laser spectroscopy of alkali-doped helium clusters. *Physical Review Letters* **74**, 3592–3595 (1995).

- [116] Stienkemeier, F., Higgins, J., Callegari, C., Kanorsky, S. I., Ernst, W. E. & Scoles, G. Spectroscopy of alkali atoms (Li, Na, K) attached to large helium clusters. *Zeitschrift für Physik D: Atoms, Molecules and Clusters* **38**, 253–263 (1996).
- [117] Bünermann, O., Mudrich, M., Weidemüller, M. & Stienkemeier, F. Spectroscopy of Cs attached to helium nanodroplets. *The Journal of Chemical Physics* **121**, 8880–8886 (2004).
- [118] Theisen, M., Lackner, F. & Ernst, W. E. Cs atoms on helium nanodroplets and the immersion of Cs<sub>+</sub> into the nanodroplet. *The Journal of Chemical Physics* **135**, 074306 (2011).
- [119] Fechner, L., Grüner, B., Sieg, A., Callegari, C., Ancilotto, F., Stienkemeier, F. & Mudrich, M. Photoionization and imaging spectroscopy of rubidium atoms attached to helium nanodroplets. *Physical Chemistry Chemical Physics* **14**, 3843 (2012).
- [120] Rendler, N., Scognamiglio, A., Dulitz, K., Stienkemeier, F., Barranco, M., Pí, M. & Halberstadt, N. Dynamics of photo-excited Cs atoms attached to helium nanodroplets. *arXiv:2106.12330* (2021).
- [121] Kelbg, M., Zabel, M., Krebs, B., Kazak, L., Meiwes-Broer, K.-H. & Tiggesbäumker, J. Auger emission from the Coulomb explosion of helium nanoplasmas. *The Journal of Chemical Physics* **150**, 204302 (2019).
- [122] Elastic electron-atom scattering cross-sections database at <http://www.ioffe.ru/ES/Elastic/>.
- [123] Corkum, P. B. Plasma perspective on strong field multiphoton ionization. *Physical Review Letters* **71**, 1994–1997 (1993).
- [124] Lewenstein, M., Balcou, P., Ivanov, M. Y., L’Huillier, A. & Corkum, P. B. Theory of high-harmonic generation by low-frequency laser fields. *Phys. Rev. A* **49**, 2117–2132 (1994).
- [125] Kim, K.-Y., Glowina, J. H., Taylor, A. J. & Rodriguez, G. Terahertz emission from ultrafast ionizing air in symmetry-broken laser fields. *Optics Express* **15**, 4577 (2007).
- [126] Vvedenskii, N. V., Korytin, A. I., Kostin, V. A., Murzanev, A. A., Silaev, A. A. & Stepanov, A. N. Two-color laser-plasma generation of terahertz radiation using a frequency-tunable half harmonic of a femtosecond pulse. *Phys. Rev. Lett.* **112**, 055004 (2014).
- [127] Johnson, L. A., Palastro, J. P., Antonsen, T. M. & Kim, K. Y. THz generation by optical Cherenkov emission from ionizing two-color laser pulses. *Physical Review A* **88**, 063804 (2013).
- [128] Kotelnikov, I. A., Borodin, A. V. & Shkurinov, A. P. Multiphoton ionization of atoms by a two-color laser pulse. *Journal of Experimental and Theoretical Physics* **112**, 946–951 (2011).
- [129] You, Y. S., Oh, T. I. & Kim, K. Y. Off-axis phase-matched terahertz emission from two-color laser-induced plasma filaments. *Physical Review Letters* **109**, 183902 (2012).

- [130] Bagulov, D. S. & Kotelnikov, I. A. Theory of multiphoton and tunnel ionization in a bichromatic field. *Journal of Experimental and Theoretical Physics* **116**, 20–31 (2013).
- [131] Reimann, K. Table-top sources of ultrashort THz pulses. *Reports on Progress in Physics* **70**, 1597–1632 (2007).
- [132] Yeh, K.-L., Hoffmann, M. C., Hebling, J. & Nelson, K. A. Generation of 10 $\mu$ J ultrashort terahertz pulses by optical rectification. *Applied Physics Letters* **90**, 171121 (2007).
- [133] Kitada, T., Tanaka, F., Takahashi, T., Morita, K. & Isu, T. GaAs/AlAs coupled multilayer cavity structures for terahertz emission devices. *Applied Physics Letters* **95**, 111106 (2009).
- [134] Jiang, Y., Li, D., Ding, Y. J. & Zotova, I. B. Terahertz generation based on parametric conversion: from saturation of conversion efficiency to back conversion. *Optics Letters* **36**, 1608 (2011).
- [135] Hirori, H., Doi, A., Blanchard, F. & Tanaka, K. Single-cycle terahertz pulses with amplitudes exceeding 1 MV/cm generated by optical rectification in LiNbO<sub>3</sub>. *Applied Physics Letters* **98**, 091106 (2011).
- [136] Vicario, C., Ovchinnikov, A. V., Ashitkov, S. I., Agranat, M. B., Fortov, V. E. & Hauri, C. P. Generation of 0.9-mJ THz pulses in DSTMS pumped by a Cr:Mg<sub>2</sub>SiO<sub>4</sub> laser. *Optics Letters* **39**, 6632 (2014).
- [137] Shalaby, M. & Hauri, C. P. Demonstration of a low-frequency three-dimensional terahertz bullet with extreme brightness. *Nature Communications* **6**, 5976 (2015).
- [138] Jin, Q., E, Y., Williams, K., Dai, J. & Zhang, X.-C. Observation of broadband terahertz wave generation from liquid water. *Applied Physics Letters* **111**, 071103 (2017).
- [139] Knyazev, B. A., Kulipanov, G. N. & Vinokurov, N. A. Novosibirsk terahertz free electron laser: instrumentation development and experimental achievements. *Measurement Science and Technology* **21**, 054017 (2010).
- [140] Abo-Bakr, M., Feikes, J., Holldack, K., Kuske, P., Peatman, W. B., Schade, U., Wüstefeld, G. & Hübers, H.-W. Brilliant, coherent far-infrared (THz) synchrotron radiation. *Physical Review Letters* **90**, 094801 (2003).
- [141] Carr, G. L., Martin, M. C., McKinney, W. R., Jordan, K., Neil, G. R. & Williams, G. P. High-power terahertz radiation from relativistic electrons. *Nature* **420**, 153–156 (2002).
- [142] Williams, G. P. FAR-IR/THz radiation from the jefferson laboratory, energy recovered linac, free electron laser. *Review of Scientific Instruments* **73**, 1461–1463 (2002).
- [143] Huismans, Y., Rouzée, A., Gijsbertsen, A., Logman, P. S. W. M., Lépine, F., Cauchy, C., Zamith, S., Stodolna, A. S., Jungmann, J. H., Bakker, J. M., Berden, G., Redlich, B., van der Meer, A. F. G., Schafer, K. J. & Vrakking, M. J. J. Photoelectron angular distributions from the ionization of xenon Rydberg states by midinfrared radiation. *Physical Review A* **87**, 033413 (2013).

- [144] Wetzels, A., Gürtler, A., Noordam, L. D., Robicheaux, F., Dimu, C., Muller, H. G., Vrakking, M. J. J. & van der Zande, W. J. Rydberg state ionization by half-cycle-pulse excitation: Strong kicks create slow electrons. *Physical Review Letters* **89**, 273003 (2002).
- [145] Takahashi, E., Nabekawa, Y. & Midorikawa, K. Generation of 10- $\mu$ J coherent extreme-ultraviolet light by use of high-order harmonics. *Optics Letters* **27**, 1920 (2002).
- [146] Hergott, J.-F., Kovacev, M., Merdji, H., Hubert, C., Mairesse, Y., Jean, E., Breger, P., Agostini, P., Carré, B. & Salières, P. Extreme-ultraviolet high-order harmonic pulses in the microjoule range. *Phys. Rev. A* **66**, 021801 (2002).
- [147] Tzallas, P., Skantzakis, E. & Charalambidis, D. Measuring the absolute carrier-envelope phase of many-cycle laser fields. *Phys. Rev. A* **82**, 061401 (2010).
- [148] Shafir, D., Soifer, H., Bruner, B. D., Dagan, M., Mairesse, Y., Patchkovskii, S., Ivanov, M. Y., Smirnova, O. & Dudovich, N. Resolving the time when an electron exits a tunnelling barrier. *Nature* **485**, 343–346 (2012).
- [149] Takahashi, E. J., Lan, P., Mücke, O. D., Nabekawa, Y. & Midorikawa, K. Attosecond nonlinear optics using gigawatt-scale isolated attosecond pulses. *Nature Communications* **4**, 2691 (2013).
- [150] Pedatzur, O., Orenstein, G., Serbinnenko, V., Soifer, H., Bruner, B. D., Uzan, A. J., Brambila, D. S., Harvey, A. G., Torlina, L., Morales, F., Smirnova, O. & Dudovich, N. Attosecond tunnelling interferometry. *Nature Physics* **11**, 815–819 (2015).
- [151] Huang, W. R., Huang, S.-W., Granados, E., Ravi, K., Hong, K.-H., Zapata, L. E. & Kärtner, F. X. Highly efficient terahertz pulse generation by optical rectification in stoichiometric and cryo-cooled congruent lithium niobate. *Journal of Modern Optics* **62**, 1486–1493 (2014).
- [152] Vicario, C., Jazbinsek, M., Ovchinnikov, A. V., Chefonov, O. V., Ashitkov, S. I., Agranat, M. B. & Hauri, C. P. High efficiency THz generation in DSTMS, DAST and OH1 pumped by Cr:forsterite laser. *Optics Express* **23**, 4573 (2015).
- [153] Clerici, M., Peccianti, M., Schmidt, B. E., Caspani, L., Shalaby, M., Giguère, M., Lotti, A., Couairon, A., Légaré, F., Ozaki, T., Faccio, D. & Morandotti, R. Wavelength scaling of terahertz generation by gas ionization. *Physical Review Letters* **110**, 253901 (2013).
- [154] Buldt, J., Mueller, M., Stark, H., Jauregui, C. & Limpert, J. Fiber laser-driven gas plasma-based generation of THz radiation with 50-mW average power. *Applied Physics B* **126**, 2 (2019).
- [155] Koulouklidis, A. D., Gollner, C., Shumakova, V., Fedorov, V. Y., Pugžlys, A., Baltuška, A. & Tzortzakakis, S. Observation of strong THz fields from mid-infrared two-color laser filaments. In *Conference on Lasers and Electro-Optics* (OSA, 2018).

- [156] Koulouklidis, A. D., Gollner, C., Shumakova, V., Fedorov, V. Y., Pugžlys, A., Baltuška, A. & Tzortzakis, S. Observation of extremely efficient terahertz generation from mid-infrared two-color laser filaments. *Nature Communications* **11**, 292 (2020).
- [157] Oh, T. I., You, Y. S., Jhajj, N., Rosenthal, E. W., Milchberg, H. M. & Kim, K. Y. Intense terahertz generation in two-color laser filamentation: energy scaling with terawatt laser systems. *New Journal of Physics* **15**, 075002 (2013).
- [158] Harimoto, T., Takeuchi, Y. & Fujita, M. Spectral properties of second-harmonic generation at 800 nm in a BiB3O6 crystal. *Optics Express* **12**, 811 (2004).
- [159] Abramowitz, M. *Handbook of mathematical functions with formulas, graphs, and mathematical tables* (Martino Publishing, Mansfield Centre, CT, 2014).
- [160] Gribakin, G. F. & Kuchiev, M. Y. Multiphoton detachment of electrons from negative ions. *Physical Review A* **55**, 3760–3771 (1997).
- [161] Perelomov, A. & Popov, V. Ionization of atoms in an alternating electrical field. iii. *Journal of Experimental and Theoretical Physics* **25**, 336 (1967).
- [162] Popruzhenko, S. & Bauer, D. Strong field approximation for systems with coulomb interaction. *Journal of Modern Optics* **55**, 2573–2589 (2008).
- [163] Smirnova, O., Spanner, M. & Ivanov, M. Analytical solutions for strong field-driven atomic and molecular one- and two-electron continua and applications to strong-field problems. *Physical Review A* **77**, 033407 (2008).
- [164] Torlina, L. & Smirnova, O. Time-dependent analytical R-matrix approach for strong-field dynamics. I. One-electron systems. *Physical Review A* **86**, 043408 (2012).
- [165] Keil, T., Popruzhenko, S. V. & Bauer, D. Laser-driven recollisions under the coulomb barrier. *Physical Review Letters* **117** (2016).
- [166] Maxwell, A. S., Popruzhenko, S. V. & Faria, C. F. d. M. Treating branch cuts in quantum trajectory models for photoelectron holography. *Phys. Rev. A* **98**, 063423 (2018).
- [167] Popruzhenko, S. V., Mur, V. D., Popov, V. S. & Bauer, D. Strong field ionization rate for arbitrary laser frequencies. *Phys. Rev. Lett.* **101**, 193003 (2008).
- [168] Laryushin, I. Generation of terahertz radiation by two-color ionizing laser pulses with arbitrary intensity ratios. *Photonics* **7**, 38 (2020).
- [169] Tulskey, V. A., Bagheri, M., Saalman, U. & Popruzhenko, S. V. Boosting terahertz-radiation power with two-color circularly polarized midinfrared laser pulses. *Phys. Rev. A* **98**, 053415 (2018).
- [170] Dai, J., Karpowicz, N. & Zhang, X.-C. Coherent polarization control of terahertz waves generated from two-color laser-induced gas plasma. *Physical Review Letters* **103**, 023001 (2009).

- [171] Wen, H. & Lindenberg, A. M. Coherent terahertz polarization control through manipulation of electron trajectories. *Physical Review Letters* **103**, 023902 (2009).
- [172] Meng, C., Chen, W., Wang, X., Lü, Z., Huang, Y., Liu, J., Zhang, D., Zhao, Z. & Yuan, J. Enhancement of terahertz radiation by using circularly polarized two-color laser fields. *Applied Physics Letters* **109**, 131105 (2016).
- [173] Kim, K.-Y. Generation of coherent terahertz radiation in ultrafast laser-gas interactions. *Physics of Plasmas* **16**, 056706 (2009).
- [174] Eichmann, H., Egbert, A., Nolte, S., Momma, C., Wellegehausen, B., Becker, W., Long, S. & McIver, J. K. Polarization-dependent high-order two-color mixing. *Physical Review A* **51**, R3414–R3417 (1995).
- [175] Milošević, D. B., Becker, W. & Kopold, R. Generation of circularly polarized high-order harmonics by two-color coplanar field mixing. *Phys. Rev. A* **61**, 063403 (2000).
- [176] Milošević, D. B. Atomic and molecular processes in a strong bicircular laser field. *Atoms* **6**, 61 (2018).
- [177] Frolov, M. V., Manakov, N. L., Minina, A. A., Vvedenskii, N. V., Silaev, A. A., Ivanov, M. Y. & Starace, A. F. Control of harmonic generation by the time delay between two-color, bicircular few-cycle mid-IR laser pulses. *Physical Review Letters* **120**, 263203 (2018).
- [178] Dixit, G., Jiménez-Galán, Á., Medišauskas, L. & Ivanov, M. Control of the helicity of high-order harmonic radiation using bichromatic circularly polarized laser fields. *Physical Review A* **98** (2018).
- [179] Jiménez-Galán, Á., Zhavoronkov, N., Ayuso, D., Morales, F., Patchkovskii, S., Schloz, M., Pisanty, E., Smirnova, O. & Ivanov, M. Control of attosecond light polarization in two-color bicircular fields. *Physical Review A* **97**, 023409 (2018).
- [180] Frolov, M. V., Manakov, N. L., Minina, A. A., Silaev, A. A., Vvedenskii, N. V., Ivanov, M. Y. & Starace, A. F. Analytic description of high-order harmonic generation in the adiabatic limit with application to an initial  $s$  state in an intense bicircular laser pulse. *Physical Review A* **99**, 053403 (2019).
- [181] Gazibegović-Busuladžić, A., Becker, W. & Milošević, D. B. Helicity asymmetry in strong-field ionization of atoms by a bicircular laser field. *Optics Express* **26**, 12684 (2018).
- [182] Kostin, V. A. & Vvedenskii, N. V. Ionization-induced conversion of ultrashort bessel beam to terahertz pulse. *Optics Letters* **35**, 247 (2010).
- [183] Ushakov, A. A., Chizhov, P. A., Volkov, R. V., Bukin, V. V. & Garnov, S. V. Dependence of the efficiency of terahertz radiation generation on the state of two-color pump field polarization during optical breakdown of air. *Bulletin of the Lebedev Physics Institute* **41**, 200–204 (2014).

- [184] Song, Q., Yuan, X., Hu, S., Huang, J., Zhong, H., Lin, Q., Wang, H., Lu, X., Zheng, M., Cai, Y., Zeng, X. & Xu, S. Enhance terahertz radiation and its polarization-control with two paralleled filaments pumped by two-color femtosecond laser fields. *Optics Express* **29**, 22659 (2021).
- [185] Volkov, R. V., Chizhov, P. A., Ushakov, A. A., Bukin, V. V., Garnov, S. V. & Savel'ev, A. B. Optimal polarization of a two-colored pump for terahertz generation with a phase-unstable scheme. *Laser Physics* **25**, 065403 (2015).
- [186] Kostin, V. A., Laryushin, I. D., Silaev, A. A. & Vvedenskii, N. V. Ionization-induced multiwave mixing: Terahertz generation with two-color laser pulses of various frequency ratios. *Phys. Rev. Lett.* **117**, 035003 (2016).
- [187] Zhang, L.-L., Wang, W.-M., Wu, T., Zhang, R., Zhang, S.-J., Zhang, C.-L., Zhang, Y., Sheng, Z.-M. & Zhang, X.-C. Observation of terahertz radiation via the two-color laser scheme with uncommon frequency ratios. *Physical Review Letters* **119**, 235001 (2017).
- [188] Balčiūnas, T., Lorenc, D., Ivanov, M., Smirnova, O., Zheltikov, A. M., Dietze, D., Untertainer, K., Rathje, T., Paulus, G. G., Baltuška, A. & Haessler, S. CEP-stable tunable THz-emission originating from laser-waveform-controlled sub-cycle plasma-electron bursts. *Optics Express* **23**, 15278 (2015).
- [189] Pitaevski, L. P. & Lifshitz, E. M. *X. Physical Kinetics* (Elsevier Science, 2012).
- [190] Fletcher, J. & Cowling, I. R. Electron impact ionization of neon and argon. *Journal of Physics B: Atomic and Molecular Physics* **6**, L258–L261 (1973).
- [191] Cook, D. J. & Hochstrasser, R. M. Intense terahertz pulses by four-wave rectification in air. *Opt. Lett.* **25**, 1210–1212 (2000).
- [192] Bartel, T., Gaal, P., Reimann, K., Woerner, M. & Elsaesser, T. Generation of single-cycle THz transients with high electric-field amplitudes. *Optics Letters* **30**, 2805 (2005).
- [193] Babushkin, I., Skupin, S. & Herrmann, J. Generation of terahertz radiation from ionizing two-color laser pulses in ar filled metallic hollow waveguides. *Optics Express* **18**, 9658 (2010).
- [194] Murray, R., Ruiz, C., Marangos, J. P. & Ivanov, M. Y. Control of diffraction of electron wave packets on diatomic molecules using two-colour fields. *Journal of Physics B: Atomic, Molecular and Optical Physics* **43**, 135601 (2010).
- [195] Liseykina, T. & Popruzhenko, S. Bright single-cycle terahertz source based on gas cells irradiated by two-color laser pulses. *Journal of Physics: Conference Series* **1412**, 042005 (2020).
- [196] Fedorov, V. Y. & Tzortzakis, S. Extreme THz fields from two-color filamentation of mid-infrared laser pulses. *Physical Review A* **97**, 063842 (2018).

- [197] Daigle, J.-F., Th  berge, F., Henriksson, M., Wang, T.-J., Yuan, S., Ch  teauneuf, M., Dubois, J., Pich  , M. & Chin, S. L. Remote THz generation from two-color filamentation: long distance dependence. *Optics Express* **20**, 6825 (2012).
- [198] Berg  , L., Skupin, S., K  hler, C., Babushkin, I. & Herrmann, J. 3D numerical simulations of THz generation by two-color laser filaments. *Physical Review Letters* **110**, 073901 (2013).
- [199] Mitrofanov, A. V., Voronin, A. A., Sidorov-Biryukov, D. A., Pug  zlys, A., Stepanov, E. A., Andriukaitis, G., Fl  ry, T., Ali  sauskas, S., Fedotov, A. B., Baltu  ska, A. & Zheltikov, A. M. Mid-infrared laser filaments in the atmosphere. *Scientific Reports* **5**, 8368 (2015).
- [200] Bogatskaya, A. V. & Popov, A. M. On the possibility of the amplification of subterahertz electromagnetic radiation in a plasma channel created by a high-intensity ultrashort laser pulse. *JETP Letters* **97**, 388–392 (2013).
- [201] Bogatskaya, A. V. & Popov, A. M. New approach to the problem of THz generation by intense two-color laser fields. *Laser Physics* **28**, 115301 (2018).
- [202] Chiril  , C. C., Dreissigacker, I., van der Zwan, E. V. & Lein, M. Emission times in high-order harmonic generation. *Physical Review A* **81**, 033412 (2010).
- [203] Murakami, M., Korobkin, O. & Horbatsch, M. High-harmonic generation from hydrogen atoms driven by two-color mutually orthogonal laser fields. *Phys. Rev. A* **88**, 063419 (2013).
- [204] Zagoya, C., Bonner, M., Chomet, H., Slade, E. & Figueira de Morisson Faria, C. Different time scales in plasmonically enhanced high-order-harmonic generation. *Phys. Rev. A* **93**, 053419 (2016).
- [205] Hern  ndez-Garc  a, C., Popmintchev, T., Murnane, M. M., Kapteyn, H. C., Plaja, L., Becker, A. & Jaron-Becker, A. Isolated broadband attosecond pulse generation with near- and mid-infrared driver pulses via time-gated phase matching. *Optics Express* **25**, 11855 (2017).
- [206] Li, J.-B., Zhang, X., Yue, S.-J., Wu, H.-M., Hu, B.-T. & Du, H.-C. Enhancement of the second plateau in solid high-order harmonic spectra by the two-color fields. *Optics Express* **25**, 18603 (2017).
- [207] Peng, D., Pi, L.-W., Frolov, M. V. & Starace, A. F. Enhancing high-order-harmonic generation by time delays between two-color, few-cycle pulses. *Physical Review A* **95**, 033413 (2017).
- [208] Su  rez, N., Chac  n, A., P  rez-Hern  ndez, J. A., Biegert, J., Lewenstein, M. & Ciappina, M. F. High-order-harmonic generation in atomic and molecular systems. *Physical Review A* **95**, 033415 (2017).
- [209] Tancogne-Dejean, N. & Rubio, A. Atomic-like high-harmonic generation from two-dimensional materials. *Science Advances* **4**, eaao5207 (2018).

- [210] Chen, C., Guo, F.-M., Yang, Y.-J., Chen, Y.-J. & Yang, S.-P. Role of quantum orbits in odd-even high harmonic generation from atoms in bichromatic laser fields. *EPL (Europhysics Letters)* **127**, 34004 (2019).
- [211] He, L., Yuan, G., Wang, K., Hua, W., Yu, C. & Jin, C. Optimization of temporal gate by two-color chirped lasers for the generation of isolated attosecond pulse in soft x rays. *Photonics Research* **7**, 1407 (2019).
- [212] Paul, P. M., Toma, E. S., Breger, P., Mullot, G., Augé, F., Balcou, P., Muller, H. G. & Agostini, P. Observation of a train of attosecond pulses from high harmonic generation. *Science* **292**, 1689–1692 (2001).
- [213] Neyra, E., Videla, F., Pérez-Hernández, J. A., Ciappina, M. F., Roso, L. & Torchia, G. A. High-order harmonic generation driven by chirped laser pulses induced by linear and non linear phenomena. *The European Physical Journal D* **70**, 243 (2016).
- [214] Krause, J. L., Schafer, K. J. & Kulander, K. C. High-order harmonic generation from atoms and ions in the high intensity regime. *Phys. Rev. Lett.* **68**, 3535–3538 (1992).
- [215] Tulskey, V. A. & Bauer, D. Numerical time-of-flight analysis of the strong-field photoeffect. *Phys. Rev. Research* **2**, 043083 (2020).
- [216] Guo, L., Hu, S., Liu, M., Shu, Z., Liu, X., Li, J., Yang, W., Lu, R., Han, S. & Chen, J. Accuracy of the semiclassical picture of photoionization in intense laser fields. *arXiv:1905.00213* (2019).
- [217] Guo, L., Liu, M., Lu, R., Han, S. & Chen, J. Analysis of above-threshold ionization by “Wigner-distribution-like function” method. *Laser and Particle Beams* **37**, 448–462 (2019).
- [218] Eckle, P., Smolarski, M., Schlup, P., Biegert, J., Staudte, A., Schöffler, M., Muller, H. G., Dörner, R. & Keller, U. Attosecond angular streaking. *Nature Physics* **4**, 565–570 (2008).
- [219] Pfeiffer, A. N., Cirelli, C., Smolarski, M. & Keller, U. Recent attoclock measurements of strong field ionization. *Chemical Physics* **414**, 84–91 (2013).
- [220] Landsman, A. S., Weger, M., Maurer, J., Boge, R., Ludwig, A., Heuser, S., Cirelli, C., Gallmann, L. & Keller, U. Ultrafast resolution of tunneling delay time. *Optica* **1**, 343 (2014).
- [221] Han, M., Ge, P., Fang, Y., Yu, X., Guo, Z., Ma, X., Deng, Y., Gong, Q. & Liu, Y. Unifying tunneling pictures of strong-field ionization with an improved attoclock. *Physical Review Letters* **123**, 073201 (2019).
- [222] Cohen, L. Time-frequency distributions-a review. *Proceedings of the IEEE* **77**, 941–981 (1989).
- [223] Kim, J.-H., Lee, D. G., Shin, H. J. & Nam, C. H. Wigner time-frequency distribution of high-order harmonics. *Physical Review A* **63**, 063403 (2001).

- [224] Scholl, S. Fourier, Gabor, Morlet or Wigner: Comparison of time-frequency transforms. *arXiv:2101.06707* (2021).
- [225] Borbély, S., Tóth, A., Arbó, D. G., Tókesi, K. & Nagy, L. Photoelectron holography of atomic targets. *Phys. Rev. A* **99**, 013413 (2019).
- [226] Li, Y., Zhou, Y., He, M., Li, M. & Lu, P. Identifying backward-rescattering photoelectron hologram with orthogonal two-color laser fields. *Optics Express* **24**, 23697 (2016).
- [227] Han, M., Ge, P., Shao, Y., Liu, M.-M., Deng, Y., Wu, C., Gong, Q. & Liu, Y. Revealing the sub-barrier phase using a spatiotemporal interferometer with orthogonal two-color laser fields of comparable intensity. *Physical Review Letters* **119**, 073201 (2017).
- [228] Nayak, A., Dumergue, M., Kühn, S., Mondal, S., Csizmadia, T., Harshitha, N., Füle, M., Kahaly, M. U., Farkas, B., Major, B., Szaszkó-Bogár, V., Földi, P., Majorosi, S., Tsatrafyllis, N., Skantzakis, E., Neoričić, L., Shirozhan, M., Vampa, G., Varjú, K., Tzallas, P., Sansone, G., Charalambidis, D. & Kahaly, S. Saddle point approaches in strong field physics and generation of attosecond pulses. *Physics Reports* **833**, 1–52 (2019).
- [229] Werby, N., Natan, A., Forbes, R. & Bucksbaum, P. H. Disentangling the subcycle electron momentum spectrum in strong-field ionization. *Phys. Rev. Research* **3**, 023065 (2021).

## LIST OF FIGURES

1.1	Spectra of 'direct' photoelectrons from argon in a laser field of intensity $I = 2 \cdot 10^{14} \text{W/cm}^2$ and wavelength $\lambda = 800 \text{ nm}$ with a weak ( $\xi = 0.1$ ) 400 nm component added. . . . .	12
1.2	PES in a two-color field as from Fig. 1.1(a) but calculated with CTMC . . .	14
1.3	PES for hydrogen in a circularly polarized laser pulse calculated using QPROP 3.2	24
1.4	PES for hydrogen in a linearly polarized laser pulse calculated using QPROP 3.2	25
2.1	Fourier decomposition (62) of the full PES with respect to the phase $\phi$ between the two laser components . . . . .	27
2.2	PoP $\Phi_1$ for argon in $\omega - 2\omega$ two-color $\uparrow\downarrow$ laser field with intensity $I_1 = 2 \cdot 10^{14} \text{W/cm}^2$ and wavelength $\lambda_1 = 800 \text{ nm}$ . . . . .	28
2.3	SFA-based PES and PoP $\Phi_n$ for circular two-color counter-rotating fields . .	29
2.4	Position of the phase flip of PoP $\Phi_1$ . . . . .	31
2.5	Left panel: Total spectrum $Y$ and magnitudes of first few Fourier components $Y_n$ for $n = 0-3$ evaluated in the $q_x = k_x/A_0 > 0$ direction . . . . .	33
2.6	Sketch of the setup used in the calculations. . . . .	35
2.7	Percentage of electrons that undergo a certain amount of scattering events indicated on the horizontal axis. . . . .	36

2.8	(a) PES predicted by the SFA for a two-color bicircular laser field with counter-rotating components of frequencies $\omega$ and $2\omega$ , interacting with an argon atom. (b) Same but for an argon atom placed in a helium droplet. . .	38
2.9	(a) PoP $\Phi_1$ from a continuous SFA-based distribution, (b) – the same but for a finite number $N_e = 2 \cdot 10^8$ of photoelectrons for each phase $\phi$ . (c) PoP $\Phi_2$ from a continuous SFA-based distribution, (d) the same but for a finite number $N_e = 2 \cdot 10^7$ of photoelectrons for each phase $\phi$ . (e) the same as (d) but with the (multiple) scattering on neutral helium atoms of a surrounding droplet being taken into account. For all cases $N_\phi = 20$ phases have been taken. . . . .	38
3.1	PES for argon in a two-color field with colinear components . . . . .	45
3.2	Ionization probability estimate $W = wT$ . . . . .	49
3.3	Average photoelectron momentum as a function of $2\xi$ for various relative phase shifts $\phi$ . . . . .	50
3.4	Average photoelectron momentum as a function of $2\xi$ for various intensities $I_1$ of the main laser field . . . . .	51
3.5	Average photoelectron momentum as a function of $I_2/(I_1 + I_2)$ for various total intensities $I_1 + I_2$ of the combined two-color laser field . . . . .	52
3.6	Momentum distribution in the polarization plane for hydrogen in a two-color field . . . . .	55
3.7	PES along the net momentum $\mathbf{k}_0$ axis and integrated over the transverse momentum . . . . .	56
3.8	PES for argon irradiated by a two-color $\odot\odot$ laser field. . . . .	58
3.9	Distribution function $f_{z=0}(k, x, t)$ of electrons in the $(x, k)$ plane at different times $t$ . . . . .	59
3.10	Dipole acceleration computed according to (109) as a function of time . . .	62
3.11	Relative magnitude of the electric field strengths . . . . .	62
3.12	Relative spectral density of the radiated power computed according to Eq. (111)	63
3.13	Total energy emitted in frequency range $\Delta\nu = 0.1 \div 10$ THz . . . . .	64
4.1	(a) Gabor-transformed spectrum of HHG . . . . .	68
4.2	(a) Time-energy-resolved PES from argon in the laser propagation direction	70
4.3	(a,d) Cumulative yield as a function of maximal registration time $t$ . . . . .	72
4.4	A section through the time and angle resolved distributions shown in Fig. 4.3(a,d)	72
4.5	(a) Vector potential $A(t)$ . (b) Time-energy-resolved photoelectron spectrum	74
4.6	Demonstration of elimination of long-timescale interference patterns from PES. . . . .	75

## ACKNOWLEDGEMENTS

*Let's go, in and out,  
twenty minutes adventure...*  
(Rick and Morty)

The path towards the completion of this thesis wasn't a trifling matter, but was an exciting adventure. And as every adventure, it would not be a great one without the companions and mentors that were around all the past years. At this point, I would like to thank my parents and all my relatives, colleagues and friends that inspired me on different stages of the multi-step process.

I would like to thank Prof. S.V. Popruzhenko who took me under the wing and patiently supported during my first steps in the scientific world. He encouraged me to travel abroad to participate in a conference for the first time, later helped me to get a guest scientist position in MPIPKS, a great place to work in Dresden where I still come to meet people and just for good memories. I am very pleased that even that I do not have joint scientific projects with S.V.P. to the present moment, we still keep in touch and always find time to see each other if we are in the same city.

Back in times when I was a student in Moscow, I met Prof. D. Bauer who gave a lecture course in MEPhI and created a memorable impression about computational physics in the sphere of strong-laser-matter interaction. Learning about an open PhD position in the group of D.B. in the Uni Rostock, I gladly got started to write an application hoping to get lucky with it. Now, after almost four years of work here, I have countless memories of pleasant episodes of all kinds. I especially value the freedom that D.B. gave me by providing me with multiple and really diverse physical problems to start and continue with. Besides letting me schedule by myself in which sequence to solve them, D.B. was always supportive if I tried extending the fields under consideration deeper than initially planned or if I proposed a completely different topic.

The working atmosphere in the QTMPs group was very positive and all other members of the group are also greatly acknowledged. In particular, I would like to send my regards to J. Rapp and A. Hanusch who gave me valuable knowledge about managing the IT infrastructure of our group.

Creativity during the working hours is greatly improved by quality of the remaining leisure time. Special thanks goes here to my friends L. Kazak and V. Kochetov with whom I had multiple inspiring discussions in physics taking place at ease with a beer in hand. And certainly the great inspiration came from my wife, O. Soloveva: even working in different kinds of physics, we gladly share knowledge in new computational tricks that we have learned and always help each other when needed.

## SELBSTÄNDIGKEITSERKLÄRUNG

Hiermit versichere ich, dass ich die vorliegende Arbeit selbständig angefertigt und ohne fremde Hilfe verfasst habe, keine außer den von mir angegebenen Hilfsmitteln und Quellen dazu verwendet habe und die den benutzten Werken inhaltlich und wörtlich entnommenen Stellen als solche kenntlich gemacht habe.

Rostock

---

(Abgabedatum)

---

(Vollständige Unterschrift)